UNIVERSITY OF SOUTHAMPTON

Faculty of Engineering and the Environment

Institute of Sound and Vibration Research

Vibration analysis of uncertain spot-welded structures

by

Ricardo Octavio de Alba Alvarez

Thesis for the degree of Doctor of Philosophy

May 2012

ABSTRACT

Spot-welded structures contain inherent variability in location and/or stiffness due to the complexity of the manufacturing process. Therefore, an analysis that includes the uncertainty generated in the joints will provide a range of response predictions, adding more value to the design process compared to deterministic results. Finite element (FE) analysis is frequently used in conjunction with Monte Carlo simulations (MCS) to predict the variability in the vibration response of assembled structures, however this is usually computationally expensive. Small numerical spot weld models must be used since real spot welded structures usually possess many spot welds and modelling each of them in detail would lead to additional computational effort, current models provide results sensitive to the element size.

In this thesis, a method to quantify the variability in the dynamic characteristics of structures due to uncertainty in the location and diameter of the spot welds is proposed and experimentally validated. Component mode synthesis (CMS) is used in combination with multipont constraint (MPC) connection models in order to improve the computational efficiency of the uncertainty analysis. However, if the number of degrees of freedom (DOFs) involved in the connection is large, then the CMS size reduction is less effective. Two techniques are proposed to overcome this problem: (i) characteristic constraint modes and (ii) application of a low rank update theory to the CMS matrices. A spot weld model based on MPCs is proposed and validated as part of the original contributions of this work. This model improves convergence and minimizes the sensitivity to the element size.

The application of the new method is experimentally validated in a double hat structure. Results show that the method presented is accurate when predicting the structure's natural frequencies and it can identify which modes are sensitive to the uncertainties in the spot welds and which modes are not.

CONTENTS

LIST OF FIGURES

LIST OF TABLES

DECLARATION OF AUTORSHIP

I, Ricardo Octavio de Alba Alvarez

declare that the thesis entitled

Vibration analysis of uncertain spot-welded structures

and the work presented in the thesis are both my own, and have been generated by me as the result of my own original research. I confirm that:

- this work was done wholly or mainly while in candidature for a research degree at this University;
- where any part of this thesis has previously been submitted for a degree or any other qualification at this University or any other institution, this has been clearly stated;
- where I have consulted the published work of others, this is always clearly attributed;
- where I have quoted from the work of others, the source is always given. With the exception of such quotations, this thesis is entirely my own work;
- I have acknowledged all main sources of help;
- where the thesis is based on work done by myself jointly with others, I have made clear exactly what was done by others and what I have contributed myself;
- parts of this work have been published in the following references:
    - De Alba R.O., Mace B.R. Ferguson N.S. and Lecomte C., "A low rank update theory for the vibration analysis of spot welded structures" ISMA-USD 2010, Leuven Belgium 2010.
    - De Alba R.O., Mace B.R. and Ferguson N.S., "Prediction of response variability in uncertain point connected structures using component

mode synthesis and characteristic constraint modes", RASD 2010, Southampton UK, 12-14 July 2010.

- De Alba R.O.,Ferguson N.S and Mace B.R.,"A multipoint constraint model for the vibration of spot welded structures", ISVR Technical Memorandum 982, June 2009.
- De Alba R.O.,Ferguson, N.S and Mace B.R.,"Dynamic analysis of structures with uncertain point connections",NOVEM 2009, Oxford UK,5-8 April 2009.

Signed: ……..

Date:……20/07/2012…….

ACKNOWLEDGEMENTS

I would like to thank my supervisors Professor Brian R. Mace and Dr. Neil Ferguson, without their guidance, time and involvement, this project would not have been possible.

I also appreciate the comments and feedback from Dr. Tim Waters, Dr. Yi Qiu and Dr. Christophe Lecompte and in general all the interaction with my friends and staff at ISVR.

I would like to express my gratitude to my sponsor, The Mexican Council for Science and Technology (Consejo Nacional de Ciencia y Tecnología, CONACYT), which supported my PhD studies.

I would like to thank my parents, grandmother and my brother for their understanding and endless love, through the duration of my studies.

Last but not least this thesis is dedicated to my other half, Patricia, for all the sacrifices, help, support and understanding during the last 4 years and during our entire marriage. Without my wife's encouragement, I would not have finished this degree, thank you for giving me the happiest moments of my life. To Ricky and Mila who are the motivation behind all our efforts to become better persons.

LIST OF SYMBOLS

Latin letters

A Area of element, Area of cross section

A Receptance matrix

A_n Mode n modal constant

B Component modal matrix

C Transformation matrix.

$\mathbf{D}(\omega)$ Disturbance to the nominal system,

D_n Diameter of the fitted circle in the Nyquist diagram

$\mathbf{D}_{se}^{1}$ Dynamic stiffness matrix

E Young's modulus

F Nodal forces

G Shear modulus and

$\mathbf{G}_i$ Matrix of coefficients (MPC equations)

$\mathbf{H}$ Constraint matrix.

$\mathbf{J}$ Jacobian matrix

$\mathbf{K}$ Stiffness matrix.

K_w Tranlational stiffness

$K_{\theta x}$ .Rotational stiffness

$K_{\theta y}$ Rotational stiffness

L Lagrangian

$\mathbf{M}$ Mass matrix

$\boldsymbol{N_j}$ Lagrange basis functions respectively.

$N_{i,i}$ Parametric shape functions.

N Substructure number,

$\boldsymbol{P}_j$ Serendipity basis functions respectively.

T Kinetic energy

U Potential energy

$\mathbf{Y}$ Mobility matrix

$\mathbf{Z}_c$ Impedance matrix

$\mathbf{d}_l$ and $\mathbf{d}_r$ Disturbance left and right vectors

$\mathbf{f}$ Vector of external forces.

$\mathbf{g}$ Interface basis coordinates.

i Connection number

j Node number.

k_b Beam flexural wave number equal to $2\pi / \lambda$

$\mathbf{q}$ Component modal coordinates

$r_{l,m}$ Pearson product-moment correlation coefficient between ε_l and ε_m

$\mathbf{u}$ Physical DOFs,

$\mathbf{u}_i'$ Local connection DOFs

$\mathbf{u}_{cc}$ Interface DOFs

$\mathbf{v}$ Independent modal coordinates

u, v, and *w* Displacement DOFs

(x', y') Connection local coordinates

x, y and *z* Coordinates

Greek letters

Γ Transformation matrix that relates connection local to modal DOFs

Ξ Transformation matrix defined to transform to global DOFs

Ψ Static constraint modes in CMS

η Modal loss factor

κ Modal stiffness matrix

λ Eigenvalue, wavelength

μ Modal mass matrix

ν Poisson's ratio

ρ Mass density

σ Standard deviation

ϕ Normal modes in CMS

ω Angular frequency

ABBREVIATIONS

(ACM2) Area contact model 2

(CMS) Component mode synthesis

(DOF) Degrees of freedom

(FEM) Finite element method

(FRFs) Frequency response functions

(MCS) Monte Carlo simulation

(MPC) Multipoint constraint

(PDF) Probability density function

(RSW) Resistance spot welding

(SEs) Spectral Elements

(SEA) Statistical energy analysis

1 INTRODUCTION

Structural elements such as beams, plates, rods, etc., are typically assembled together using elements called structural joints in order to build more complex structures. A built-up structure might contain many joints and the properties and characteristics of these connecting elements contribute significantly to the overall dynamic behaviour of the structure, e.g. natural frequencies, mode shapes and frequency response functions (FRFs). In the automotive industry one of the most important structural joint is the spot welded joint, or simply called the spot weld. A vehicle body contains several thousands of spot welds. The spot welds are manufactured using a process called resistance spot welding (RSW).

RSW is an efficient process to join vehicle body parts. It consists of four stages called squeezing, welding, forging and cooling [1] as shown in Figure 1.1. Two metal sheets are compressed between a pair of water-cooled copper-alloy electrodes with an external applied force, and then an electric current is passed through the sheets via the two electrodes to generate concentrated heating at the contact surface. The contact surfaces in the region of current concentration are heated for a very short duration by a pulse of low-voltage, high-amperage current. Due to heat generation at the contact surface and Joule heating, a molten nugget is formed at the interface of the two sheets. After the current flow ceases, the electrode force is maintained for a short duration to allow the workpiece to rapidly cool and solidify.

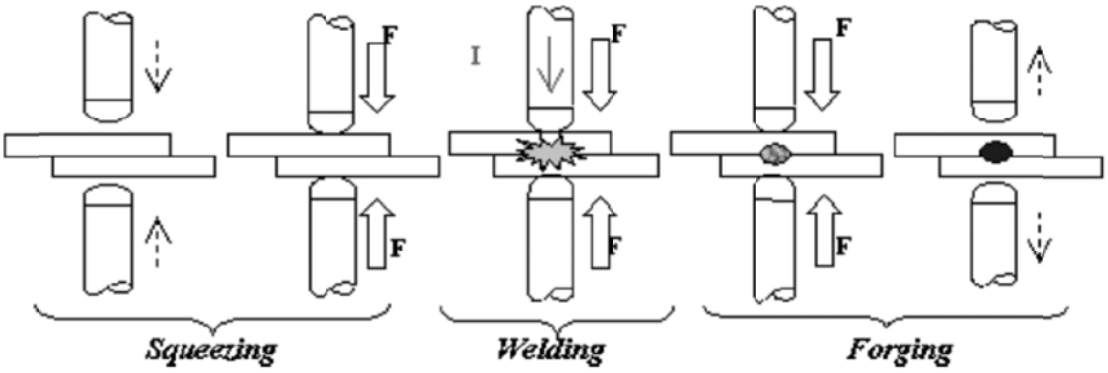

Figure 1.1: Figure 1: RSW welding sequence [1].

The contact surface area depends on the electrode diameter, applied force, temperature and metal deformation. It has been shown that the electrothermal and mechanical contact conditions influence the weld growth mechanisms [2]. Thus a RSW process involves interactions of thermal, electrical, mechanical and metallurgical phenomena.

All the interactions involved in the RSW lead to a large source of variability in the final characteristics of the spot weld such as the location, shape or size of the nugget. For example, the electrode contact region varies when the area at the electrode tips increases due to in-service degradation of electrode tips (pollution and erosion of the profile) affecting the nugget diameter. Figure 2 shows changes in the electrode profile after 300 welded points [1].

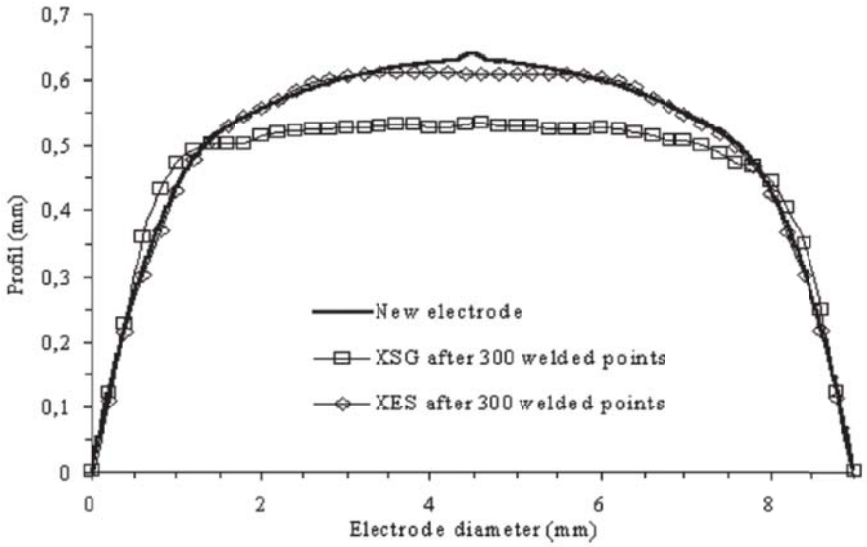

Figure 1.2: RSW electrode profiles [1]

Other sources of variation in this process are welding duration, electrical current changes, electrode-surface contact characteristics and thermal conditions amongst others.

Given this problem, there is current interest in developing methods to estimate the weld nugget parameters during the short time of the weld formation and create a real-time spot weld quality monitoring, but these investigations are current work and have not been implemented in industry [3].

The finite element method (FEM) is commonly used to compute deterministic predictions of complex systems. The inputs in a regular FEM analysis are the mass, stiffness and damping and the response quantities can be frequency response functions (FRFs), eigenvalues, eigenvectors etc. If the input parameters are accurate and the system is correctly modelled, then the output quantities will be accurate. Nevertheless the standard FEM does not include variations in the geometric and physical properties of the spot welds.

These variations lead to variations in the joint dynamic properties and the resulting overall dynamic behaviour of the built up structure. Since spot welds contain inherent variability due to the complexity of the manufacturing process, an analysis including the uncertainty generated in the joints providing a range of response values, can add more value in the design process compared to deterministic predictions.

In order to achieve that, it is necessary to use an adequate FE spot weld model, this model should be able to represent the physical and dynamic properties of these joints and therefore the variations in them. Then a method to include the uncertainties in the FE models must be implemented.

In the following sections, the existing FE spot weld models are reviewed, followed by a review of the available methods to include variability in FE models and finally the outline/scope of the thesis is given.

1.1 Finite element spot weld models

Modelling spot welds is a difficult task, mainly because there are many local effects such as geometrical irregularities, residual stresses, material inhomogeneities and defects due to the welding process that are not taken into account. Furthermore it is necessary to use models with as few degrees of freedom (DOF) as possible, since real spot welded structures usually possess many spot welds and modelling each of them in detail would lead to a major computational effort.

Two main types of spot weld models can be distinguished: models for stress analysis within the spot weld and models for vibration analysis which do not require the knowledge of stresses at the spot welds. In the first case, very detailed models are required to compute a smooth stress field at the spot weld. As stated previously, these models are used for stress analysis and durability. In general they are too detailed to use in dynamic analysis, leading to a prohibitive computational cost, therefore these models will not be reviewed in this thesis. In the second case the only requirement from the model is to simulate, as closely as possible, the stiffness (and mass) characteristics of the real spot welds and their influence on the rest of the structure. This allows much simpler models with far fewer DOFs.

These simpler models can be divided into two types, models that require coincident meshed surfaces in which the nodes of the plate elements of the joined surfaces are coincident and models that can be assembled with non-coincident meshes in which the plate nodes are non coincident.

The latter models offer a great advantage to industry, since it is not necessary to re-mesh surfaces to assemble them together. Next some of the most common models are reviewed.

1.1.1 Single beam models

These models were very commonly used in industry for many years. A node to node connection is applied between coincident meshes using a rigid link or a beam element.

According to Lardeur *et al.* [4] this connection is physically inconsistent and leads to imprecise and inconsistent results. Similarly, Palmonella *et al.* [5] state that this model is an inadequate representation for the behaviour of the spot weld and generally tends to underestimate its stiffness.

1.1.2 Single brick models

This model was first proposed by Pal and Cronin [6] and connect two surfaces using a single 3D solid element to characterise the spot weld nugget. The brick nodes are coincident with the plate nodes connected with rigid links in all DOFs, therefore it is necessary to have coincident meshes between surfaces.

1.1.3 Area contact model 2

This element was created by Heiserer et al [7] and is known as area contact model 2 (ACM2). This model consists of a brick element connecting the lower and upper plates with weighted average constraint elements, called RBE3 in MSC Nastran [8], as shown in Figure 1.3. RBE3 defines the motion at a reference grid point as the weighted average of the motions at a set of other grid points. The RBE3 element is able to distribute the applied loads onto a set of nodes without increasing the local stiffness as would happen with a rigid link. The ACM2 model is also known as CHEXA spot weld model in LMS virtual lab [9]. This model provides the advantage of being able to connect surfaces with non congruent meshes and locate the spot weld anywhere in the surface between nodes.

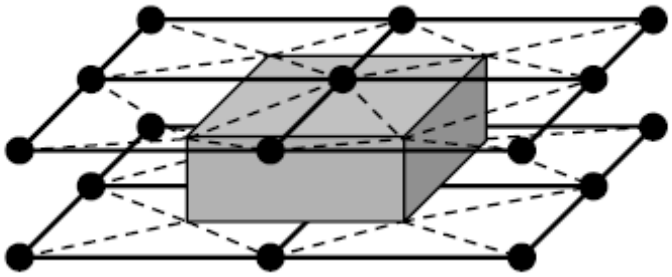

Figure 1.3: ACM2 model

1.1.4 CWELD

Fang *et al.* [10], proposed a model designed to connect congruent as well as non congruent meshes using a Multipoint constraint (MPC) equation. This element was implemented as the CWELD element in MSC/NASTRAN or PLINK in ESI/Pam-Crash. Figure 1.4 shows a sketch of the CWELD element. The elastic part of the CWELD element is a short beam from points GA to GB with six DOFs per node; this beam is modelled as a shear flexible Timoshenko type. The location of the element is defined with a free grid point GS, which is projected on the surfaces to be joined. Every node of the beam is connected to a chosen set of nodes of the plate to which it belongs. In Figure 4, the node GA for example is connected to the shell nodes GA1, GA2, GA3 and GA4 belonging to the upper plate. The portions of the plates delimited by the nodes GAi and GBi are called "patches" [8].

The DOFs of the spot weld end point GA are constrained as follows: the 3 translational and 3 rotational DOFs are connected to the 3 translational DOFs of each node GAi with constraints from Kirchoff shell theory,

$$\begin{Bmatrix} u \\ v \\ w \end{Bmatrix}_A = \sum N_i(\xi_A, \eta_A) \cdot \begin{Bmatrix} u \\ v \\ w \end{Bmatrix}_i \tag{1.1}$$

$$\theta_x^A = \frac{\partial w}{\partial y} = \sum N_{i,y} \cdot w_i \tag{1.2}$$

$$\theta_y^A = \frac{\partial w}{\partial x} = -\sum N_{i,x} \cdot w_i \tag{1.3}$$

$$\theta_z^A = \frac{1}{2}\left(\frac{\partial v}{\partial x} - \frac{\partial u}{\partial y}\right) = \frac{1}{2}\left(\sum N_{i,x} \cdot v_i - \sum N_{i,y} \cdot u_i\right) \tag{1.4}$$

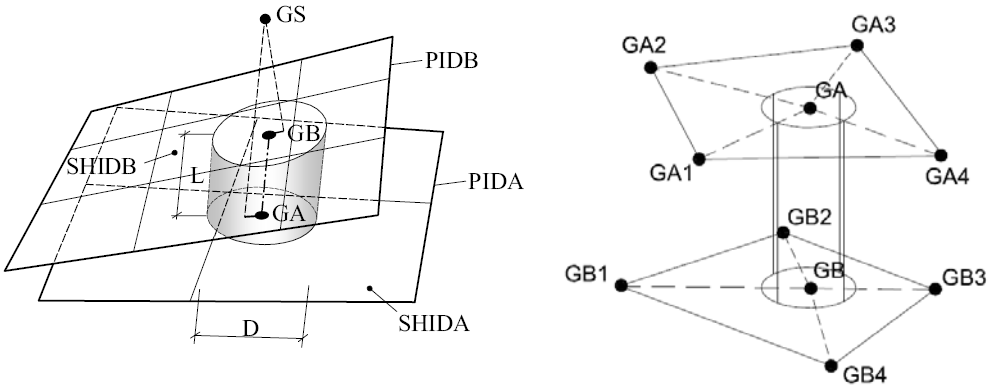

Figure 1.4: CWELD model

Here x, y and z are the co-ordinates with z being perpendicular to the element plane; $N_{i,i}$ are the parametric shape functions; ξ_A and η_A are the normalised coordinates; u, v, and w are the displacement DOFs and θ_x, θ_y and θ_z are rotational DOFs.

1.2 APPROACHES FOR A NON-DETERMINISTIC ANALYSIS

In order to include the uncertainties in a FE structural dynamics model, there are two contrasting approaches: (1) possibilistic and (2) probabilistic approaches. In possibilistic approaches the uncertain parameters are assumed to lie in a finite interval, where only the definition of a lower and upper bound is required. The definition of these bounds is normally a difficult task and in general is done based on experience or based on a limited number of experiments. The goal of a possibilistic propagation approach [11] is to calculate the bounds on the response quantity of interest. If the problem is monotonic, i.e. the output depends monotonically on every input parameter, it is sufficient to consider all combinations of the bounds of the input parameters only, which is referred to as the vertex method [12].

In probabilistic approaches [13,14], information about the likelihood and probability of events are included. The variation in the parameter(s) is specified by a probability density function (PDF) and the variation in the response can be quantified in terms of distribution functions or statistics. A standard PDF is normally assumed for the input

parameter(s). The normal distribution is often an adequate fit to product variability, in statistics, and this is also supported by the Central Limit Theorem [15]. However, the unbounded tails of the normal distribution are often inconsistent with reality, which has to be taken into account.

The standard method for propagating probabilistic data is the Monte Carlo (MC) method [16–20]. In standard MC sampling, parameter values are randomly drawn according to their probability distributions and a deterministic problem is solved for each sample. The results are analysed to estimate response statistics and distribution functions. The method is very robust and converges to the exact solution as the sample size tends to infinity. It makes no approximations and considers all effects modelled in the deterministic problem. In general, a sample size of the order of 10 is sufficient to estimate the mean of a distribution function and a sample size of the order of 100 is required to obtain a reasonable estimate of the variance. However, the numerical cost to estimate a small probability of failure can be in the order of thousands of deterministic solutions.

In order to reduce the computational time of the deterministic solution in the analysis of uncertainties when a FE model is used, the number of the degrees of freedom (DOF) can be reduced using component mode synthesis (CMS). CMS is a well established method to reduce the size of the model and also offers an appealing framework for the analysis of the structural dynamics of uncertain structures. One of the most accurate and frequently used CMS methods is the Craig-Bampton method [21]. In the fixed interface method the component normal modes are calculated with the interface between the components held fixed. These modes are further augmented by static constraint modes to improve convergence, yield the exact solution and assure the compatibility between components facilitating coupling of structures. It is also possible to perform an eigensolution on the constraint mode partitions of the mass and stiffness matrices. The resultant eigenvectors are called the characteristic constraint modes. When the Craig-Bampton method is used the DOFs of the model can be further reduced by truncating the characteristic constraint modes, especially in problems with large number of interface coordinates [22].

1.3 Scope of the thesis

The objective of this thesis is to predict the vibrational behaviour of built-up structures subject to variations in the location and size of the spot welds. This objective was divided into three parts:

(1) The analysis, evaluation and verification of spot weld FE models.

(2) Improve the efficiency of the dynamic analysis of spot welded structures for non deterministic analysis.

(3) Experimental validation of the proposed methodology.

In modelling the structure, a model of the spot weld which is connected to the substructures by MPCs has clear advantages. It can be located anywhere in the model and it is not necessary to re-mesh surfaces to assemble them together. Furthermore, MPC connections can be used to model changes in the location of the joint instead of modifying the FE model from one sample to the next.

In order to further improve the efficiency of the deterministic solution, CMS gives a sub-structuring framework by which the number DOFs are reduced [21]. Combining CMS with MPC joints, the response of the system can be evaluated for many spot weld locations using the same modal representation of the substructures, which is a big advantage when using a MCS for a non deterministic study.

As part of objective (1), in chapter 2 the MPC connection is analytically verified. The results from FE models with MPCs are compared to analytical solutions to evaluate the accuracy of these connections when the location is changed and to analyze the influence of the size and the type of element at which these MPCs are attached. Two different models are analyzed: two infinite beams and two simply supported plates. In all the models there is a single elastic connection with translational and rotational stiffnesses.

In chapter 3, as part of objective (2), MPC connections are combined with the Craig-Bampton method in order to reduce the computational time of a MCS. Combining CMS with MPC joints, the response of the system can be evaluated for many joint locations using the same modal representation of the substructures. However it will be seen that when the number of degrees of freedom involved in the connection is large, the CMS size reduction is less efficient because the interface DOFs are not reduced. To further improve the efficiency of this analysis, two additional methods are applied: characteristic constraint modes and a low-rank update theory.

In chapter 4 a robust spot weld model based on MPC connections is proposed and validated. This model is compatible with the methods in chapter 3 and is capable of modelling not only changes in location but also changes in diameter of the spot weld with the same computational expense as the simple MPC connection. This proposed connection is also less sensitive to element size.

In chapter 5 the robust spot weld model is combined with the numerical methods proposed in chapter 3 to obtain non deterministic predictions. These predictions are experimentally validated in a system of two hat profiles with four spot welds with 54 samples.

In summary the original contributions of this work include:

- Analytical validation of MPC connections, especially when modelling changes in the connection location.
- The application of the Craig-Bampton method and characteristic constraint modes in combination with the MPCs connection in order to model uncertainty in the locations of joints.
    - Constraints DOFs in areas instead of lines.
    - Elastic connection instead of rigid.
- The application of low rank update theory in the CMS framework in order to improve models with a large number of coupling DOFs.
- A spot weld model robust to changes in the mesh characteristics and capable of modelling the diameter of the spot welds was proposed and validated.

- Experimental validation of the non deterministic model.

2 VALIDATION OF MULTI POINT CONSTRAINTS FOR SPOT-WELD MODELS

As mentioned in the previous chapter, in FE models spot welds are commonly represented by two-noded elements (e.g. beams or springs with lumped masses) or by rigid connections. The parameters of these simple elements represent the stiffness characteristics of the real joint, and therefore their influence on the rest of the structure. This simple connection can be connected to the substructures in mainly two different ways: (1) a direct connection between nodes in the substructures (node-to-node connection) or (2) using interpolation elements or multipoint constraints (MPCs) to connect the joint nodes to the substructures. The node-to-node connection requires coincident meshes: if the location of the weld changes, then the mesh of both surfaces needs to be modified. In contrast, when interpolation elements or MPCs are used, the connection can be placed at any location using the existing surface meshes.

The latter feature offers a great advantage to industry, since it is then possible to assemble components with different mesh characteristics or to assemble components with complex geometries in which it is very difficult to have coincident nodes. Moreover, MPC connections can improve the computational efficiency when Monte Carlo simulation (MCS) is used to analyse the dynamic behaviour of built-up structures with uncertainties in the location of the joints. In this case, the MPC connections are used to model changes in the location of the joint instead of modifying the FE model from one sample to the next.

However, model validation is needed. In this chapter, the results from FE models with MPCs are compared to analytical solutions to evaluate the accuracy of these connections and to analyse the influence of the size and the type of element for which these MPCs are attached. Two different models are analysed: two infinite beams and two simply supported plates. In all of the models there is a single elastic connection with translational and rotational stiffnesses.

In the following section, the MPC joint model is described in detail. In Section 2.2 the MPC joint model is validated using a model of two infinite beams with a single elastic connection. In Section 2.3 the MPC joint model is validated using a model of two simply supported plates with a single elastic connection and the influence of the size and the type of element to which these MPCs are attached is analyzed. Finally, conclusions are given in section 2.4.

2.1 Multi point constraint elastic connection

The MPC elastic connection in this study consists of spring elements connected to the substructures using MPCs. The model is then a function of the position of the connection points (x', y') as shown in Figure 2.1. In the case of thin plate substructures with out-of-plane DOFs w, θ_x and θ_y, the elastic element contains a translational stiffness, K_w and two rotational stiffnesses, $K_{\theta x}$ and $K_{\theta y}$, as shown in Figure 2.1. The nodal forces and DOFs of the i^{th} connection are related by

$$\mathbf{F}_i' = \mathbf{K}_i'\mathbf{u}_i' = \begin{bmatrix} K_w & 0 & 0 & -K_w & 0 & 0 \\ 0 & K_{\theta x} & 0 & 0 & -K_{\theta x} & 0 \\ 0 & 0 & K_{\theta y} & 0 & 0 & -K_{\theta y} \\ -K_w & 0 & 0 & K_w & 0 & 0 \\ 0 & -K_{\theta x} & 0 & 0 & K_{\theta x} & 0 \\ 0 & 0 & -K_{\theta y} & 0 & 0 & K_{\theta y} \end{bmatrix} \begin{Bmatrix} w_i^{(1)\prime} \\ \theta_i^{(1)\prime} \\ \theta_i^{(1)\prime} \\ w_i^{(2)\prime} \\ \theta_i^{(2)\prime} \\ \theta_i^{(2)\prime} \end{Bmatrix} \tag{2.1}$$

hence, the stiffness matrix in the local connection DOFs $\mathbf{u}_i'$ is

$$\mathbf{K}'_i = \begin{bmatrix} \mathbf{K}''_i & -\mathbf{K}''_i \\ -\mathbf{K}''_i & \mathbf{K}''_i \end{bmatrix} \tag{2.2}$$

where

$$\mathbf{K}''_i = diag\begin{pmatrix} K_{iw} & K_{i\theta x} & K_{i\theta y} \end{pmatrix} \tag{2.3}$$

The DOFs $\mathbf{u}'_i$ can be related to the nodal DOFs of one of the substructures using MPCs. The MPC can be defined as the set of equations that relate each of the connection DOFs $\mathbf{u}'_i$ to the interface DOFs $\mathbf{u}_{cc}$, i.e.

$$\mathbf{u}_i'^{(1)} = \mathbf{G}_i^{(1)}(x_i'^{(1)}, y_i'^{(1)})\mathbf{u}_{cc}^{(1)} \tag{2.4}$$

$$\mathbf{u}_i'^{(2)} = \mathbf{G}_i^{(2)}(x_i'^{(2)}, y_i'^{(2)})\mathbf{u}_{cc}^{(2)} \tag{2.5}$$

where $\mathbf{G}_i^{(1)}$ and $\mathbf{G}_i^{(2)}$ are the matrix of coefficients of the MPC equations for the upper and lower plate respectively. In this case $\mathbf{G}_i^{(1)}$ and $\mathbf{G}_i^{(2)}$ are populated using the element shape functions. In doing so, the relationship between $\mathbf{u}'_i$ and $\mathbf{u}_{cc}$ is made consistent with the FE formulation and is a function of (x', y').

There are many methods available in the literature to apply MPCs to a FE model, e.g. static condensation [23], augmented Lagrange multipliers, Lagrange elimination etc. In this paper, static condensation is used.

In order to add *n* connections, a global connection matrix in $\mathbf{u}'_i$ coordinates is defined as

$$\Delta\mathbf{K}' = diag\begin{pmatrix} \mathbf{K}'_1 & \mathbf{K}'_2 & \mathbf{K}'_3 & \cdots & \mathbf{K}'_n \end{pmatrix} \tag{2.6}$$

Then a transformation matrix $\boldsymbol{\Gamma}$ that relates the $\mathbf{u}_i'$ to $\mathbf{u}_{cc}$ and imposes the coupling conditions between plates can be written as

$$\boldsymbol{\Gamma} = \begin{bmatrix} \mathbf{G}^{(1)} & -\mathbf{G}^{(2)} \end{bmatrix} \tag{2.7}$$

where

$$\mathbf{G}^{(1)} = diag\begin{pmatrix} \mathbf{G}_1^{(1)} & \mathbf{G}_2^{(1)} & \mathbf{G}_3^{(1)} & \cdots & \mathbf{G}_n^{(1)} \end{pmatrix} \tag{2.8}$$

$$\mathbf{G}^{(2)} = diag\begin{pmatrix} \mathbf{G}_1^{(2)} & \mathbf{G}_2^{(2)} & \mathbf{G}_3^{(2)} & \cdots & \mathbf{G}_n^{(2)} \end{pmatrix} \tag{2.9}$$

A second transformation matrix $\boldsymbol{\Xi}$ is defined to transform from $\mathbf{u}_{cc}$ to $\mathbf{p}$ coordinates as

$$\boldsymbol{\Xi} = \begin{bmatrix} \mathbf{0} & \mathbf{0} \\ \mathbf{0} & \mathbf{I} \end{bmatrix} \tag{2.10}$$

where $\mathbf{0}$ are zeros matrices of appropriate size. Then the stiffness matrix in $\mathbf{p}$ coordinates containing *n* connections is

$$\mathbf{K}_{MPC} = \left(\boldsymbol{\Gamma}\boldsymbol{\Xi}\right)^T \Delta\mathbf{K}' \, \boldsymbol{\Gamma}\boldsymbol{\Xi} \tag{2.11}$$

The resulting nodal forces in the joint are

$$\mathbf{F} = \mathbf{K}_{MPC}\mathbf{u}_{cc} \tag{2.12}$$

The substructures DOFs $\mathbf{u}_{cc}$ can be partitioned as

$$\begin{bmatrix} \mathbf{F}_1 \\ \mathbf{F}_2 \end{bmatrix} = \begin{bmatrix} \mathbf{K}_{MPC}^{(11)} & \mathbf{K}_{MPC}^{(12)} \\ \mathbf{K}_{MPC}^{(21)} & \mathbf{K}_{MPC}^{(22)} \end{bmatrix} \begin{bmatrix} \mathbf{u}_{cc}^{(1)} \\ \mathbf{u}_{cc}^{(2)} \end{bmatrix} \tag{2.13}$$

where $\mathbf{u}_{cc}^{(1)}$ and $\mathbf{u}_{cc}^{(2)}$ are the DOFs in substructure (1) and substructure (2) respectively.

2.2 Validation of a multipoint constraint spot-weld model for a one dimensional system.

This section investigates the validation of use of MPCs for connecting FE models and their ability to locate a connection anywhere between nodes. To avoid effects due to resonances and to simplify the evaluation, the joint is placed in a model of two infinite Euler-Bernoulli beams joined by a single connection. The transfer mobility from the upper to the lower beam as shown in Figure 2.2, is evaluated using two different FE models; one with an MPC elastic connection and the second with a node-to-node connection. Finally, the results are compared to an exact analytical solution.

2.2.1 Numerical models

To model an infinite beam model, the region of the elastic connection is modelled using Euler-Bernoulli beam finite elements and then attached to semi-infinite Spectral Elements (SEs) as shown in Figure 2.3.

An infinite beam structure can be incorporated into the FE model using the SE method. The SE approach is similar to the FE method, but the element matrix is defined via the dynamic stiffness relationships in the frequency domain [24]. A SE element that extends to infinity and is connected at a single point can be created; this element simulates a semi-infinite medium and can be connected to any node in a FE model according to the method described by Doyle [24].

Two different SEs were created, a) one semi-infinite beam that extends to $+\infty$ and b) one that extends to $-\infty$ as shown in Figure 2.4.

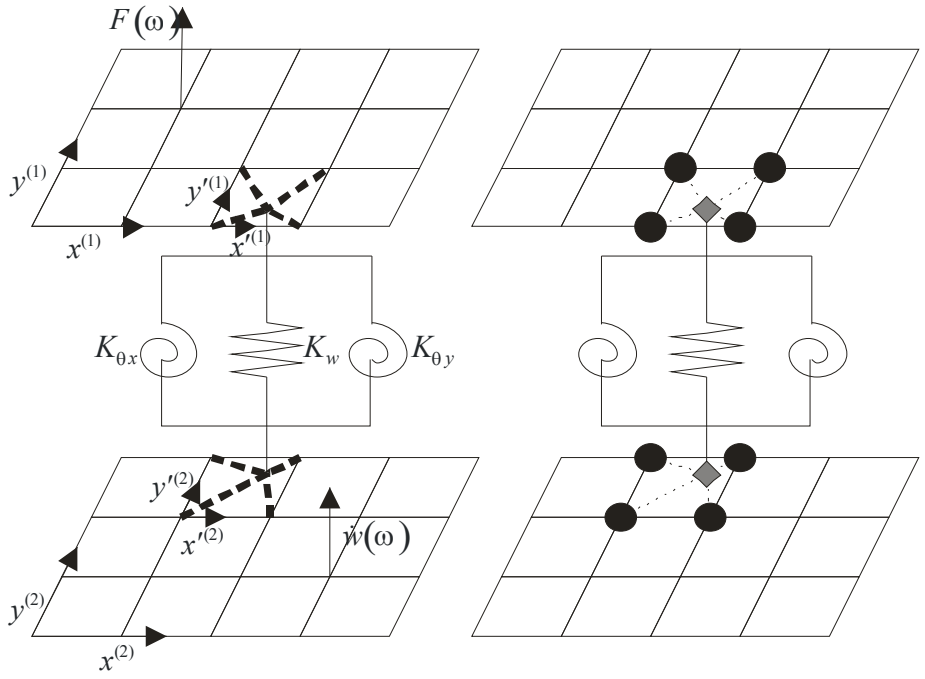

Figure 2.1: MPC elastic connection for plate bending analysis: ◆ joint DOFs $\left(\mathbf{u}_i'\right)$; ● substructure DOFs involved in the connection $\left(\mathbf{u}_{cc}\right)$.

The harmonic nodal forces are related to the nodal displacements as

$$\begin{Bmatrix} Q_1 \\ M_1 \end{Bmatrix} = EI \begin{bmatrix} -(1-i)k_b{}^3 & ik_b{}^2 \\ ik_b{}^2 & (1+i)k_b \end{bmatrix} \begin{Bmatrix} w^{(1)} \\ \theta_x^{(1)} \end{Bmatrix} \tag{2.14}$$

and

$$\begin{Bmatrix} Q_2 \\ M_2 \end{Bmatrix} = EI \begin{bmatrix} -(1-i)k_b{}^3 & -ik_b{}^2 \\ -ik_b{}^2 & (1+i)k_b \end{bmatrix} \begin{Bmatrix} w^{(2)} \\ \theta_x^{(2)} \end{Bmatrix} \tag{2.15}$$

where

$$k_b = \sqrt[4]{\frac{\omega^2 \rho A}{EI}} \tag{2.16}$$

is the beam flexural wave number equal to $2\pi/\lambda$, λ being the corresponding wavelength. The dynamic stiffness of a semi-infinite beam that extends to $+\infty$ is then given by

$$\mathbf{D}_{se}^{(1)} = EI\begin{bmatrix} -(1-i)k_b^{\,3} & ik_b^{\,2} \\ ik_b^{\,2} & (1+i)k_b \end{bmatrix} \qquad x \geq 0 \tag{2.17}$$

and the dynamic stiffness matrix for a beam that extends to $-\infty$ is given by

$$\mathbf{D}_{se}^{(2)} = EI\begin{bmatrix} -(1-i)k_b^{\,3} & -ik_b^{\,2} \\ -ik_b^{\,2} & (1+i)k_b \end{bmatrix} \qquad x \leq 0 \tag{2.18}$$

The SEs are connected to the FEs in a similar way in which two FEs are connected, but instead of connecting the mass and stiffness matrices, the dynamic stiffness matrix of the FEs is connected to the dynamic stiffness matrix of the SEs.

$$\mathbf{D}_{fe} = \mathbf{K} - \omega^2\mathbf{M} \tag{2.19}$$

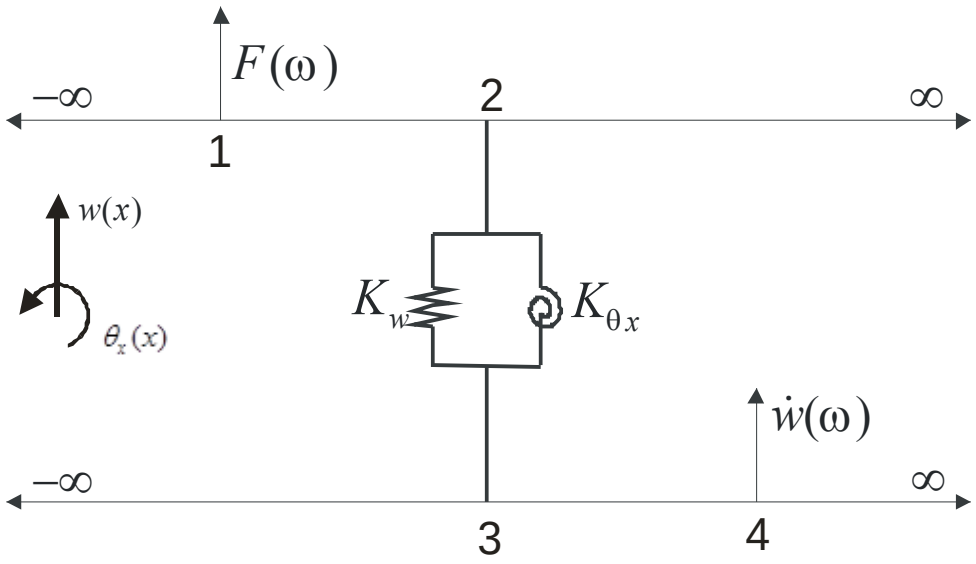

Figure 2.2: Two infinite beams connected with an elastic connection.

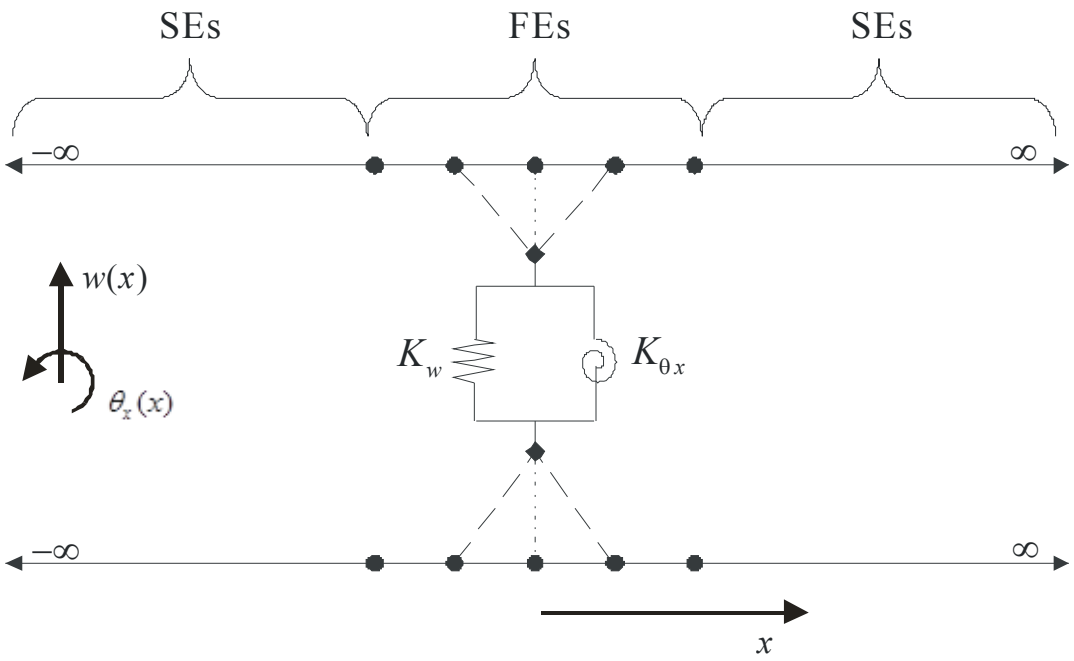

Figure 2.3: FE-SE Model of two infinite beams joined by a translational and a rotational spring.

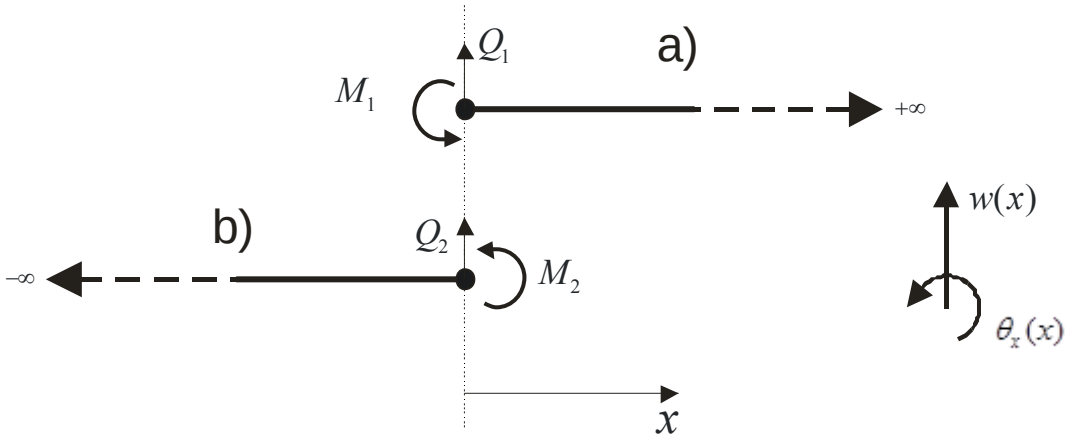

Figure 2.4: Semi-infinite SEs. Q_1 and Q_2 are the applied forces. M_1 and M_2 are the applied moments.

2.2.2 Node to node connection

The nodal force matrix $\mathbf{F}'$ of a connecting element comprising a translational and a rotational spring can be expressed as

$$\mathbf{F}' = \mathbf{K}'\mathbf{u}' = \begin{bmatrix} K_w & 0 & -K_w & 0 \\ 0 & K_{\theta x} & 0 & -K_{\theta x} \\ -K_w & 0 & K_w & 0 \\ 0 & -K_{\theta x} & 0 & K_{\theta x} \end{bmatrix} \begin{Bmatrix} w^{(1)\prime} \\ \theta_x^{(1)\prime} \\ w^{(2)\prime} \\ \theta_x^{(2)\prime} \end{Bmatrix} \tag{2.20}$$

where $\mathbf{K}'$ is the joint stiffness matrix in the local DOFs Δ'; w, K_w and $K_{\theta x}$ are the rotational and translational stiffness of the elastic connection as shown in Figure 2.3 and $w^{(1)}$ and $\theta_x^{(1)}$ and $w^{(2)}$ and $\theta_x^{(2)}$ are the local DOFs at the connection node belonging to sibstructure 1 and 2 respectively. $\mathbf{K}'$ can be transformed into global DOFs as

$$\mathbf{K}_{joint} = \mathbf{A}^T\mathbf{K}'\mathbf{A} \tag{2.21}$$

where $\mathbf{K}_{joint}$ is the joint stiffness matrix in global co-ordinates and $\mathbf{A}$ is a transformation matrix that relates the local to the global DOFs [25].

2.2.3 Multipoint constraint connection

The local DOFs of the joint element in equation (2.20) can be related to one or more DOFs in the global matrices using a MPC equation. The same method described in section 2.1 can be used. In this case the model is assembled as shown in Figure 2.3. The $\mathbf{G}^{(1)}$ and $\mathbf{G}^{(2)}$ matrices in equations (2.4) and (2.5) are expressed as

$$\mathbf{G}^{(1)} = \begin{bmatrix} N_1(\xi'^{(1)}) & aN_2(\xi'^{(1)}) & N_3(\xi'^{(1)}) & aN_4(\xi'^{(1)}) \\ \dfrac{N_1'(\xi'^{(1)})}{a} & N_2'(\xi'^{(1)}) & \dfrac{N_3'(\xi'^{(1)})}{a} & N_4'(\xi'^{(1)}) \end{bmatrix} \tag{2.22}$$

$$\mathbf{G}^{(2)} = \begin{bmatrix} N_1(\xi'^{(2)}) & aN_2(\xi'^{(2)}) & N_3(\xi'^{(2)}) & aN_4(\xi'^{(2)}) \\ \dfrac{N_1'(\xi'^{(2)})}{a} & N_2'(\xi'^{(2)}) & \dfrac{N_3'(\xi'^{(2)})}{a} & N_4'(\xi'^{(2)}) \end{bmatrix} \tag{2.23}$$

where

$$N_1(\xi) = \frac{1}{4}(2 - 3\xi + \xi^3) \tag{2.24}$$

$$N_2(\xi) = \frac{1}{4}(1 - \xi - \xi^2 + \xi^3) \tag{2.25}$$

$$N_3(\xi) = \frac{1}{4}(2 + 3\xi - \xi^3) \tag{2.26}$$

$$N_4(\xi) = \frac{1}{4}(-1 - \xi + \xi^2 + \xi^3) \tag{2.27}$$

are the parametric shape functions for a FE Euler-Bernoulli beam and

$$\xi' = \left(\frac{x' - a}{a} \right) \tag{2.28}$$

is the normalized co-ordinate, $a = s/2$ where s is the element length.

2.2.4 Analytical solution

Appendix A gives the equations governing the system in Figure 2.2 using a mobility approach, and it also describes the derivation of the transfer mobility from a force excitation applied at point 1 on the first beam to a response evaluated at point 4 on the second beam.

Solving the equations in appendix A, the velocities of beams 1 and 2 at the connection point are given by

$$\begin{bmatrix} \mathbf{V}_C^{(1)} \\ \mathbf{V}_C^{(2)} \end{bmatrix} = \left[\mathbf{I} - \begin{bmatrix} \mathbf{Y}_{2,2}^{(1)} & 0 \\ 0 & \mathbf{Y}_{3,3}^{(2)} \end{bmatrix} \mathbf{Z}_c \right]^{-1} \begin{bmatrix} \mathbf{Y}_{1,2}^{(2)} \\ 0 \end{bmatrix} \mathbf{F}_{ext} \tag{2.29}$$

where

$$\mathbf{Z}_c = i\omega \begin{bmatrix} K_w & 0 & -K_w & 0 \\ 0 & K_{\theta x} & 0 & -K_{\theta x} \\ -K_w & 0 & K_w & 0 \\ 0 & -K_{\theta x} & 0 & K_{\theta x} \end{bmatrix} \tag{2.30}$$

is the impedance of the connection and

$$\mathbf{Y}_{i,j}^{(k)} = \begin{bmatrix} Y_{i,j}^{v,F} & Y_{i,j}^{v,M} \\ Y_{i,j}^{\psi,F} & Y_{i,j}^{\psi,M} \end{bmatrix} \tag{2.31}$$

is the mobility matrix from point i to point j for the k^{th} Euler-Bernoulli beam [26].

2.2.5 Numerical Examples

The numerical example is a system of two infinite beams joined together by an elastic connection. To simplify the analysis all simulations were divided into two cases; the first of which only the effects of a translational spring K_w are analyzed and the second for which only $K_{\theta x}$ is considered in order to analyze the effects of a rotational spring. The values used for K_w and $K_{\theta x}$ are 10^6 N/m and 10^4 Nm/rad respectively. Both beams were assumed to be identical and the properties are given in Table 2-1.

The mobility of the translational connection is fully imaginary (i.e. related to stiffness), when compared to the imaginary part of the mobility of the connected beams (i.e. the beams' stiffness) and setting them equal, a critical frequency ω_0 can be found, i.e.

$$\omega_0 = \left(\frac{K_W}{2EI}\right)^{\frac{2}{3}} \left(\frac{EI}{\rho A}\right)^{\frac{1}{2}} \tag{2.32}$$

much below ω_0 the spring is effectively rigid and the behaviour of the assembly is that of two beams bending in parallel with no relative displacement at the connection. Much above ω_0 the spring is flexible and works as an isolator between the two beams.

When the mobility of the rotational connection is compared to the imaginary part of the mobility of the connected beams, two critical frequencies appear ω_1 and ω_2, i.e.

$$\omega_1 = \frac{{K_R}^2}{2(\rho A)^{1/2}(EI)^{3/2}} \text{ and } \omega_2 = \left(\frac{1}{x_e + x_r}\right)^2 \cdot \left(\frac{EI}{\rho A}\right)^{\frac{1}{2}} \tag{2.33}$$

where x_e and x_r are the excitation and response coordinates from the origin. ω_1 is equivalent to ω_0 but for the rotational DOF, ω_2 is not physically meaningful but represents a change in the slope of the FRF. Given the stiffness value and the beams' properties ($EI = 2.23\times10^4$ Nm^2, $\varphi A = 23.58$ kg/m) used in the present example, one has $\omega_0 = 654$ rad/s, $\omega_1 = 81.56$ rad/s and $\omega_2 = 11574$ rad/s.

The transfer mobility from the upper beam a position $x = -0.01$m in the upper beam to a position $x = 0.01$m in the lower beam was evaluated using two different FE models; the first using a MPC connection and the second using a node to node connection. Finally both solutions were compared to the analytical result.

2.2.5.1 Accuracy of FE models: a single translational spring connection

Figure 2.5 shows the comparison between the results from both FE models and the analytical solution for the translational stiffness case. When the spring is connected from node to node (see Figure 2.3), the result for the transfer mobility is not exact due to FE discretization errors.

	Cross Section	b (m)	h (m)	ρ (kg/m^3)	E (N/m^2)	υ
Beams (1&2)	Rectangular	0.5	0.006	7860	2.07E+11	0.3

Table 2-1: Beam properties

When the beam wave number k_b and the element length s are multiplied and squared $(k_b s)^2$, a non dimensional frequency is defined. When the mobility is plotted using this non dimensional frequency as the abscissa it is possible to compare the accuracy of different FE models with different element size. The frequencies corresponding to $s = \lambda/6$, $s = \lambda/3$ and $s = \lambda$ are added for reference. Figure 2.5 shows the comparison between the exact solution and the prediction using the FE-SE model. It can be seen that the prediction agrees with the exact solution and it starts to deviate for frequencies slightly above the frequencies where $s > \lambda/3$. If $s > \lambda$ the solution is very inaccurate. These errors are expected from any FE model, since as a rule of thumb the predictions from a FE model are accurate up to a frequency for which $s = \lambda/6$. If the element shape functions are quadratic, as used in this study, then the accuracy limit increases up to frequencies where $s = \lambda/3$.

When the results from the MPC connection model are compared, it can be seen that the prediction agrees very well with the exact solution and starts to differ at frequencies slightly lower than frequencies where $s > \lambda/3$; therefore it is marginally less accurate than the node to node connection. This is explained by the fact that the displacements

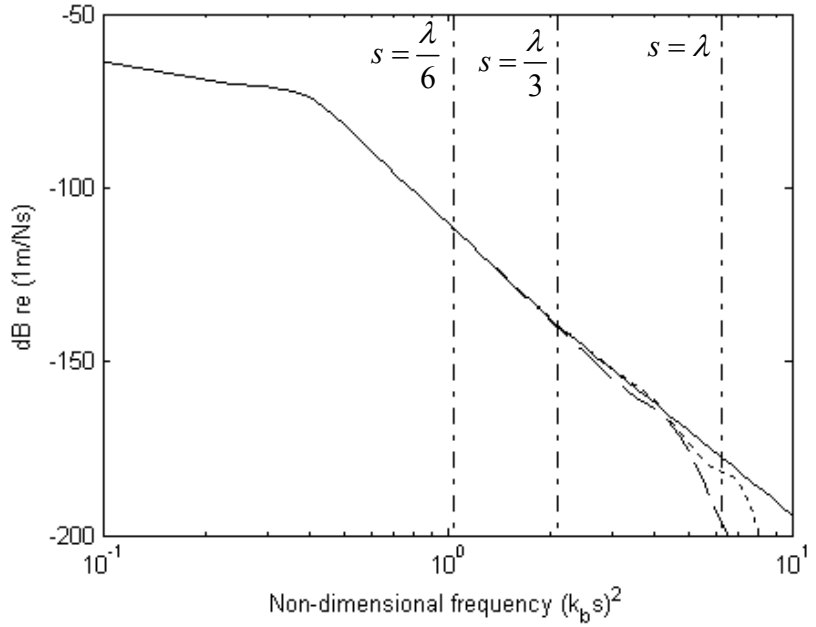

Figure 2.5: Magnitude of the transfer mobility for a system of two infinite beams with a single elastic translational connection: —— analytical solution; – – – · MPC connection; - - - - - node to node connection.

of the connection nodes depend on the shape functions of the element to which it is connected when a MPC is used; therefore additional discretization errors are introduced into the solution.

However, these additional errors are small and the agreement between both models is very good at low frequencies, especially at frequencies corresponding to $s < \lambda / 6$.

2.2.5.2 Accuracy of FE models: a single rotational spring connection

When the node to node connection is used, the transfer mobility can be predicted with good accuracy at low frequencies as can be seen in Figure 2.6. The solution obtained with the node to node FE-SE model is accurate for frequencies where $s < \lambda / 3$. At higher frequencies, the solution starts to deviate from the analytical solution. Similar to the translational stiffness connection, when a MPC connection is used to connect the rotational spring the response starts to deviate significantly from the analytical solution at slightly lower frequencies compared to the node to node connection.

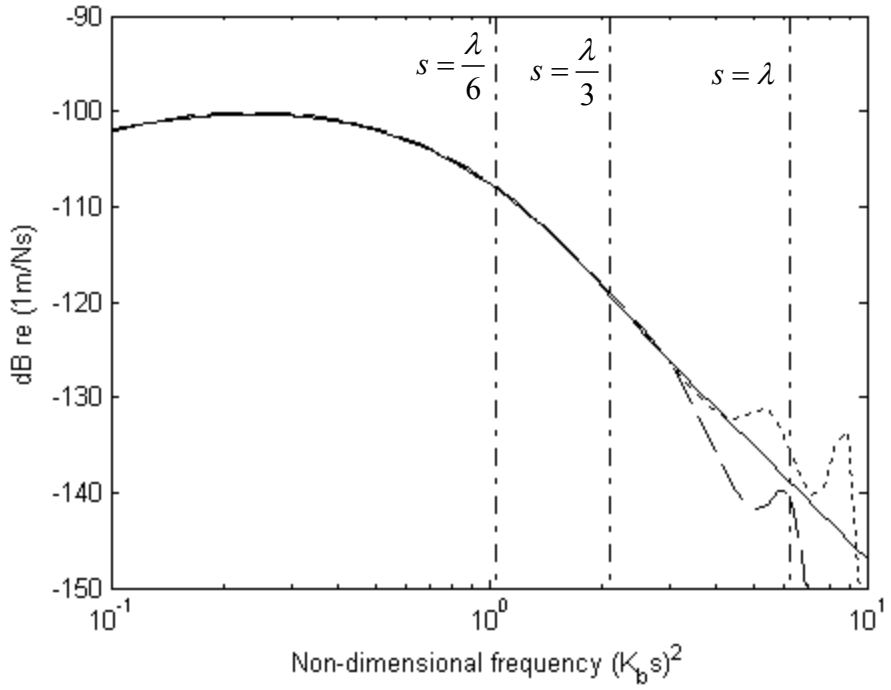

Figure 2.6: Transfer mobility magnitude in a system of two infinite beams with a single elastic rotational connection: —— analytical solution; - - - - - MPC connection; – – – · node to node connection.

2.3 Validation of a multipoint constraint spot weld model for two dimensional systems.

When plates are connected with an MPC connection, the MPC coefficient matrices are populated using the element shape functions. Therefore it is important to analyze the formulation of the plate element that is being used.

There are two main different plate theories [27]. The first is Kirchoff plate theory, in which the effects of transverse shear deformation and rotary inertia are neglected. Kirchoff plate theory is applicable to thin plates in which the plate thickness is much smaller than the bending wavelength. The second is Mindlin-Reissner theory. Here the transverse shear and rotary inertia become important when describing the plate behaviour, and it is often used to analyze thick plates.

When Kirchoff plate theory is used, the element results in a non-conforming formulation or alternately in a conforming formulation with additional DOFs [25]; the non-conforming formulation could result in incompatibilities with the MPC equations, whilst the conforming formulation is difficult to assemble due to the additional DOFs.

Alternatively, when Mindlin-Reissner theory is used [27], the transverse shear strain is independent of the thickness of the plate. Therefore as the plate thickness decreases, the strain energy associated with transverse shear tends to dominate the response, rather than tending to zero as in the Kirchoff plate theory. This phenomenon is referred to as "shear locking" and leads to an overly stiff prediction of the response. One approach to reducing the effects of shear locking is to use a reduced number of Gauss integration points when evaluating the shear stiffness of an element [28], [29]. In effect, this reduces the order of the interpolation for the transverse shear strain to that used in the Gauss integration scheme. In general this approach can lead to rank deficiency of the stiffness matrix and a singular set of equations. However, by appropriate selection of the element basis functions and integration schemes, it is possible to obtain a robust element known as the Heterosis plate element [30].

In this section the ability of the MPC connection to be located anywhere in an element is tested for two different element formulations, namely a non-conforming thin plate rectangular element [25] and a heterosis plate element [28].

A system of two simply supported plates with a single elastic connection is used. The transfer mobility from the upper plate to the lower plate is evaluated using two different FE models; one with an MPC elastic connection and the second with a node-to-node connection. Results are then compared to an analytical solution.

2.3.1 Finite element formulations

2.3.1.1 Thin plate rectangular element (Non conforming)

This is a four noded element, with one node at each corner. Each node has three DOFs which describe flexural motion, vertical displacement w and two rotations θ_x and θ_y as can be observed in Figure 2.7. It is based on Kirchoff plate theory, therefore it is assumed that

$$\theta_x = \frac{\partial w}{\partial y} \text{ and } \theta_y = -\frac{\partial w}{\partial x} \tag{2.34}$$

The displacement function can be described in terms of the normalised coordinates ξ and η as

$$w = [\mathbf{N}_1(\xi,\eta) \quad \mathbf{N}_2(\xi,\eta) \quad \mathbf{N}_3(\xi,\eta) \quad \mathbf{N}_4(\xi,\eta)]\mathbf{w}_e \tag{2.35}$$

where $\mathbf{w}_e$ is a vector that contains the element DOFs and

$$\mathbf{N}_j^T(\xi,\eta)=\begin{bmatrix}\frac{1}{8}(1+\xi_j\xi)(1+\eta_j\eta)(2+\xi_j\xi+\eta_j\eta-\xi^2-\eta^2)\\ \frac{b}{8}(1+\xi_j\xi)(\eta_j+\eta)(\eta^2-1)\\ \frac{a}{8}(1+\eta_j\eta)(\xi_j+\xi)(\xi^2-1)\end{bmatrix} \tag{2.36}$$

are the element shape functions, where $(\xi_j,\eta_j), j=1,2,3,4$ are the normalized coordinates of each of the element nodes.

The rotations θ_x and θ_y are evaluated using equations (2.34) and (2.35). When doing so it is noted that θ_y is determined by the values of w and θ_x at the four nodes as well as by the values of θ_y at nodes 2 and 3. This indicates that when elements are assembled, θ_y is discontinuous between nodes. Similarly θ_x is also discontinuous between nodes. This is therefore a non-conforming element.

2.3.1.2 Heterosis element

The Heterosis plate element [28] is a nine-noded plate element that is based on Mindlin -Reissner plate theory and is shown in Figure 2.8. The central node has two rotations and each other node has 5 DOFs which describe in-plane and out-of-plane motion (42 DOF in total). The displacement field within the element is interpolated using serendipity basis functions, whilst the rotations in the *x* and *y* directions are interpolated using Lagrange basis functions. Reduced order integration is used to evaluate the shear stiffness matrix. This element does not suffer from shear locking and possesses correct rank. The out of plane co-ordinates (w,θ_x,θ_y) of a point within the element can be described as

$$w=\sum_{j=1}^{8}\boldsymbol{N}_j w_j \tag{2.37}$$

$$\theta_x = \sum_{j=1}^{9} \boldsymbol{P}_j \theta_{x,j} \tag{2.38}$$

$$\theta_y = \sum_{j=1}^{9} \boldsymbol{P}_j \theta_{y,j} \tag{2.39}$$

where j indicates the node number and

$$\boldsymbol{N}_j = \frac{1}{4}\left(1+\xi_j\xi\right)\left(1+\eta_j\eta\right)\left(\xi_j\xi+\eta_j\eta-1\right), \qquad j=1,3,5,7 \tag{2.40}$$

$$\boldsymbol{N_j} = \frac{\xi_j^{\,2}\left(1+\xi_j\xi\right)\left(1-\eta^2\right)}{2} + \frac{\eta_j^{\,2}\left(1+\eta_j\eta\right)\left(1-\xi^2\right)}{2}, \qquad j=2,4,6,8 \tag{2.41}$$

$$\boldsymbol{P}_j = \left(\frac{\xi_j\xi\left(1+\xi_j\xi\right)}{2}+\left(1-\xi^2\right)\left(1-\xi_j^{\,2}\right)\right)\left(\frac{\eta_j\eta\left(1+\eta_j\eta\right)}{2}+\left(1-\eta^2\right)\left(1-\eta_j^{\,2}\right)\right), j=1-9 \tag{2.42}$$

are vectors of Lagrange and serendipity basis functions respectively.

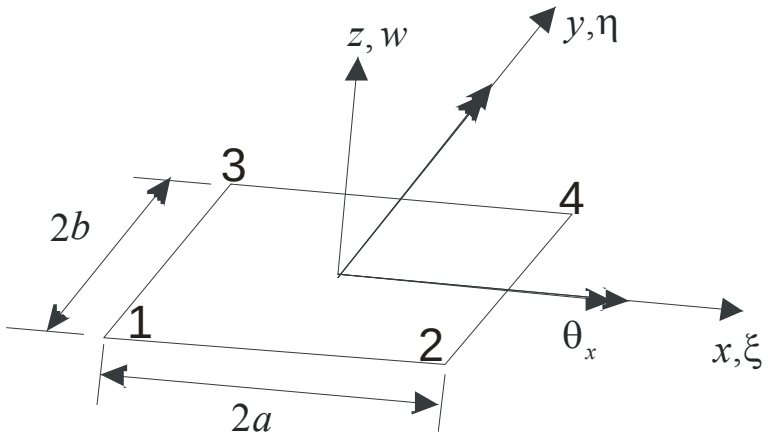

Figure 2.7: Geometry and coordinate system of a rectangular element.

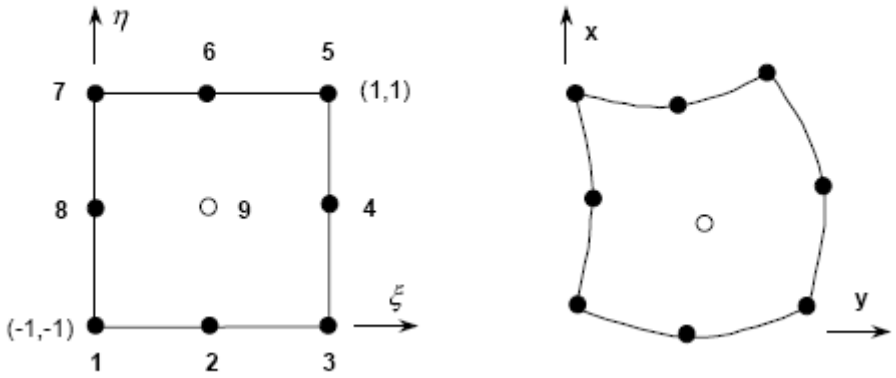

Figure 2.8: Node numbering for Heterosis element.

2.3.2 Type of connection

2.3.2.1 Node to node connection

In the case of thin plate substructures with out-of-plane DOFs w, θ_x and θ_y, the elastic element contains a translational stiffness K_w and two rotational stiffnesses $K_{\theta x}$ and $K_{\theta y}$, as shown in Figure 2.1.

The nodal forces and DOFs of the point connection are related by equation (2.1)

$\mathbf{K}'$ can be transformed into global DOFs as

$$\mathbf{K}_{joint} = \mathbf{A}^T \mathbf{K}' \mathbf{A} \tag{2.43}$$

where $\mathbf{K}_{joint}$ is the joint stiffness matrix in global co-ordinates and $\mathbf{A}$ is a transformation matrix that relates the local to the global DOFs [25].

2.3.2.2 Multipoint constraint connection

As described in 2.1, the local DOFs of the joint element in equation (2.1) can be related to one or more DOFs in the global matrices using a MPC equations. In this case the

model is assembled as shown in Figure 2.1, where the **G** matrix in equation (2.4) and (2.5) is given by

$$\mathbf{G}^{(1)}\left(x'^{(1)}, y'^{(1)}\right) = \begin{bmatrix} \mathbf{N}_1 & \mathbf{N}_2 & \mathbf{N}_3 & \mathbf{N}_4 \\ \dfrac{\partial \mathbf{N}_1}{\partial y} & \dfrac{\partial \mathbf{N}_2}{\partial y} & \dfrac{\partial \mathbf{N}_3}{\partial y} & \dfrac{\partial \mathbf{N}_4}{\partial y} \\ -\dfrac{\partial \mathbf{N}_1}{\partial x} & -\dfrac{\partial \mathbf{N}_2}{\partial x} & -\dfrac{\partial \mathbf{N}_3}{\partial x} & -\dfrac{\partial \mathbf{N}_4}{\partial x} \end{bmatrix} \tag{2.44}$$

where $\mathbf{N}_j$ are the element shape functions for node j as defined in equation (2.36). When heterosis elements are used, $\mathbf{G}^{(1)}$ is defined as

$$\mathbf{G}^{(1)} = \begin{bmatrix} \mathbf{N}^{(1)} & 0 & 0 \\ 0 & \mathbf{P}^{(1)} & 0 \\ 0 & 0 & \mathbf{P}^{(1)} \end{bmatrix} \tag{2.45}$$

where

$$\mathbf{P}^{(1)} = \begin{bmatrix} \boldsymbol{P}_1 & \boldsymbol{P}_2 & \boldsymbol{P}_3 & \boldsymbol{P}_4 & \boldsymbol{P}_5 & \boldsymbol{P}_6 & \boldsymbol{P}_7 & \boldsymbol{P}_8 & \boldsymbol{P}_9 \end{bmatrix} \tag{2.46}$$

is the vector of serendipity basis functions for substructure as defined in equation (2.42) and

$$\mathbf{N}^{(1)} = \begin{bmatrix} \boldsymbol{N}_1 & \boldsymbol{N}_2 & \boldsymbol{N}_3 & \boldsymbol{N}_4 & \boldsymbol{N}_5 & \boldsymbol{N}_6 & \boldsymbol{N}_7 & \boldsymbol{N}_8 \end{bmatrix} \tag{2.47}$$

Is the vector of Lagrange basis functions for substructure i as defined in equations (2.40) and (2.41) and the same for $\mathbf{G}^{(2)}$.

2.3.3 Analytical solution

In this section the transfer mobility for the system in Figure 2.9 is derived, thin plate theory being used.

Appendix B shows the equations governing the system in Figure 2.9 using a mobility approach, and it also describes the derivation of the transfer mobility from a force excitation applied at point 1 on the first plate to a response evaluated at point 4 on the second plate.

Solving the equations in appendix A, the velocities at plate 1 and plate 2 at the connection are given by

$$\begin{bmatrix} \mathbf{V}_C^{(1)} \\ \mathbf{V}_C^{(2)} \end{bmatrix} = \left[\mathbf{I} - \begin{bmatrix} \mathbf{Y}_{2,2}^{(1)} & 0 \\ 0 & \mathbf{Y}_{3,4}^{(2)} \end{bmatrix} \mathbf{Z}' \right]^{-1} \begin{bmatrix} \mathbf{Y}_{1,2}^{(2)} \\ 0 \end{bmatrix} \mathbf{F}_{ext} \tag{2.48}$$

where

$$\mathbf{Z}' = i\omega \mathbf{K}' \tag{2.49}$$

is the transfer impedance of the connection, and

$$\mathbf{Y}_{i,j}{}^{(k)} = \begin{bmatrix} Y_{i,j}^{w,F} & Y_{i,j}^{w,M_x} & Y_{i,j}^{w,M_y} \\ Y_{i,j}^{\theta_x,F} & Y_{i,j}^{\theta_x,M_x} & Y_{i,j}^{\theta_x,M_y} \\ Y_{i,j}^{\theta y,F} & Y_{i,j}^{\theta_y,M_x} & Y_{i,j}^{\theta_y,M_y} \end{bmatrix} \tag{2.50}$$

are the mobility matrices from point i to point j for plate k. The terms in matrix (2.50) are calculated for thin rectangular plates in terms of a modal summation [26].

2.3.4 Numerical example

The numerical example is a system of two simply supported parallel plates with an elastic connection as shown in Figure 2.9. The properties for each plate are given in Table 2-2. To simplify the analysis all simulations were divided into two cases; the first in which only the effects of a translational spring K_w are analyzed and the second in which only $K_{\theta x}$ is considered in order to analyze the effects of a rotational spring. The values used for K_w and $K_{\theta x}$ are $16000\,\mathrm{N/m}$ and $1600\,\mathrm{Nm/rad}$ respectively. Damping is introduced as a modal loss factor $\eta = 0.02$.

The transfer mobility from coordinate (0.38, 0.32) in plate 1 to coordinate (0.38, 0.32) in plate 2 as shown in Figure 2.9 was evaluated. In this example, the co-ordinates of the spring (x_c, y_c) are $(0.1227, 0.1614)$ in both plates.

When the MPC connection is incorporated, the plates are modelled using a mesh of 11×11 identical elements. The co-ordinates of the spring correspond to $(2.25 s_x, 3.5 s_y)$, where s_x is the element length in the x direction and s_y is the element size in the y direction. The local co-ordinates of the connection within the element are $(x', y') = (0.25 s_x, 0.5 s_y)$. For the node to node connection a mesh of 22×22 elements is used in order to have a node exactly at the elastic connection location.

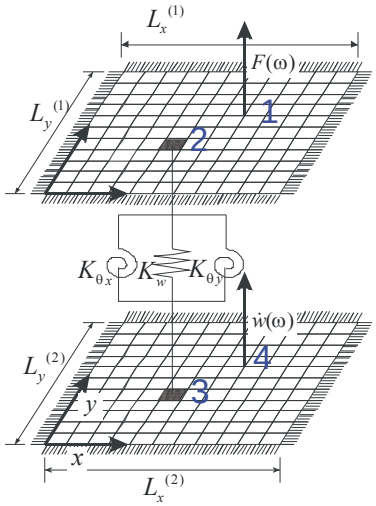

Figure 2.9: Two parallel simply supported plates assembled with an elastic point connection.

	L_x (m)	L_y (m)	h (m)	ρ (Kg/m^3)	E (N/m^2)	υ
Component (1)	0.6	0.5	0.006	7860	2.07E+11	0.3
Component (2)	0.6	0.5	0.012	7860	2.07E+11	0.35

Table 2-2: Properties of each thin plate component for the numerical example.

When Heterosis elements are used to predict the transfer mobility, in the case of a connection with translational stiffness K_w, both connection models have almost identical behaviour and are in very good agreement when compared to the analytical solution. Only FE discretization errors are present at higher frequencies as can be observed in Figure 2.10. At resonance the difference in magnitude between the analytical and numerical solution is negligible and the first natural frequency is overestimated by approximately 0.5 Hz, whilst the second natural frequency is overestimated by approximately 0.3 Hz as shown in Figure 2.11(a) and Figure 2.11(b). These differences are small and consistent between FE models.

In the case of a connection with rotational stiffness $K_{\theta x}$, both connection models are in good agreement with each other, but there are differences when compared to the analytical solution, especially at low frequencies where a difference of approximately 2dB can be observed in Figure 2.12. These discrepancies are mainly caused by

convergence issues in the modal summation when rotational DOFs are involved. The natural frequencies are overestimated by the same amount as in the translational stiffness case, as can be observed in Figure 2.13. In spite of these differences, the performance of the Heterosis elements connected by MPCs is acceptable, having the same frequency limitation as typical FE models.

When thin plate elements are assembled using a node to node connection, the predictions are comparable to the results obtained from the Heterosis element. In some cases this prediction is closer to the analytical solution, as can be observed in Figure 2.10 to Figure 2.13. On the other hand, when thin plates are connected using MPCs the solution is significantly in error and different from the analytical solution, as can be observed in Figure 2.10 and Figure 2.12. The error is generated when the MPCs are attached to the non-conforming elements, for which θ_y is discontinuous between nodes in the individual plates. Hence, an important overall conclusion is that MPC connections should not be implemented on any model comprising thin plate non-conforming elements.

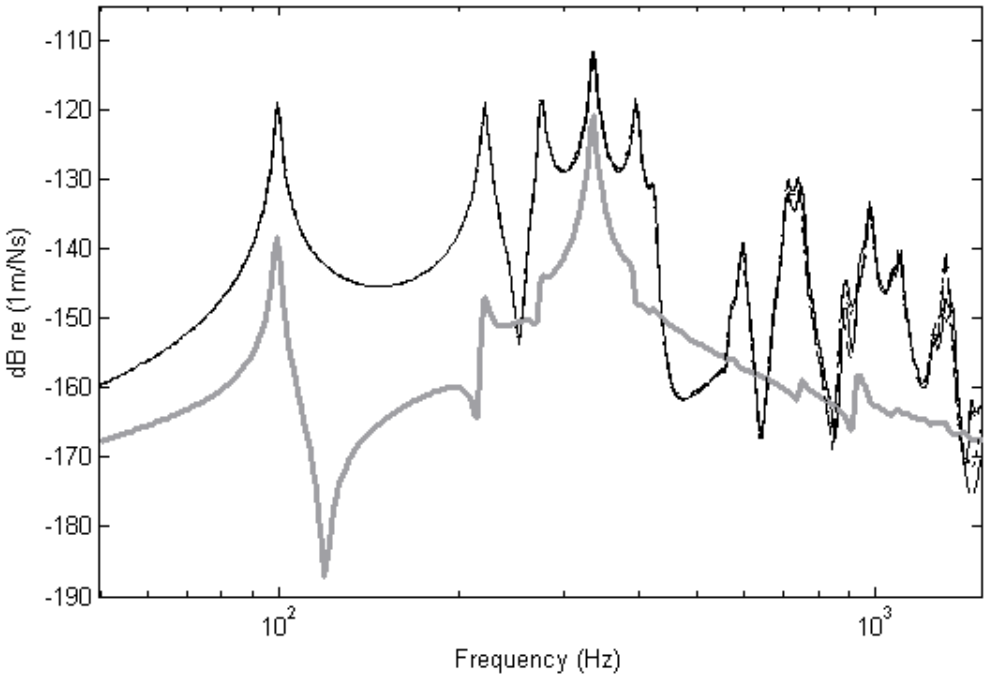

Figure 2.10: Magnitude of the transfer mobility for a system of two simply supported plates with a single elastic connection with translational stiffness: ——analytical solution; - - - - - node to node-heterosis; – – – MPC-heterosis; – · – · node to node-thin; ——— MPC-thin.

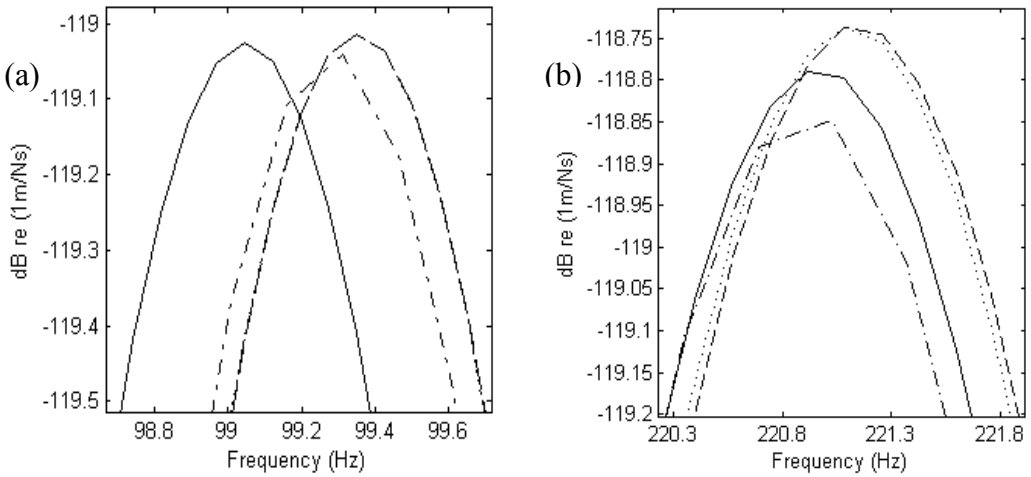

Figure 2.11: Magnitude of the transfer mobility for a system of two simply supported plates with a single elastic connection with translational stiffness: (a) first resonance ; (b) second resonance: —— analytical solution; - - - - - node to node-heterosis; – – – MPC-heterosis; – · – · node to node-thin.

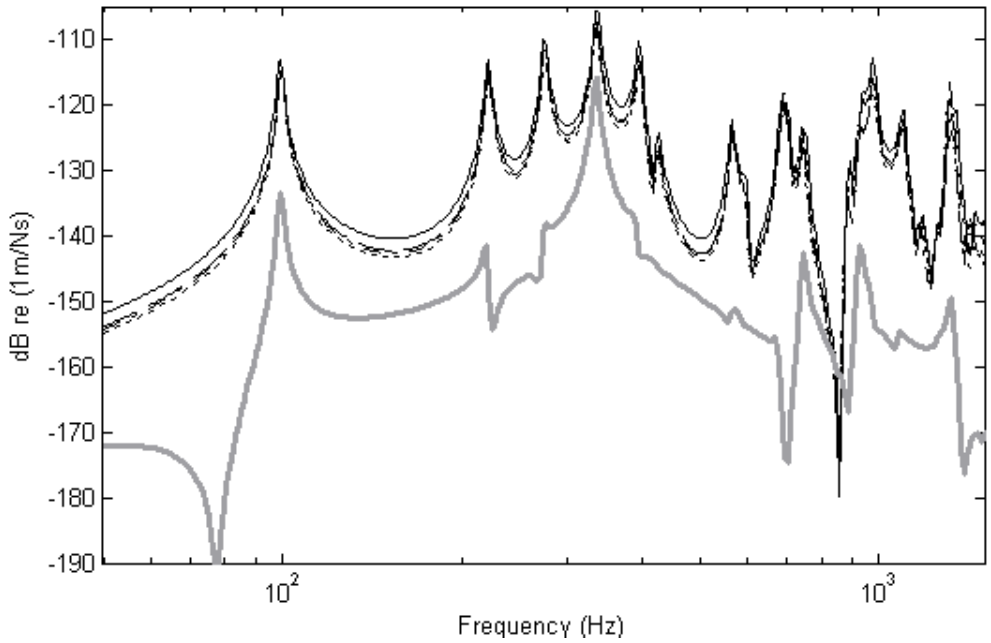

Figure 2.12: Magnitude of the transfer mobility for a system of two simply supported plates with a single elastic connection with rotational stiffness: ——analytical solution; - - - - - node to node-heterosis; – – – MPC-heterosis; – · – · node to node-thin; —— MPC-thin.

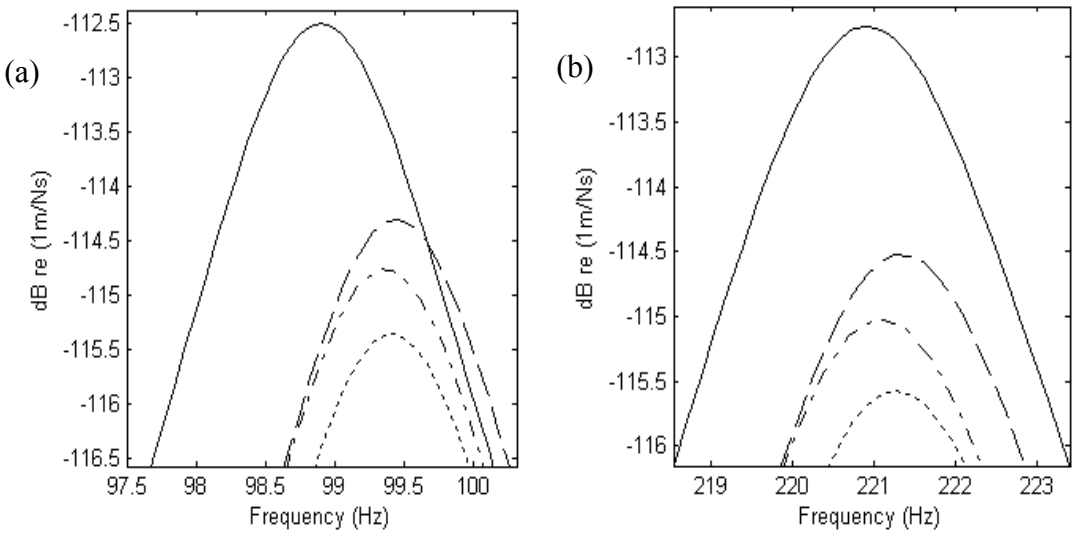

Figure 2.13: Magnitude of transfer mobility in a system of two simply supported plates with a single elastic connection with rotational stiffness: (a) first resonance; (b) second resonance: —— analytical solution; - - - - - node to node-heterosis; – – – MPC-heterosis; – · – · node to node-thin.

2.3.5 Influence of element size in MPC connections

To study the influence of element size for MPC connections, the same numerical example in section 2.3.4 was used. The FE model with Heterosis elements and an MPC connection was modified to change the element size from the original 11×11 element mesh to meshes ranging from 6×6 to 22×22 elements and compared to the analytical solution.

Since the location of the nodes is changed for every different mesh, the force was applied and the response calculated using MPCs in order to predict the same transfer mobility as in section 2.3.4.

It was found that when a spring with a translational stiffness is used, the element size has a small influence when adapting MPC connections and only differences at higher frequencies are present, due to discretization errors as can be observed in Figure 2.14. There is a stiffening effect due to the increase in the constraint area as the element gets larger; however this effect is negligible since the variations in natural frequency and peak magnitude are insignificant as can be observed in Figure 2.15.

On the other hand, when a rotational stiffness is used the estimated transfer mobility is not as accurate as the translational stiffness case. Moreover, the estimated transfer mobility is sensitive to the element size; the magnitude changes with the element size as can be observed in Figure 2.16. If the plotted line below the first resonance is extended to lower frequencies, it is obvious that even the static solution for this problem is sensitive to the element size. This problem is not related to the MPC, since the MPC and node to node connection results are almost identical. Furthermore, the MPC results are closer to the analytical solution as can be seen in Figure 2.13. This sensitivity is generated when rotational stiffness is added into the FE stiffness matrix. This will be addressed and studied in detail on Chapter 4.

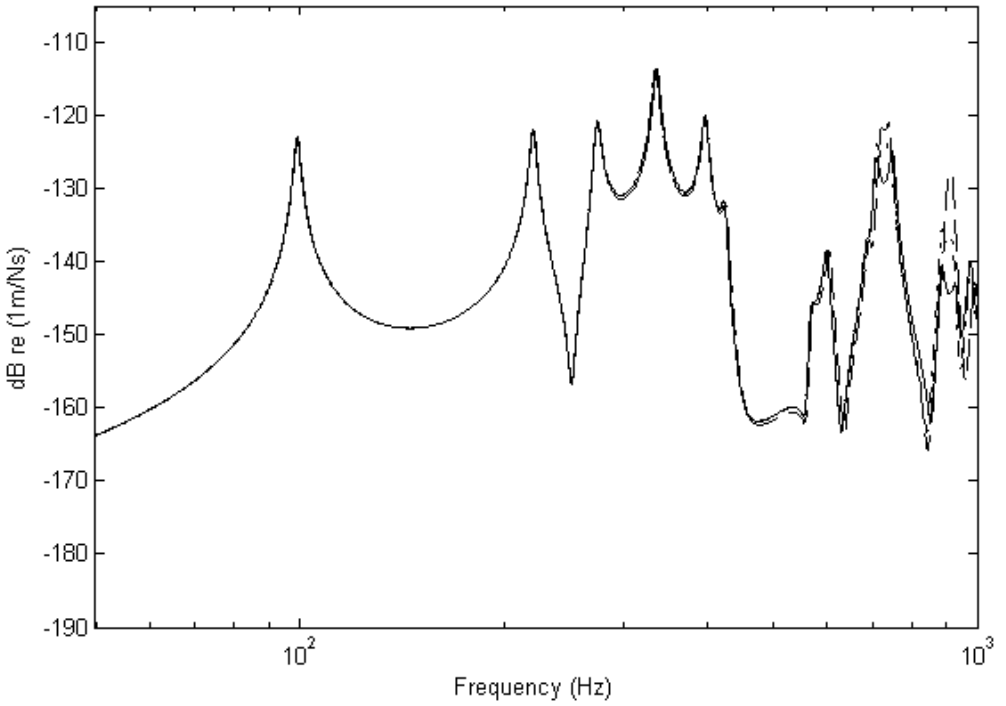

Figure 2.14: Magnitude of the transfer mobility magnitude for a system of two simply supported plates with a single elastic connection with translational stiffness:
—— analytical solution - - - - - MPC-heterosis 6×6 mesh; − − − MPC-heterosis 22×22 mesh.

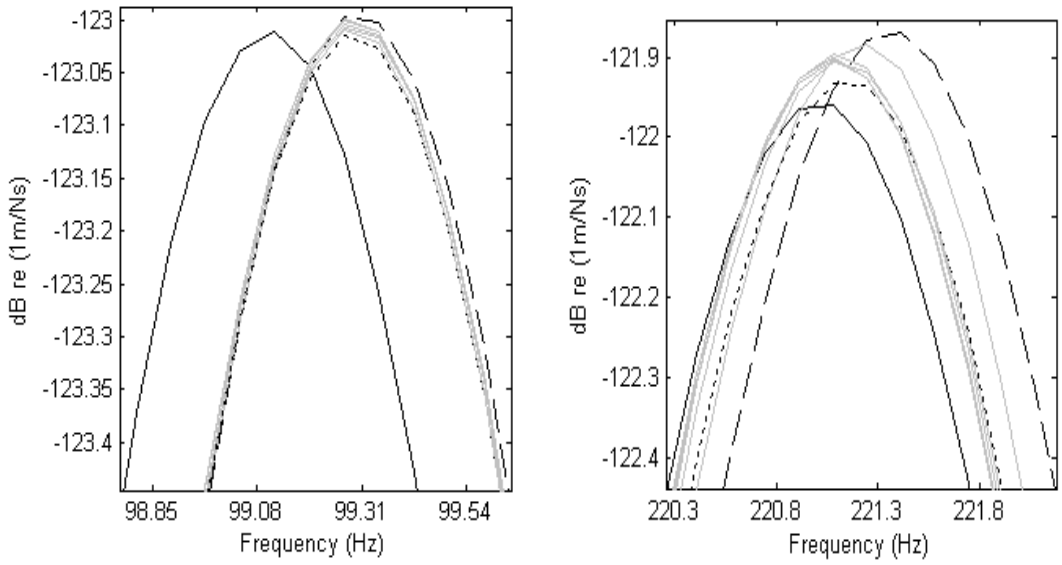

Figure 2.15: Magnitude of the transfer mobility magnitude for a system of two simply supported plates with a single elastic connection with translational stiffness: (a) first resonance; (b) second resonance: —— analytical solution ----- MPC-heterosis 6×6 mesh; – – – MPC-heterosis 22×22 mesh; —— MPC-heterosis meshes from 7×7 to 21×21.

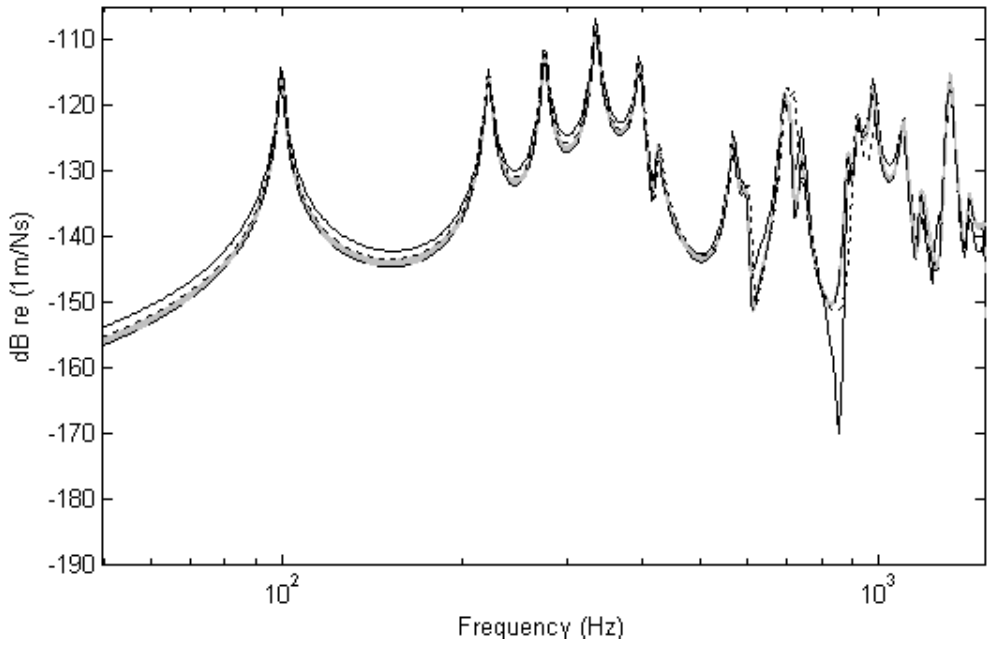

Figure 2.16: Magnitude of the transfer mobility for a system of two simply supported plates with a single elastic connection with rotational stiffness: (a) first resonance; (b) second resonance: —— analytical solution ----- MPC-heterosis 6×6 mesh; — — MPC-heterosis 22×22 mesh; —— MPC-heterosis meshes from 7×7 to 21×21.

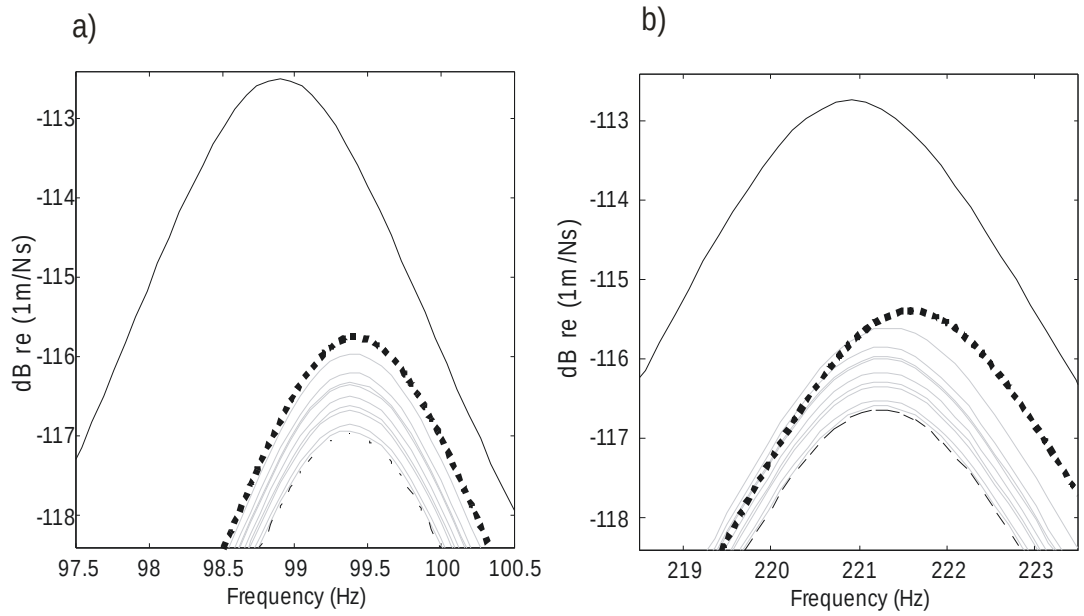

Figure 2.17: Magnitude of the transfer mobility for a system of two simply supported plates with a single elastic connection with rotational stiffness: (a) first resonance;(b) second resonance: —— analytical solution ----- MPC-heterosis 6×6 mesh; – – – MPC-heterosis 22×22 mesh; —— MPC-heterosis meshes from 7×7 to 21×21.

2.4 Conclusions

In this chapter multipoint constraints (MPC) were used to apply connections between flat structures. It was shown that an MPC connection can be placed between nodes of an FE model and is able to incorporate any change in the location of the elastic connection in an accurate way.

When beams are connected, results showed that the MPC connection has the same predictive performance compared to the direct node to node connections. Both models giving accurate results for point connections comprising a translational or rotational spring.

Results showed that the MPC connection is not accurate when thin plate elements are used, due to the non-conforming formulation. In contrast, when the Heterosis element was used the results showed that the MPC connection is as accurate as the node-to-node connection. Additional errors appear when rotational springs are used in the connection, due to discrepancies between the element formulation and the analytical

solution. Some convergence issues exist in the modal summation when rotational DOFs are involved; however the solution is still acceptable.

When a rotational spring is used, the transfer mobility magnitude is sensitive to the element size. This problem is not related to the MPC, since the MPC and node to node connection results are almost identical. Furthermore, the MPC results are closer to the analytical solution. This sensitivity is related to the addition of rotational stiffness into the FE stiffness matrix. This will be addressed and studied in detail on Chapter 4.

3 VIBRATION ANALYSIS OF STRUCTURES WITH UNCERTAIN SPOT WELD LOCATION

Spot-welded structures contain inherent variability in the location and/or stiffness of the spot weld due to the inherent variability of the manufacturing process. This variability leads to variability in the dynamic response of the structure. An analysis that includes uncertainty in properties of the joints provides a range of response predictions, adding more value to the design process compared to a single deterministic analysis.

In Chapter 2 it was seen that in modelling the structure, a model of the joints which is connected to the substructures by multipoint constraints (MPCs) has clear advantages. It can be located anywhere in the model and it is not necessary to re-mesh surfaces to assemble them giving accurate results whatever the location of the joint.

Therefore, MPC connections can improve the computational efficiency when Monte Carlo simulation (MCS) is used to analyze the dynamic behaviour of built-up structures with uncertainties in the location of the joints. In this case the MPC connections are used to model changes in the location of the joint instead of modifying the FE model from one sample to the next. Nonetheless, as the accuracy of this method depends on the number of repeated analyses used during the simulation [14], the computational effort is still high, especially for large scale models.

In order to further improve the efficiency, component mode synthesis (CMS) gives a sub-structuring framework by which the number of the degrees of freedom (DOFs) can be reduced [31]. Combining CMS with MPC joint models, the response of the system

can be evaluated for many joint locations using the same modal representation of the substructures.

However, if the number of DOFs involved in the connection between structures is large, the reduction in the model size using CMS is not great because the number of coupling DOFs is not reduced. Two techniques are proposed to overcome this problem: (i) characteristic constraint modes [22] and (ii) application of a low rank update theory [32] to the CMS matrices.

The use of characteristic constraint modes is a technique for reducing the size of a model generated by the Craig-Bampton method of CMS in which an eigenanalysis is applied to the constraint-mode partitions of the mass and stiffness matrices and the resulting modes are truncated to yield a reduced model.

When using the low rank update theory, the receptance matrix is first calculated for the unassembled system. Then the response of the assembled system is calculated by updating this response by including the effect of the connection. Here the efficiency is increased in two ways: (i) most of the CMS dynamic stiffness matrix is inverted only once during the MCS, (ii) the transformation from CMS coordinates to physical coordinates is also calculated only once during the MCS.

3.1 Component mode synthesis

CMS is a technique in which a structure is subdivided into components. The static and dynamic behaviour of each component is described in terms of a set of basis functions, e.g. the modes of the component. When the higher frequency modes are truncated a reduction in size is achieved. Another advantage arises in substructuring, where it may be cheaper to solve the eigenvalue problems of a number of the components and of the assembled reduced global system compared to solving the complete global eigenvalue problem [33].

The CMS method was introduced by Hurty [34] who introduced the concept of using component modes as trial functions or basis vectors. Craig and Bampton [21] simplified

the method when they showed that rigid body and redundant interface modes could be treated as constraint modes. There are different variants of the method [35–37] and reviews of current techniques in CMS are available in literature [38–40].

In this section the general CMS method is described followed by an overview of the most common types of component modes. Finally the fixed-interface Craig-Bampton [21] method is discussed in detail.

3.1.1 Background theory

The undamped equation of motion for a structure is given by

$$\mathbf{M}\ddot{\mathbf{u}} + \mathbf{K}\mathbf{u} = \mathbf{f} \tag{3.1}$$

where $\mathbf{u}$ are the physical DOFs, $\mathbf{M}$ and $\mathbf{K}$ are the mass and stiffness matrices respectively and $\mathbf{f}$ is the vector of external forces. The structure is divided into N substructures, where the mass and stiffness of the i th subsystem are given by $\mathbf{M}^{(i)}$ and $\mathbf{K}^{(i)}$. The global DOFs $\mathbf{u}$ are partitioned such that

$$\mathbf{u} = \left[\left(\mathbf{u}^{(1)}\right)^T \quad \left(\mathbf{u}^{(2)}\right)^T \quad \cdots \quad \left(\mathbf{u}^{(N)}\right)^T \right]^T \tag{3.2}$$

$\mathbf{u}^{(i)}$ can subsequently be partitioned into interior, $\mathbf{u}_I$ and coupling DOFs, $\mathbf{u}_c$ such that

$$\mathbf{u}^{(i)} = \begin{bmatrix} \mathbf{u}_I^{(i)} \\ \mathbf{u}_c^{(i)} \end{bmatrix} \tag{3.3}$$

The sub-matrices $\mathbf{M}$ and $\mathbf{K}$, that relate to each subsystem are given by

$$\mathbf{M}^{(i)} = \begin{bmatrix} \mathbf{m}_{II}^{(i)} & \mathbf{m}_{Ic}^{(i)} \\ \mathbf{m}_{cI}^{(i)} & \mathbf{m}_{cc}^{(i)} \end{bmatrix} \tag{3.4}$$

$$\mathbf{K}^{(i)} = \begin{bmatrix} \mathbf{K}_{II}^{(i)} & \mathbf{K}_{Ic}^{(i)} \\ \mathbf{K}_{cI}^{(i)} & \mathbf{K}_{cc}^{(i)} \end{bmatrix} \tag{3.5}$$

These form the block diagonal matrices of $\mathbf{M}$ and $\mathbf{K}$, i.e.

$$\mathbf{K} = blkdiag\left(\mathbf{K}^{(1)} \quad \mathbf{K}^{(2)} \quad \cdots \quad \mathbf{K}^{(N)}\right) \text{ and } \mathbf{M} = blkdiag\left(\mathbf{M}^{(1)} \quad \mathbf{M}^{(2)} \quad \cdots \quad \mathbf{M}^{(N)}\right) \tag{3.6}$$

The force vector associated with the i^{th} substructure is given by

$$\mathbf{F}^{(i)} = \begin{bmatrix} \mathbf{f}_I^{(i)} \\ \mathbf{f}_c^{(i)} \end{bmatrix} \tag{3.7}$$

and the equation of motion for each substructure is therefore

$$\mathbf{M}^{(i)}\ddot{\mathbf{u}}^{(i)} + \mathbf{K}^{(i)}\mathbf{u}^{(i)} = \mathbf{F}^{(i)} \tag{3.8}$$

Consider two coupled components, α and β that have a common boundary interface, the coupling DOFs can be constrained such that

$$\mathbf{u}_c^{(\alpha)} = \mathbf{u}_c^{(\beta)} \tag{3.9}$$

and the coupling forces are related by

$$\mathbf{f}_c^{(\alpha)} + \mathbf{f}_c^{(\beta)} = 0 \tag{3.10}$$

A selection of component modes is arranged in a component modal matrix $\mathbf{B}$. Usually these are one of two general types: kept fixed-interface modes and constraint modes; kept free-interface modes and attachment modes. The $\mathbf{u}$ DOFs can be transformed into the component modal coordinates $\mathbf{q}$ by

$$\mathbf{u} = \mathbf{B}\mathbf{q} \tag{3.11}$$

where

$$\mathbf{q} = \begin{bmatrix} \mathbf{q}^{(\alpha)} \\ \mathbf{q}^{(\beta)} \end{bmatrix} \tag{3.12}$$

It can be shown that the expressions for the kinetic and potential energy, from Lagrange's equation of motion for components α and β are given by [41]

$$T = \frac{1}{2}\dot{\mathbf{q}}^T\boldsymbol{\mu}\dot{\mathbf{q}} = \frac{1}{2}\dot{\mathbf{q}}^{(\alpha)T}\boldsymbol{\mu}^{(\alpha)}\dot{\mathbf{q}}^{(\alpha)} + \frac{1}{2}\dot{\mathbf{q}}^{(\beta)T}\boldsymbol{\mu}^{(\beta)}\dot{\mathbf{q}}^{(\beta)} \tag{3.13}$$

$$V = \frac{1}{2}\dot{\mathbf{q}}^T\boldsymbol{\kappa}\dot{\mathbf{q}} = \frac{1}{2}\dot{\mathbf{q}}^{(\alpha)T}\boldsymbol{\kappa}^{(\alpha)}\dot{\mathbf{q}}^{(\alpha)} + \frac{1}{2}\dot{\mathbf{q}}^{(\beta)T}\boldsymbol{\kappa}^{(\beta)}\dot{\mathbf{q}}^{(\beta)} \tag{3.14}$$

where

$$\boldsymbol{\mu}^{(\alpha)} = \mathbf{B}^{(\alpha)T}\mathbf{M}^{(\alpha)}\mathbf{B}^{(\alpha)} \tag{3.15}$$

$$\boldsymbol{\kappa}^{(\alpha)} = \mathbf{B}^{(\alpha)T}\mathbf{K}^{(\alpha)}\mathbf{B}^{(\alpha)} \tag{3.16}$$

are the transformed component mass and stiffness matrices (similarly for component β) which are assembled as

$$\boldsymbol{\mu} = \begin{bmatrix} \boldsymbol{\mu}^{(\alpha)} & 0 \\ 0 & \boldsymbol{\mu}^{(\beta)} \end{bmatrix} \text{ and } \boldsymbol{\kappa} = \begin{bmatrix} \boldsymbol{\kappa}^{(\alpha)} & 0 \\ 0 & \boldsymbol{\kappa}^{(\beta)} \end{bmatrix} \tag{3.17}$$

The conditions to be satisfied in equations (3.9) and (3.10) can be expressed in terms of the modal coordinates and written in matrix form as

$$\mathbf{Hq} = 0 \tag{3.18}$$

where **H** is the constraint matrix. This equation can be partitioned into linearly independent DOFs l and dependent DOFs d such that equation (3.18) becomes

$$\begin{bmatrix}\mathbf{H}_{dd} & \mathbf{H}_{dl}\end{bmatrix}\begin{bmatrix}\mathbf{q}_d \\ \mathbf{q}_l\end{bmatrix} = 0 \tag{3.19}$$

The Lagrangian for the system can be written as

$$L = T - V + \boldsymbol{\sigma}^T \mathbf{Hq} \tag{3.20}$$

where $\boldsymbol{\sigma}$ is a vector of Lagrange multipliers. It can be shown that the system equation of motion is given by [42]

$$\boldsymbol{\mu}\ddot{\mathbf{q}} + \boldsymbol{\kappa}\mathbf{q} = \mathbf{H}^T\boldsymbol{\sigma} \tag{3.21}$$

This can be solved by introducing a linear transformation

$$\mathbf{q} = \begin{bmatrix}\mathbf{q}_d \\ \mathbf{q}_l\end{bmatrix} = \mathbf{C}\mathbf{q}_l = \mathbf{C}\mathbf{v} \tag{3.22}$$

where **v** is the new set of independent modal coordinates and

$$\mathbf{C} = \begin{bmatrix}-\mathbf{H}_{dd}^{-1}\mathbf{H}_{dl} \\ \mathbf{I}_{ll}\end{bmatrix} \tag{3.23}$$

is the transformation matrix. The mass and stiffness matrices of the global system are then found by

$$\mathbf{M}_R^{gl} = \mathbf{C}^T \boldsymbol{\mu} \mathbf{C} \text{ and } \mathbf{K}_R^{gl} = \mathbf{C}^T \boldsymbol{\kappa} \mathbf{C} \tag{3.24}$$

which are reduced in size if the component modal matrix $\mathbf{B}$ is truncated.

Substituting equation (3.22) into (3.21), pre-multiplying by $\mathbf{C}^T$ and substituting $\mathbf{M}_R^{gl}$ and $\mathbf{K}_R^{gl}$ from equation (3.24), the equation of motion for the system becomes

$$\mathbf{M}_R^{gl} \ddot{\mathbf{v}} + \mathbf{K}_R^{gl} \dot{\mathbf{v}} = \mathbf{C}^T \mathbf{H}^T \boldsymbol{\sigma} \tag{3.25}$$

From equations (3.22) and (3.18) it can be seen that $\mathbf{HC} = 0$, therefore equation (3.25) becomes

$$\mathbf{M}_R^{gl} \ddot{\mathbf{v}} + \mathbf{K}_R^{gl} \dot{\mathbf{v}} = 0 \tag{3.26}$$

3.1.2 Component mode types

Component modes in equation (3.11) are defined as Ritz basis vectors, used for the reduced description of the static and/or dynamic behaviour of a substructure in a CMS setting. These may include normal modes of free vibration, rigid body modes, constraint modes, attachment modes and Krylov vectors [43].

The free-interface normal modes of a component are the eigenvectors of the component with the boundary DOFs free. They are found from solving the eigenvalue problem

$$\left(\mathbf{K} - \lambda_j^{fr} \mathbf{M}\right) \boldsymbol{\phi}_j^{fr} = 0 \tag{3.27}$$

and can be combined as columns to give the normal mode matrix $\boldsymbol{\Phi}^{fr}$. The normal modes may be divided into a set of modes k to be kept for further calculations and a complementary set of modes d that will be deleted, i.e.

$$\boldsymbol{\Phi}^{fr} = \begin{bmatrix} \boldsymbol{\Phi}_k^{fr} & \boldsymbol{\Phi}_d^{fr} \end{bmatrix} \tag{3.28}$$

Similarly, the eigenvalues λ are arranged on the diagonal of the eigenvalue matrix $\boldsymbol{\Lambda}$ and can be divided into sets k and d to give

$$\boldsymbol{\Lambda}^{fr} = \begin{bmatrix} \boldsymbol{\Lambda}_k^{fr} & 0 \\ 0 & \boldsymbol{\Lambda}_d^{fr} \end{bmatrix} \tag{3.29}$$

If a component is unconstrained, the normal mode set contains rigid body modes with zero-valued eigenvalues.

The fixed-interface normal modes of a component are the eigenvectors of the component with the interface DOFs fixed. The size of the eigenvalue problem is therefore reduced by the number of interface DOFs. It is governed by the elements of the mass and stiffness matrices associated with the interior DOFs only and given as

$$\left(\mathbf{K}_{II} - \lambda_j^{fi}\mathbf{M}_{II}\right)\phi_{Ij}^{fi} = 0 \tag{3.30}$$

where λ_j^{fi} are the fixed-interface eigenvalues. The eigenvectors ϕ_{Ij}^{fi} form the columns of the normal mode matrix $\boldsymbol{\Phi}^{fi}$, which can be divided into a matrix with kept (k) and deleted (d) modes, respectively. The normal mode matrix is then

$$\boldsymbol{\Phi}^{fi} = \begin{bmatrix} \boldsymbol{\Phi}_k^{fi} & \boldsymbol{\Phi}_d^{fi} \end{bmatrix} = \begin{bmatrix} \boldsymbol{\Phi}_{Ik}^{fi} & \boldsymbol{\Phi}_{Id}^{fi} \\ \mathbf{0}_{ck} & \mathbf{0}_{cd} \end{bmatrix} \tag{3.31}$$

where the $\mathbf{0}_c$ relate to the DOFs of the fixed coupling DOFs. There are no rigid body modes in Equation (3.31) if the set of fixed boundary DOFs is sufficient to constrain all rigid body modes of the unconstrained component.

Static constraint modes will be defined with respect to the interface DOFs and denoted by the subscript c. A constraint mode is the static displacement of all nodes due to a unit displacement applied to one interface coordinate and with all other interface coordinates fixed. This can be written in matrix form as

$$\begin{bmatrix} \mathbf{K}_{II} & \mathbf{K}_{Ic} \\ \mathbf{K}_{cI} & \mathbf{K}_{cc} \end{bmatrix} \begin{bmatrix} \mathbf{\Psi}_{Ic} \\ \mathbf{I}_{cc} \end{bmatrix} = \begin{bmatrix} \mathbf{0}_{Ic} \\ \mathbf{F}_{cc} \end{bmatrix} \tag{3.32}$$

where $\mathbf{\Psi}_{Ic}$ is a matrix of displacements of the interior DOFs and $\mathbf{I}_{cc}$ is an identity matrix, which defines zero and unit displacements for all constraint modes. $\mathbf{F}_{cc}$ are the force reactions at the nodes with prescribed displacements and the interior nodes are force-free. From the first line of Equation (3.32) it follows that

$$\mathbf{\Psi}_{Ic} = -\mathbf{K}_{II}^{-1}\mathbf{K}_{Ic} \tag{3.33}$$

and the complete matrix of constraint modes is given by

$$\mathbf{\Psi}_{c} = \begin{bmatrix} -\mathbf{K}_{II}^{-1}\mathbf{K}_{Ic} \\ \mathbf{I}_{cc} \end{bmatrix} \tag{3.34}$$

Rigid body modes appear if a component is unconstrained. They are obtained either as free-interface normal modes (Equation (3.28)) from the eigenvalue problem or recovered from constraint modes (Equation (3.34)). However they are often regarded as a separate class of component modes and will be denoted by $\mathbf{\Psi}_{r}$.

Static attachment modes will be defined with respect to the boundary DOFs and will be denoted by the subscript a. An attachment mode is the static displacement of all nodes due to a unit force applied to one boundary coordinate and with all other boundary coordinates force-free. Since forces are applied, the cases of a constrained and an unconstrained component have to be distinguished. If the component is constrained the governing static equation is given by

$$\begin{bmatrix} \boldsymbol{\psi}_{Ia} \\ \boldsymbol{\psi}_{aa} \end{bmatrix} = \begin{bmatrix} \mathbf{K}_{II} & \mathbf{K}_{Ia} \\ \mathbf{K}_{aI} & \mathbf{K}_{aa} \end{bmatrix}^{-1} \begin{bmatrix} \mathbf{0}_{Ia} \\ \mathbf{I}_{aa} \end{bmatrix} \tag{3.35}$$

where $\boldsymbol{\Psi}_{Ia}$ and $\boldsymbol{\Psi}_{aa}$ are the unknown nodal displacements. The identity matrix $\mathbf{I}_{aa}$ arises from the forces at the boundary DOFs. All interior DOFs are force-free. A solution can be found by inverting the stiffness matrix $\mathbf{K}$, where $\mathbf{G} = \mathbf{K}^{-1}$ is the flexibility matrix, assuming the inverse exists, to give

$$\begin{bmatrix} \boldsymbol{\Psi}_{Ia} \\ \boldsymbol{\Psi}_{aa} \end{bmatrix} = \begin{bmatrix} \mathbf{G}_{II} & \mathbf{G}_{Ia} \\ \mathbf{G}_{aI} & \mathbf{G}_{aa} \end{bmatrix} \begin{bmatrix} \mathbf{0}_{Ia} \\ \mathbf{I}_{aa} \end{bmatrix} \tag{3.36}$$

The attachment modes are then found to be

$$\boldsymbol{\Psi}_{a} = \begin{bmatrix} \mathbf{G}_{Ia} \\ \mathbf{G}_{aa} \end{bmatrix} \tag{3.37}$$

Residual attachment modes may be defined for forces applied at one of the coupling DOFs at a time with all other DOFs force-free. The force is given in equation (3.35) as

$$F_{a} = \begin{bmatrix} \mathbf{0}_{Ia} \\ \mathbf{I}_{aa} \end{bmatrix} \tag{3.38}$$

A set of residual attachment modes is then defined by

$$\boldsymbol{\Psi}_{aR} = \mathbf{G}_{d}\mathbf{F}_{a} \tag{3.39}$$

where $\mathbf{G}_{d}$ is the residual flexibility matrix associated with the deleted modes and related to the free-interface normal mode matrix $\boldsymbol{\Phi}$ and the free-interface eigenvalues $\boldsymbol{\Lambda}$

$$\mathbf{G}_d = \mathbf{\Phi}_d \mathbf{\Lambda}_d^{-1} \mathbf{\Phi}_d^T \tag{3.40}$$

The two most commonly used CMS methods are firstly the free-interface Craig-Chang method [44] in which residual attachment modes are added to the free-interface modes to form the modal matrix $\mathbf{B}$. The second method is the fixed interface Craig-Bampton method [21] in which the fixed normal modes $\mathbf{\Phi}^{fi}$ of a component are found with the boundaries fixed. In order to improve convergence, assure the compatibility of the components and yield the exact static solution static constraint modes $\mathbf{\Psi}_c$ are added to the component modal matrix $\mathbf{B}$.

The free interface method is sometimes preferred since the free interface modes can be measured more easily than the constraint modes. However, for this application the Craig-Bampton method offers a number of advantages since the coupling DOFs are isolated in the reduced matrices as is shown in the following subsection.

3.1.3 Craig-Bampton Method

In the fixed interface method of CMS, the component modal matrix of a component α is

$$\mathbf{B}^{\alpha} = \begin{bmatrix} \mathbf{\Phi}_k{}^{\alpha} & \mathbf{\Psi}_c{}^{\alpha} \end{bmatrix} \tag{3.41}$$

and the transformation matrix from physical coordinates to component modal coordinates is given by

$$\mathbf{u}^{\alpha} = \mathbf{B}^{\alpha} \mathbf{q}^{\alpha} = \begin{bmatrix} \mathbf{u}_I^{\alpha} \\ \mathbf{u}_c^{\alpha} \end{bmatrix} = \begin{bmatrix} \mathbf{\Phi}_{Ik}^{fi} & -\mathbf{K}_{II}^{-1}\mathbf{K}_{Ic} \\ \mathbf{0} & \mathbf{I}_{cc} \end{bmatrix} \begin{bmatrix} \mathbf{q}_k^{\alpha} \\ \mathbf{q}_c^{\alpha} \end{bmatrix} \tag{3.42}$$

Here the physical coupling DOFs $\mathbf{u}_c$ are retained, but will be denoted as modal DOFs $\mathbf{q}_c$ (i.e. $\mathbf{u}_c = \mathbf{q}_c$). On the other hand the interior physical DOFs $\mathbf{u}_I$ are transformed into modal DOFs $\mathbf{q}_k$. The mass matrix in modal DOFs

$$\boldsymbol{\mu}^{\alpha} = \begin{bmatrix} \mathbf{I}_{kk} & \mathbf{m}_{kc} \\ \mathbf{m}_{kc}^{T} & \mathbf{m}_{cc} \end{bmatrix}^{\alpha} \tag{3.43}$$

where $\mathbf{I}_{kk}$ is a identity matrix if the normal modes are mass normalised. The $\mathbf{m}_{cc}$ contains the modal constraint masses and $\mathbf{m}_{kc}$ are the coupling matrices between the modal $\mathbf{q}_k$ and $\mathbf{q}_c$. The stiffness matrix in component modal DOFs is given by

$$\boldsymbol{\kappa}^{\alpha} = \begin{bmatrix} \boldsymbol{\Lambda}_{kk} & \mathbf{0} \\ \mathbf{0} & \mathbf{k}_{cc} \end{bmatrix} \tag{3.44}$$

where $\boldsymbol{\Lambda}_{kk}$ is a diagonal matrix of eigenvalues and $\mathbf{k}_{cc}$ is the constraint modal stiffness matrix.

The system matrix in modal DOFs is assembled for a system comprising two components, α and β,

$$\mathbf{q} = \begin{bmatrix} \mathbf{q}_k^{\alpha T} & \mathbf{q}_c^{\alpha T} & \mathbf{q}_k^{\beta T} & \mathbf{q}_c^{\beta T} \end{bmatrix}^{T} \tag{3.45}$$

In order to transform $\mathbf{q}$ DOFs into linearly independent modal DOFs $\mathbf{v}$, the coupling conditions are imposed using equation (3.22), where the transformation matrix $\mathbf{C}$ depends on the conditions at the interface, for example, in the case of rigid connections

$$\mathbf{u}_c^{\alpha} = \mathbf{u}_c^{\beta} \tag{3.46}$$

Which can be transformed into modal space by equation (3.42)

$$\mathbf{q}_c^{\alpha} = \mathbf{q}_c^{\beta} = \mathbf{q}_c \tag{3.47}$$

In which case, the matrix constraint equation

$$\mathbf{Hq} = \begin{bmatrix} \mathbf{0} & \mathbf{I} & \mathbf{0} & \mathbf{-I} \end{bmatrix} \begin{bmatrix} \mathbf{q}_k^{\alpha^T} & \mathbf{q}_c^{\alpha^T} & \mathbf{q}_k^{\beta^T} & \mathbf{q}_c^{\beta^T} \end{bmatrix}^T = 0 \tag{3.48}$$

and

$$\mathbf{C} = \begin{bmatrix} \mathbf{I} & \mathbf{0} & \mathbf{0} \\ \mathbf{0} & \mathbf{0} & \mathbf{I} \\ \mathbf{0} & \mathbf{I} & \mathbf{0} \\ \mathbf{0} & \mathbf{0} & \mathbf{I} \end{bmatrix} \tag{3.49}$$

The reduced global system matrices are found by equation (3.24), so that

$$\mathbf{M}_R^{gl} = \begin{bmatrix} \mathbf{I}_{kk}^{\alpha} & \mathbf{0} & \mathbf{m}_{kc}^{\alpha} \\ \mathbf{0} & \mathbf{I}_{kk}^{\beta} & \mathbf{m}_{kc}^{\beta} \\ \mathbf{m}_{kc}^{\alpha\,T} & \mathbf{m}_{kc}^{\beta\,T} & \mathbf{m}_{cc}^{\alpha} + \mathbf{m}_{cc}^{\beta} \end{bmatrix} \tag{3.50}$$

and

$$\mathbf{K}_R^{gl} = \begin{bmatrix} \mathbf{\Lambda}_{kk}^{\alpha} & \mathbf{0} & \mathbf{0} \\ \mathbf{0} & \mathbf{\Lambda}_{kk}^{\beta} & \mathbf{0} \\ \mathbf{0} & \mathbf{0} & \mathbf{k}_{cc}^{\alpha} + \mathbf{k}_{cc}^{\beta} \end{bmatrix} \tag{3.51}$$

3.1.4 Characteristic constraint modes

The size of the constraint matrices in equations (3.50) and (3.51) depends on the number of kept fixed interface modes and interface DOFs. Since there is no reduction of the interface DOFs, the computational cost of equation (3.72) can be dominated by these modes, especially for applications involving line and surface coupling of components where the number of interface DOFs can be considerable compared to the overall number of DOFs. The number of interface DOFs can be reduced by introducing characteristic constraint modes [22].

The characteristic constraint modes are the solution of the right-eigenvalue problem

$$\left(\mathbf{K}_{cc} - \lambda_{cc}\mathbf{M}_{cc}\right)\phi_{cc} = 0 \tag{3.52}$$

where, the matrix of characteristic constraint modes

$$\phi_{cc} = \begin{bmatrix} \phi_1 & \phi_2 & \cdots & \phi_c \end{bmatrix} \tag{3.53}$$

defines a projection of the constraint component modal coordinates $\mathbf{q}_c^{(1)}$ and $\mathbf{q}_c^{(2)}$ (in equation (3.59) on to a new set of interface basis coordinates $\mathbf{g}$, i.e.

$$\begin{bmatrix} \mathbf{q}_c^{(1)} \\ \mathbf{q}_c^{(2)} \end{bmatrix} = \phi_{cc}\mathbf{g} \tag{3.54}$$

A reduction in the number of coordinates is obtained if only k characteristic modes are kept so that

$$\phi_{kcc} = \begin{bmatrix} \phi_1 & \phi_2 & \cdots & \phi_k \end{bmatrix} \tag{3.55}$$

consequently, the system matrices in coordinates $\mathbf{g}$ are

$$\mathbf{M}_g = \begin{bmatrix} \mathbf{I}_{kk} & \mathbf{m}_{kc}\phi_{kcc} \\ \phi_{kcc}^T\mathbf{m}_{kc}^T & \phi_{kcc}^T\mathbf{M}_{cc}\phi_{kcc} \end{bmatrix} \text{ and } \mathbf{K}_g = \begin{bmatrix} \Lambda_{kk} & 0 \\ 0 & \phi_{kcc}^T\mathbf{K}_{cc}\phi_{kcc} \end{bmatrix} \tag{3.56}$$

3.2 Craig-Bampton method applied to MPC connections

In order to apply the Craig-Bampton method to use CMS with sub-structures assembled with an MPC connection, first the system is divided into components. For the example in Figure 2.2, the system is divided into two components: (1) the upper plate and (2) the lower plate.

For each component i, $i=1,2$, the DOFs are separated into interior and coupling DOFs, $\mathbf{u}_c$ and $\mathbf{u}_I$ respectively. Here, $\mathbf{u}_c$ are all the DOFs within the area in which the location of each of the n point connections varies. The group of elements in which each connection might lie is called a patch. i.e. $\mathbf{u}_c$ contains every DOF in each of the n patches. For example, Figure 3.1 shows the coupling DOFs for a system with three connections with each patch comprising an array of 4x4 elements, i.e. the location of each connection might lie anywhere within sixteen elements. The normal modes for each component i are calculated using equations (3.31) and (3.33) are assembled in the component mode matrix $\mathbf{B}^i$ in equation (3.41). It is important to remember that only some of the normal modes are kept in $\mathbf{\Phi}_k{}^i$ achieving reduction in the size of the system matrices.

The component physical co-ordinates $\mathbf{u}$ can be transformed into the component modal co-ordinates $\mathbf{q}$ using equations (3.42). The component modal mass and stiffness matrices for each component i are given by

$$\boldsymbol{\mu}^i = \mathbf{B}^{iT}\mathbf{M}^i\mathbf{B}^i \tag{3.57}$$

$$\boldsymbol{\kappa}^i = \mathbf{B}^{iT}\mathbf{K}^i\mathbf{B}^i \tag{3.58}$$

where $\mathbf{M}^i$ and $\mathbf{K}^i$ are the mass and stiffness matrices of component i in component physical co-ordinates $\mathbf{u}$, $\boldsymbol{\mu}^{(i)}$ and $\boldsymbol{\kappa}^{(i)}$ are the mass and stiffness matrices of component i in component modal coordinates.

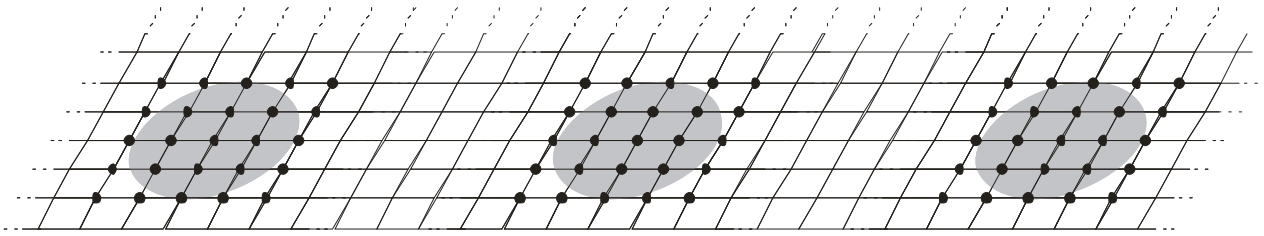

Figure 3.1: Part of FE mesh of a plate with three point connections allowed to lie within the highlighted areas. ▒ Possible joint location, ● constrained nodes.

For this system the modal DOFs matrix is assembled as

$$\mathbf{q} = \begin{bmatrix} \mathbf{q}_k^{(1)} \\ \mathbf{q}_c^{(1)} \\ \mathbf{q}_k^{(2)} \\ \mathbf{q}_c^{(2)} \end{bmatrix} \tag{3.59}$$

where $\mathbf{q}_k^{(i)}$ are the component modal coordinates and $\mathbf{q}_c^{(i)}$ are the constraint co-ordinates for the *i*th component. In this case, a rigid connection between the boundary DOFs is not applied, instead the boundary DOFs are connected using the stiffness matrix from the MPC connection $\mathbf{K}_{MPC}$ defined in equation (2.11) in Chapter 2. In order to do so, the component modal DOFs $\mathbf{q}$ are transformed into linearly independent component modal DOFs $\mathbf{v}$ using a transformation matrix $\mathbf{S}$

$$\mathbf{q} = \mathbf{S}\mathbf{v} \tag{3.60}$$

where

$$\mathbf{s} = \begin{bmatrix} \mathbf{I} & 0 & 0 & 0 \\ 0 & 0 & \mathbf{I} & 0 \\ 0 & \mathbf{I} & 0 & 0 \\ 0 & 0 & 0 & \mathbf{I} \end{bmatrix} \tag{3.61}$$

and

$$\mathbf{v} = \begin{bmatrix} \mathbf{q}_k^{(1)} \\ \mathbf{q}_k^{(2)} \\ \mathbf{q}_c^{(1)} \\ \mathbf{q}_c^{(2)} \end{bmatrix} \tag{3.62}$$

The global mass and stiffness matrices in the global co-ordinates $\mathbf{v}$ are given by,

$$\mathbf{M}_R = \mathbf{S}^T \begin{bmatrix} \boldsymbol{\mu}^{(1)} & 0 \\ 0 & \boldsymbol{\mu}^{(2)} \end{bmatrix} \mathbf{S} \text{ and } \mathbf{K}_R = \mathbf{S}^T \begin{bmatrix} \boldsymbol{\kappa}^{(1)} & 0 \\ 0 & \boldsymbol{\kappa}^{(2)} \end{bmatrix} \mathbf{S} \tag{3.63}$$

resulting in

$$\mathbf{M}_R = \begin{bmatrix} \mathbf{I}_{kk}^{(1)} & 0 & \mathbf{m}_{kc}^{(1)} & 0 \\ 0 & \mathbf{I}_{kk}^{(2)} & 0 & \mathbf{m}_{kc}^{(2)} \\ \mathbf{m}_{kc}^{(1)T} & 0 & \mathbf{m}_{cc}^{(1)} & 0 \\ 0 & \mathbf{m}_{kc}^{(2)T} & 0 & \mathbf{m}_{cc}^{(2)} \end{bmatrix} \text{ and } \mathbf{K}_R = \begin{bmatrix} \boldsymbol{\Lambda}_{kk}^{(1)} & 0 & 0 & 0 \\ 0 & \boldsymbol{\Lambda}_{kk}^{(2)} & 0 & 0 \\ 0 & 0 & \mathbf{k}_{cc}^{(1)} & 0 \\ 0 & 0 & 0 & \mathbf{k}_{cc}^{(2)} \end{bmatrix} \tag{3.64}$$

where $\boldsymbol{\Lambda}_{kk}^{(1)}$ and $\boldsymbol{\Lambda}_{kk}^{(2)}$ are diagonal matrices of eigenvalues of component 1 and component 2 respectively, $\mathbf{I}$ is the identity matrix of appropriate size and

$$\mathbf{M}_{cc} = \begin{bmatrix} \mathbf{m}_{cc}^{(1)} & 0 \\ 0 & \mathbf{m}_{cc}^{(2)} \end{bmatrix} \text{ and } \mathbf{K}_{cc} = \begin{bmatrix} \mathbf{k}_{cc}^{(1)} & 0 \\ 0 & \mathbf{k}_{cc}^{(2)} \end{bmatrix} \tag{3.65}$$

are the mass and stiffness matrices for the interface DOFs $\mathbf{u}_{cc}$. $\mathbf{K}_{MPC}$ can be added to the system stiffness matrices using equations (2.13), (3.63) and (3.64) as

$$\mathbf{K}_R = \begin{bmatrix} \boldsymbol{\Lambda}_{kk}^{(1)} & 0 & 0 & 0 \\ 0 & \boldsymbol{\Lambda}_{kk}^{(2)} & 0 & 0 \\ 0 & 0 & \mathbf{k}_{cc}^{(1)} + \mathbf{K}_{MPC}^{(11)} & \mathbf{K}_{MPC}^{(12)} \\ 0 & 0 & \mathbf{K}_{MPC}^{(21)} & \mathbf{k}_{cc}^{(2)} + \mathbf{K}_{MPC}^{(22)} \end{bmatrix} \tag{3.66}$$

It can be observed that if the location of the point connection changes within the element, only the terms in the matrix $\mathbf{K}_{MPC}$ change. This means in order to obtain the reduced mass and stiffness matrices $\mathbf{M}_R$ and $\mathbf{K}_R$ for different connection locations, only the matrix $\boldsymbol{\Gamma}$ in equation (2.7) needs to be re-calculated and equation (2.11) re-evaluated, offering a reduction in computation time.

3.2.1 Frequency response function

The equation of motion for forced undamped vibrations in modal co-ordinates **v** is given by

$$\mathbf{M}_R\ddot{\mathbf{v}} + \mathbf{K}_R\mathbf{v} = \mathbf{f}_\mathbf{v} \tag{3.67}$$

If harmonic motion is assumed, $\mathbf{v} = \mathbf{V}e^{i\omega t}$ and $\mathbf{f}_\mathbf{v} = \mathbf{F}_\mathbf{v}e^{i\omega t}$ then

$$\mathbf{V} = [\mathbf{K}_R - \omega^2\mathbf{M}_R]^{-1}\mathbf{F}_\mathbf{v} \tag{3.68}$$

The transformation from linearly independent global modal co-ordinates **v** to the physical component co-ordinates **u** is given in equations (3.11) and (3.60) as

$$\mathbf{u} = \mathbf{BSv} \tag{3.69}$$

One can express the modal forces $\mathbf{F}_\mathbf{v}$ in terms of the applied nodal forces $\mathbf{F}_\mathbf{u}$ as

$$\mathbf{F}_\mathbf{v} = \mathbf{S}^T\mathbf{B}^T\mathbf{F}_\mathbf{u} \tag{3.70}$$

Then, the receptance matrix **A** in physical coordinates is given by

$$\mathbf{A} = \mathbf{BS}\left[\mathbf{K}_R - \omega^2\mathbf{M}_R\right]^{-1}\mathbf{S}^T\mathbf{B}^T \tag{3.71}$$

Finally, the response at nodal DOF r with an excitation of unit amplitude at DOF e is given by the element $\mathbf{A}(r,e)$ in the matrix **A**. Introducing damping with a loss factor η to the global component modal stiffness matrix $\mathbf{K}_R$, this response can be evaluated using the matrix product

$$\mathbf{A}(r,e) = \mathbf{B}^{r*}\mathbf{S}\left[\mathbf{K}_R(1+i\eta) - \omega^2\mathbf{M}_R\right]^{-1}\mathbf{S}^T\mathbf{B}^{e*T} \tag{3.72}$$

where $\mathbf{B}^{r*}$ and $\mathbf{B}^{e*}$ are the r^{th} and e^{th} row of $\mathbf{B}$ respectively. The method outlined here is validated in the following section.

3.2.2 Numerical validation

The numerical example is the same system that was used in section 2.3.4. Using MPCs, the elastic point spring connection is located at the midpoint of the region that surrounds the area in which the position varies, represented as the shaded elements in Figure 2.9.

Using this position, the transfer mobility from coordinate (0.38, 0.32) in plate 1 to coordinate (0.38, 0.32) in plate 2 as shown in Figure 2.9 was evaluated. When the Craig-Bampton method is applied, all the DOFs in the shaded elements are set as boundary DOFs. When the component mode matrix $\mathbf{B}^i$ is assembled using equation (3.41) fewer modes can be kept in order to further reduce the DOFs of the system and reduce computational time. When more modes are truncated, the frequency range over which the solution is accurate is reduced, i.e. the accuracy at higher frequencies is lost but the accuracy at lower frequencies is maintained. Therefore, depending on the frequency range of interest the computational efficiency can be further improved.

When the Craig-Bampton method is applied in this example, it was found that only the first 25 modes of component 1 and the first 7 modes of component 2 are necessary for errors of 0.5% or less at all frequencies below 1000 Hz when compared to the full FE solution. Fewer modes of component 2 are required, because it is stiffer with fewer modes in the bandwidth considered. When CMS is applied, the computational time is reduced by nearly 90%. The comparison between CMS results and results for no component reduction are shown in Figure 3.2(a) and Figure 3.2(b).

The FRFs calculated by retaining fewer modes in the CMS solution are shown in Figure 3.3. It can be observed how the frequency range in which the CMS solution is accurate is reduced as the number of kept modes is reduced. For example, if the frequency range of interest were up to 100 Hz, keeping only 3 modes of the upper plate and 1 of the lower plate is sufficient to give accurate results.

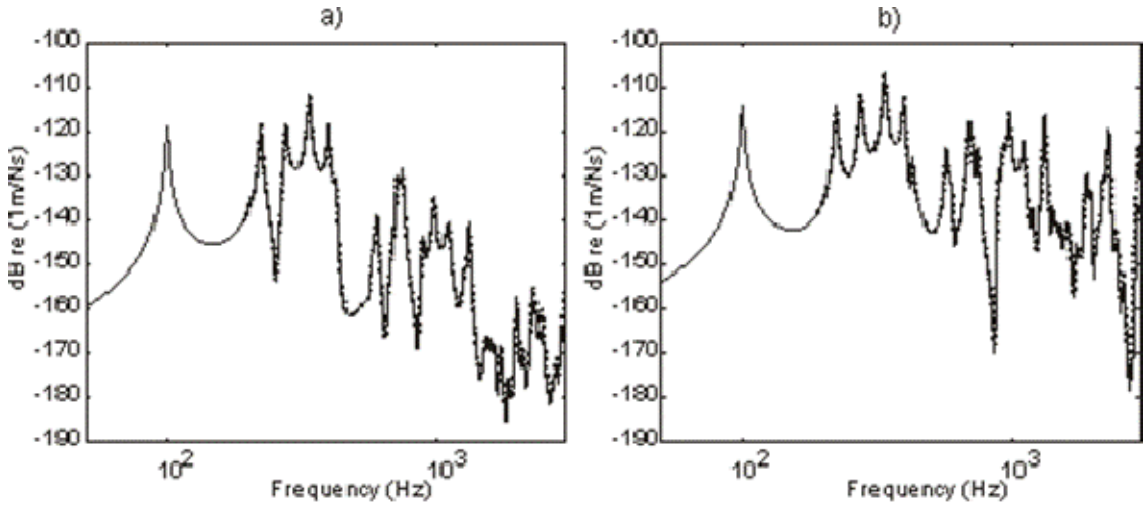

Figure 3.2: Transfer mobility: (a) translational stiffness connection and (b) rotational stiffness connection: ——— full solution+node to node; ------ CMS+MPC.

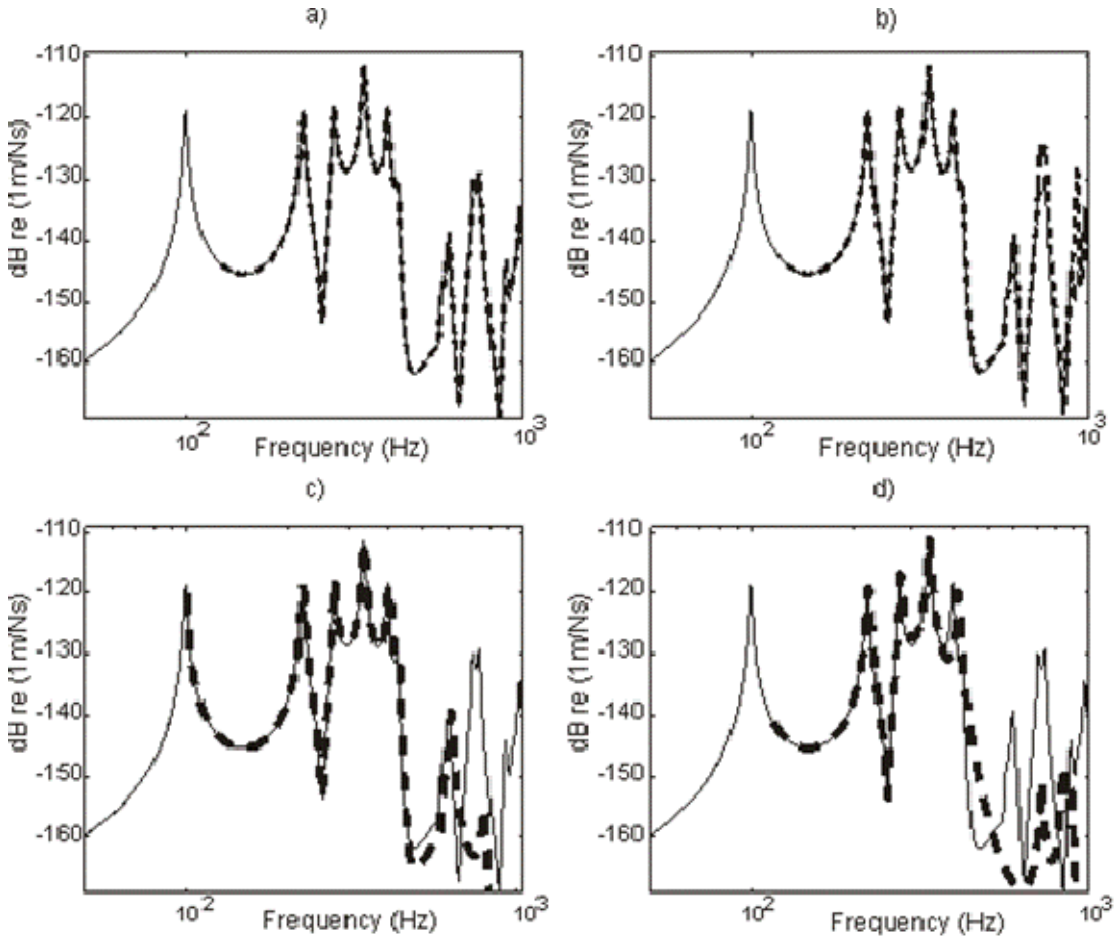

Figure 3.3: Transfer mobility at baseline position with a translational stiffness connection: ——— full solution; — — CMS: (a) 25 + 7 kept modes; (b) 12 + 3 kept modes; (c) 6 + 2 kept modes; (d) 3+1 kept modes.

In order to validate the model for different coupling conditions, the CMS+MPC model is compared to the full solution of the node to node connection model using different values of the point translation stiffness: (a) $K_w \ll D_{(\infty)}^{1+2}$, (b) $K_w \approx D_{(\infty)}^{1+2}$ and (c) $K_w \gg D_{(\infty)}^{1+2}$, where $D_{(\infty)}^{1+2}$ is the sum of the point dynamic stiffness of infinite plates with the material properties and thickness of each connected plate, i.e.

$$D_{(\infty)}(\omega) = i\omega 8\sqrt{\rho h B'} \tag{3.73}$$

is the dynamic stiffness of an infinite plate, where ρ is the density, h is the thickness and B' is the bending stiffness of plate given by

$$B' = \frac{Eh^3}{12\left(1-\upsilon^2\right)} \tag{3.74}$$

where E is the Young's modulus and υ is the Poisson ratio.

For the previous numerical example, when the static stiffness of the connection $K_w = 16000\,\text{N/m}$ is compared to the sum of the magnitudes of the dynamic stiffnesses of the connected plates at 1000 Hz, $D_{(\infty)}^{1+2} = 2.72\times10^7$ N/m, it can be observed that $K_w \ll D_{(\infty)}^{1+2}$.

For different connection stiffness values, the CMS+MPC model is in good agreement with the node to node connection and full solution as can be observed in Figure 3.4. It can be seen that when $K_w = 10^8$ the connection is effectively rigid.

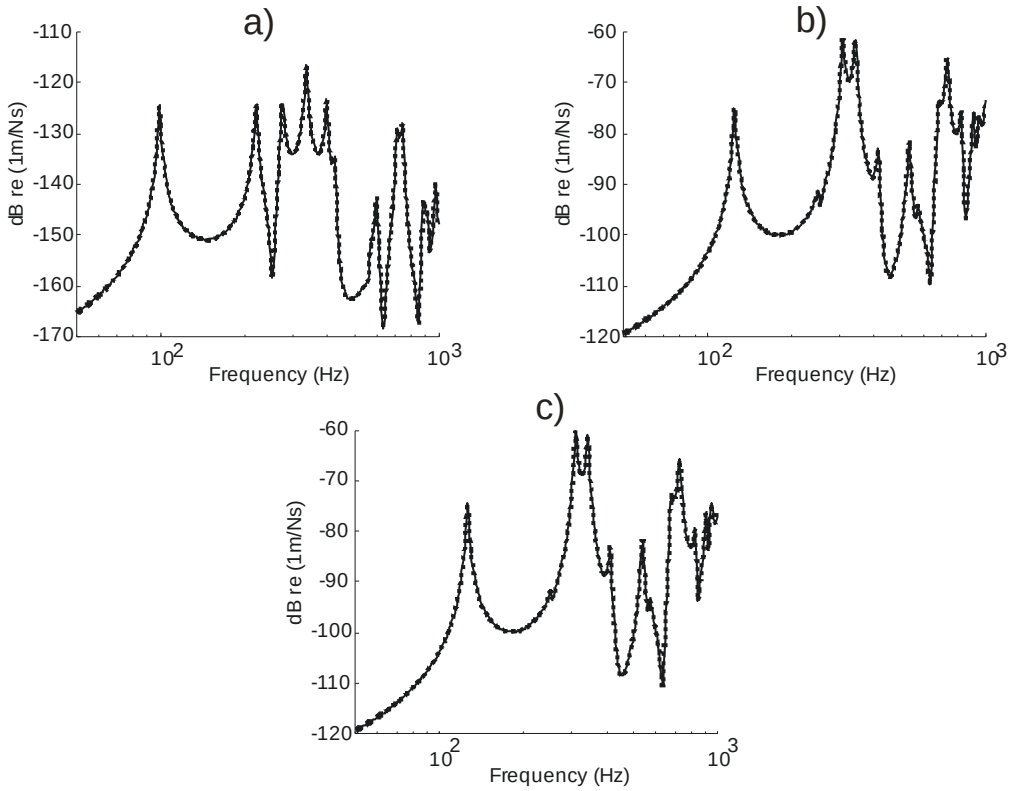

Figure 3.4: Transfer mobility at baseline position with a translational stiffness connection: ——— full solution, node to node; **-----** CMS+MPC with 24 and 7 kept modes for plates 1 and 2 respectively: (a) $K_W = 10^4$ N/m; (b) $K_W = 10^8$ N/m (c) $K_W = 10^{12}$ N/m;

3.3 Characteristic constraint modes applied to MPC connections

When analyzing a structure with uncertain MPC connections using the Craig-Bampton method outlined in section 3.2 it can be seen the computational cost of equation (3.71) and (3.72) is associated with the number of coupling DOFs. When this is applied to a built up structure, the number of coupling DOFs increases if the number of connections increases or the size of the elements in the FE model is reduced. In order to reduce the number of DOFs and reduce computational cost, characteristic constraint modes are applied to the CMS matrices in which the MPC stiffness is included (see equation (3.66)). In that case, equation (3.52) becomes

$$\left(\mathbf{K}_{cc}^{\Delta\mathbf{K}} - \lambda_{cc}\mathbf{M}_{cc}\right)\mathbf{\Phi}_{cc}^{\Delta\mathbf{K}} = 0 \tag{3.75}$$

The constraint component modal coordinates $\mathbf{q}_c^{(1)}$ and $\mathbf{q}_c^{(2)}$ are then transformed on to a new set of interface basis coordinates $\mathbf{g}$, i.e.

$$\begin{bmatrix} \mathbf{q}_c^{(1)} \\ \mathbf{q}_c^{(2)} \end{bmatrix} = \boldsymbol{\Phi}_{cc}^{\Delta\mathbf{K}} \mathbf{g} \tag{3.76}$$

A reduction in the number of coordinates is obtained if only some of the lower order characteristic modes are kept so that

$$\boldsymbol{\Phi}_{kcc}^{\Delta\mathbf{K}} = \begin{bmatrix} \phi_1 & \phi_2 & \cdots & \phi_k \end{bmatrix} \tag{3.77}$$

Consequently, the system matrices in coordinates $\mathbf{g}$ are

$$\mathbf{M}_g = \begin{bmatrix} \mathbf{I}_{kk} & \mathbf{m}_{kc}\boldsymbol{\Phi}_{kcc}^{\Delta\mathbf{K}} \\ \boldsymbol{\Phi}_{kcc}^{\Delta\mathbf{K}^T}\mathbf{m}_{kc}^T & \boldsymbol{\Phi}_{kcc}^{\Delta\mathbf{K}^T}\mathbf{M}_{cc}\boldsymbol{\Phi}_{kcc}^{\Delta\mathbf{K}} \end{bmatrix} \text{ and}$$

$$\mathbf{K}_g = \begin{bmatrix} \boldsymbol{\Lambda}_{kk} & 0 \\ 0 & \boldsymbol{\Phi}_{kcc}^{\Delta\mathbf{K}^T}\mathbf{K}_{cc}\boldsymbol{\Phi}_{kcc}^{\Delta\mathbf{K}} \end{bmatrix} \tag{3.78}$$

Finally, to calculate the response at DOF r due to an excitation at DOF e, equation (3.72) becomes

$$\mathbf{A}(r,e) = \mathbf{B}^{r*}\mathbf{S}\boldsymbol{\Phi}_{kcc}^{\mathbf{K}_{MPC}} \left[\mathbf{K}_g(1+i\eta) - \omega^2\mathbf{M}_g\right]^{-1} \boldsymbol{\Phi}_{kcc}^{\mathbf{K}_{MPC}^T}\mathbf{S}^T\mathbf{B}^{e*T} \tag{3.79}$$

where only $\boldsymbol{\Phi}_{cc}^{\mathbf{K}_{MPC}}$ needs to be recalculated for point connections at different locations.

3.4 A low rank update theory in the frequency domain

When there is uncertainty in the location of the connection point and MCS is being preferred, multiple evaluations of the FRFs are required. This can be computationally

expensive. In this section a method to improve the speed of the estimation of the response in physical coordinates **u** of a system with uncertainties in the point connections properties is described. This method uses a low rank update approach in the CMS framework. The low rank update is based on the Woodbury matrix identity [45] , which has been used extensively in signal processing [46–49] but lately being applied in the structural dynamics field [50–54]. The rank one version [55], also known as the Sherman Morrison identity, has also been applied for analysis of uncertainties in structural dynamics by Lecomte [32].

The response of a nominal system, i.e. the unassembled structure in **p** coordinates in the frequency domain is calculated as

$$x(\omega) = \mathbf{A}(\omega)^{-1}\mathbf{F} \tag{3.80}$$

where $\mathbf{A}(\omega)$ is the dynamic stiffness and is given by

$$\mathbf{A}(\omega) = \mathbf{K}_R(1+i\eta) - \omega^2\mathbf{M}_R \tag{3.81}$$

When a disturbance $\mathbf{D}(\omega)$ is added to the nominal system, equation (3.80) can be written as

$$\left[\mathbf{A}(\omega) + \mathbf{D}(\omega)\right]x'(\omega) = \mathbf{F} \tag{3.82}$$

where $x'(\omega)$ is the updated response and $\mathbf{D}(\omega)$ is the dynamic stiffness of the disturbance. It is assumed that $\mathbf{D}(\omega)$ is a low rank matrix and can be expressed as the outer product of given left and right vectors $\mathbf{d}_l$ and $\mathbf{d}_r$ as

$$\mathbf{D}(\omega) = \mathbf{d}_l(\omega)\mathbf{d}_r{}^T(\omega) \tag{3.83}$$

In the current analysis, the disturbance is given by the connection stiffness matrix $\mathbf{K}_{MPC}$ defined in equation 2.11 as function of the connection stiffness matrix in local physical coordinates $\Delta\mathbf{K}'$

$$\mathbf{K}_{MPC} = \left(\boldsymbol{\Gamma}\boldsymbol{\Xi}\right)^T \Delta\mathbf{K}' \, \boldsymbol{\Gamma}\boldsymbol{\Xi} \tag{3.84}$$

Equation (3.84) can be rewritten as an outer product of $\mathbf{d}_l$ and $\mathbf{d}_r$

$$\mathbf{D}(\omega) = \mathbf{K}_{MPC} = \mathbf{d}_l(\omega)\mathbf{d}_r{}^T(\omega) = \left(\boldsymbol{\Gamma}\boldsymbol{\Xi}\right)^T \Delta\mathbf{K}' \, \boldsymbol{\Gamma}\boldsymbol{\Xi} \tag{3.85}$$

where

$$\mathbf{d}_l = \left(\boldsymbol{\Gamma}\boldsymbol{\Xi}\right)^T \tag{3.86}$$

and

$$\mathbf{d}_r{}^T = \Delta\mathbf{K}' \, \boldsymbol{\Gamma}\boldsymbol{\Xi} \tag{3.87}$$

It can be seen that when the system is disturbed by an MPC connection the assumption that the disturbance is a low rank matrix is always perfectly met.

Substituting equation (3.83) into equation (3.82) and after some manipulation leads to

$$x'(\omega) = \mathbf{A}(\omega)^{-1}\left[\mathbf{F} + \mathbf{d}_l\mathbf{d}_r{}^T x'(\omega)\right] \tag{3.88}$$

it can be seen that $x'(\omega)$ occurs on both sides of the equation. To solve this equation, expression (3.88) can be premultiplied by $\mathbf{d}_r{}^T$ and manipulated in order to obtain

$$\mathbf{d}_r{}^T x'(\omega) = \left[\mathbf{I} - \mathbf{d}_r{}^T \mathbf{A}(\omega)^{-1} \mathbf{d}_l\right]^{-1} \mathbf{d}_r{}^T \mathbf{A}(\omega)^{-1} \mathbf{F} \tag{3.89}$$

Substituting this expression into the right hand side of equation (3.88) gives

$$x'(\omega) = \mathbf{A}'(\omega)^{-1} \mathbf{F} \tag{3.90}$$

where

$$\mathbf{A}'(\omega)^{-1} = \left[\mathbf{A}(\omega)^{-1} + \mathbf{A}(\omega)^{-1} \mathbf{d}_l \left[\mathbf{I} - \mathbf{d}_r{}^T \mathbf{A}(\omega)^{-1} \mathbf{d}_l\right]^{-1} \mathbf{d}_r{}^T \mathbf{A}(\omega)^{-1}\right] \tag{3.91}$$

Finally, the response in coordinates **p** can be transformed into physical coordinates **u** can be performed using equation (3.69) as

$$\mathbf{A}(r,e) = \mathbf{B}^{r*}\mathbf{S}\left[\mathbf{A}(\omega)^{-1}\mathbf{F} + \mathbf{A}(\omega)^{-1}\mathbf{d}_l\left[\mathbf{I} - \mathbf{d}_r{}^T\mathbf{A}(\omega)^{-1}\mathbf{d}_l\right]^{-1}\mathbf{d}_r{}^T\mathbf{A}(\omega)^{-1}\mathbf{F}\right]\mathbf{S}^T\mathbf{B}^{e*T} \tag{3.92}$$

Substituting equations (3.86) and (3.87) into this expression and some manipulation leads to

$$\begin{aligned}&\mathbf{A}(r,e) = \mathbf{B}^{r*}\mathbf{S}\mathbf{A}(\omega)^{-1}\mathbf{F}\mathbf{S}^T\mathbf{B}^{e*T} + \\ &\left[\mathbf{B}^{r*}\mathbf{S}\mathbf{A}(\omega)^{-1}\Xi^T\boldsymbol{\Gamma}^T\right]\left[\left[\mathbf{I} - \Delta\mathbf{K}'\boldsymbol{\Gamma}\Xi\mathbf{A}(\omega)^{-1}\Xi^T\boldsymbol{\Gamma}^T\right]^{-1}\Delta\mathbf{K}'\right]\left[\boldsymbol{\Gamma}\Xi\mathbf{A}(\omega)^{-1}\mathbf{F}\mathbf{S}^T\mathbf{B}^{e*T}\right]\end{aligned} \tag{3.93}$$

where the first term represents the transfer function of the nominal unperturbed system. The second term represents the effect of the perturbation to the transfer function, here the first factor represents the transfer function between the response DOFs to the connection location in the first unperturbed subsystem; the second factor represents the full receptance matrix of the connection in local DOFs considering the disturbed system and finally the third factor represents the transfer function from the location of

the connection to the excitation location in the second unperturbed subsystem, this is illustrated in Figure 3.5.

Given the separation of terms, it can be seen that the transfer functions of the unperturbed system could be replaced by FRFs measured experimentally giving a framework for hybrid analysis.

In order to improve the efficiency of evaluating equation (3.93), when applied in a MCS, it can be re-arranged as

$$\begin{aligned}\mathbf{A}(r,e) &= \mathbf{B}^{r*}\mathbf{S}\mathbf{A}(\omega)^{-1}\mathbf{F}\mathbf{S}^{T}\mathbf{B}^{e*T} + \\ &\left[\mathbf{B}^{r*}\mathbf{S}\mathbf{A}(\omega)^{-1}\Xi^{T}\right]\left[\mathbf{\Gamma}^{T}\left[\mathbf{I}-\Delta\mathbf{K}\mathbf{T}\Xi\mathbf{A}(\omega)^{-1}\Xi^{T}\mathbf{\Gamma}^{T}\right]^{-1}\Delta\mathbf{K}\mathbf{T}\right]\left[\Xi\mathbf{A}(\omega)^{-1}\mathbf{F}\mathbf{S}^{T}\mathbf{B}^{e*T}\right]\end{aligned} \tag{3.94}$$

When equation (3.94) is used to calculate the response of a system with uncertain point connections, the efficiency is improved in the following ways: (i) $\mathbf{A}(\omega)^{-1}$, Ξ, $\mathbf{B}$ and $\mathbf{S}$ are invariant to changes in the connections, therefore they are calculated only once during a MCS. Hence, the first term and the first and third factors in the second term are calculated only once in the MCS. (ii) $\mathbf{A}(\omega)^{-1}$ is calculated in the CMS co-ordinates, therefore the size of the matrices are smaller in comparison to the original matrices of the system. (iii) Since the first and third factors in the second term are vectors, the final multiplication is computationally cheap. (iii) The computational effort to invert the second factor of the second term is small since the sizes of the matrices to be inverted is equal to the number of DOFs in the connection.

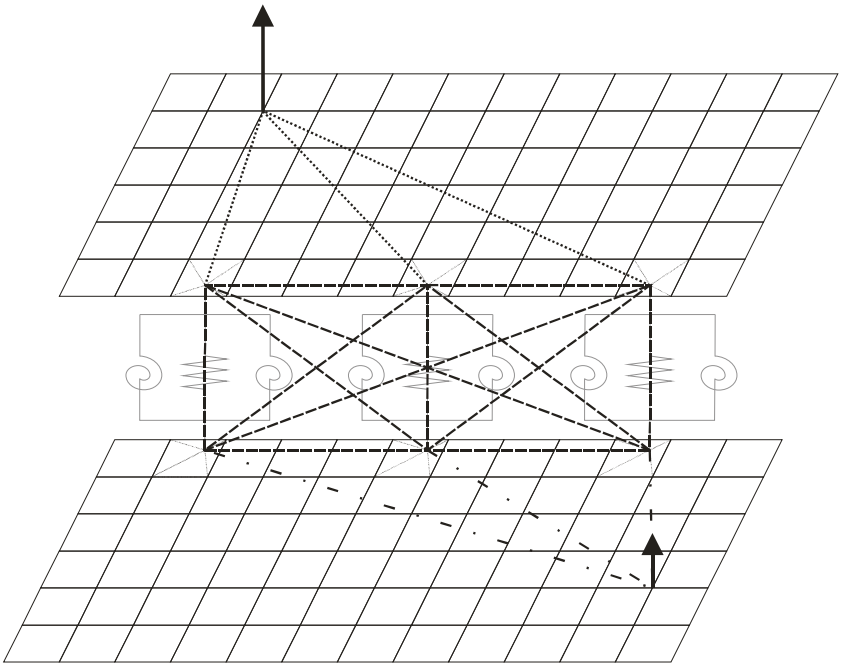

Figure 3.5: Graphical representation of the second term in equation (3.93): ····· first factor; — — — second factor; — · — · third factor.

3.5 Numerical Example

The numerical example is a system of two plates with free edges and five elastic connections as shown in Figure 3.6. The plates are modelled using a mesh of 22x22 and 22x20 heterosis elements [28] and any offset in the plates was ignored, (i.e. both plates have the the same centerline). In order to avoid symmetry in the *x* and *y* direction, the first plate is 10% wider and 10% thicker than the second plate. The properties for each plate are given in Table 3-1.

The stiffnesses values of all five connections are $K_w = 1\times10^{12}$ N/m and $K_{\theta x} = K_{\theta y} = 1\times10^{4}$ Nm/rad . As a baseline, the connections are located at the midpoint of the area in which the position varies, represented as the shaded elements in Figure 3.6.

Using this configuration, the transfer mobility from coordinate (x_1, y_1) = (0.0836, 0.0364) in plate 1 to coordinate (x_2, y_2) = (0.0836, 0.0836) in plate 2 was evaluated using a full modal solution and two different approximations: (1) CMS in which only the first 30 normal modes of each component were kept and 710 constraint modes, here

the DOFs are reduced from 10686 to 770; (2) CMS and truncation of the characteristic constraint modes using equation (3.79), in which only 16 modes were kept from a total of 710 constraint modes in order to keep the prediction error lower than 1% for all frequencies below 1000 Hz when compared to the full solution; (3) CMS matrices solved using a low rank update theory as in equation (3.93), this method is exact when compared to the CMS method, no additional approximations are made, therefore a maximum error of 0.5% can be maintained.

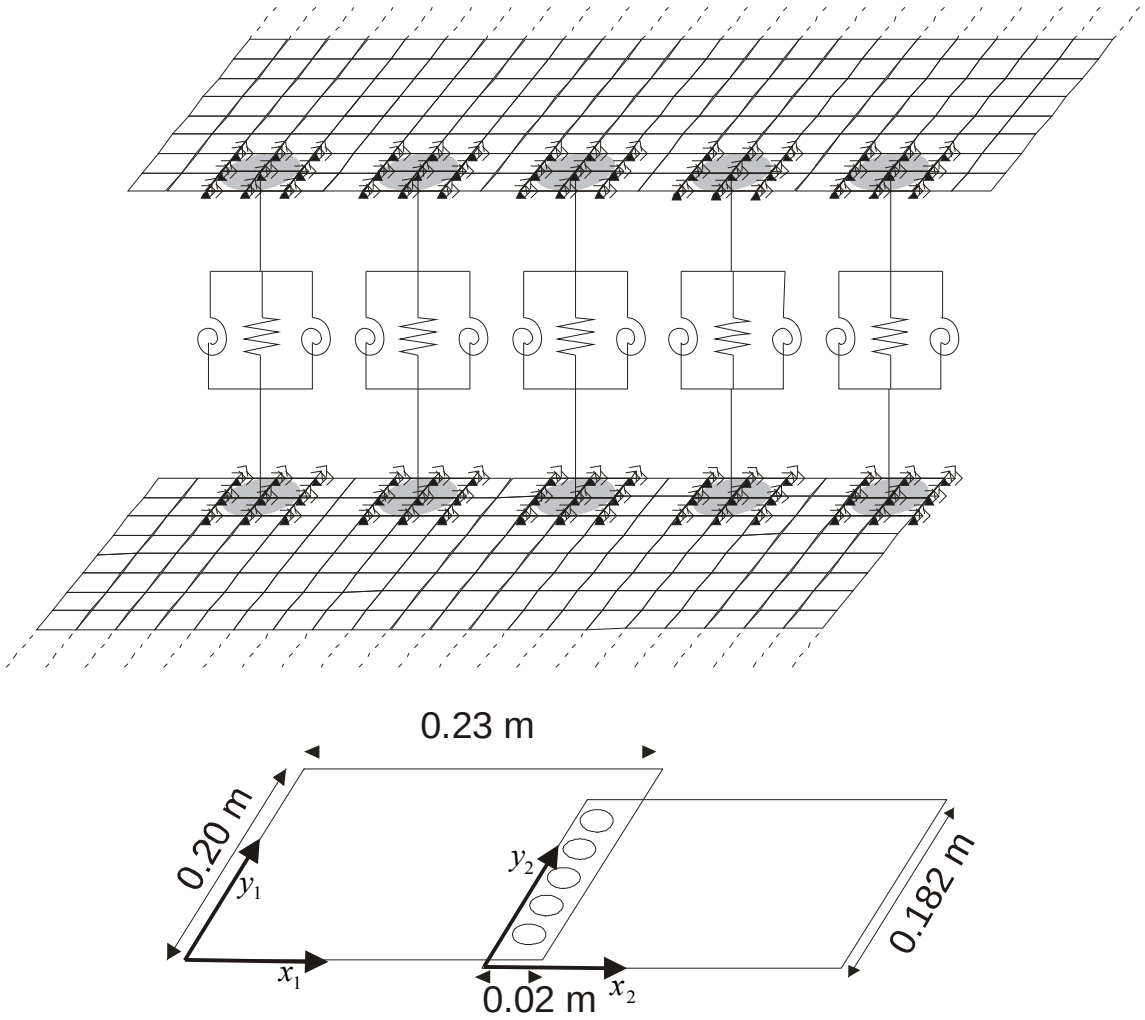

Figure 3.6: Two free plates assembled with five elastic point connections.

	L_x (m)	L_y (m)	h (m)	ρ (kg/m^3)	E (N/m^2)	υ
Plate (1)	0.23	0.2	0.0022	7860	2.07E+11	0.3
Plate (2)	0.23	0.182	0.002	7860	2.07E+11	0.3

Table 3-1: Properties of the plates.

The low rank update approach is more accurate than the reduced characteristic constraint modes approach since it does not involve further approximations. This can be observed in Figure 3.7. Even though it was ensured to keep a good agreement in the CMS methods below 1000Hz, it can be seen that the solutions start to deviate from the full modal solution especially the CMS + characteristic constraint modes method.

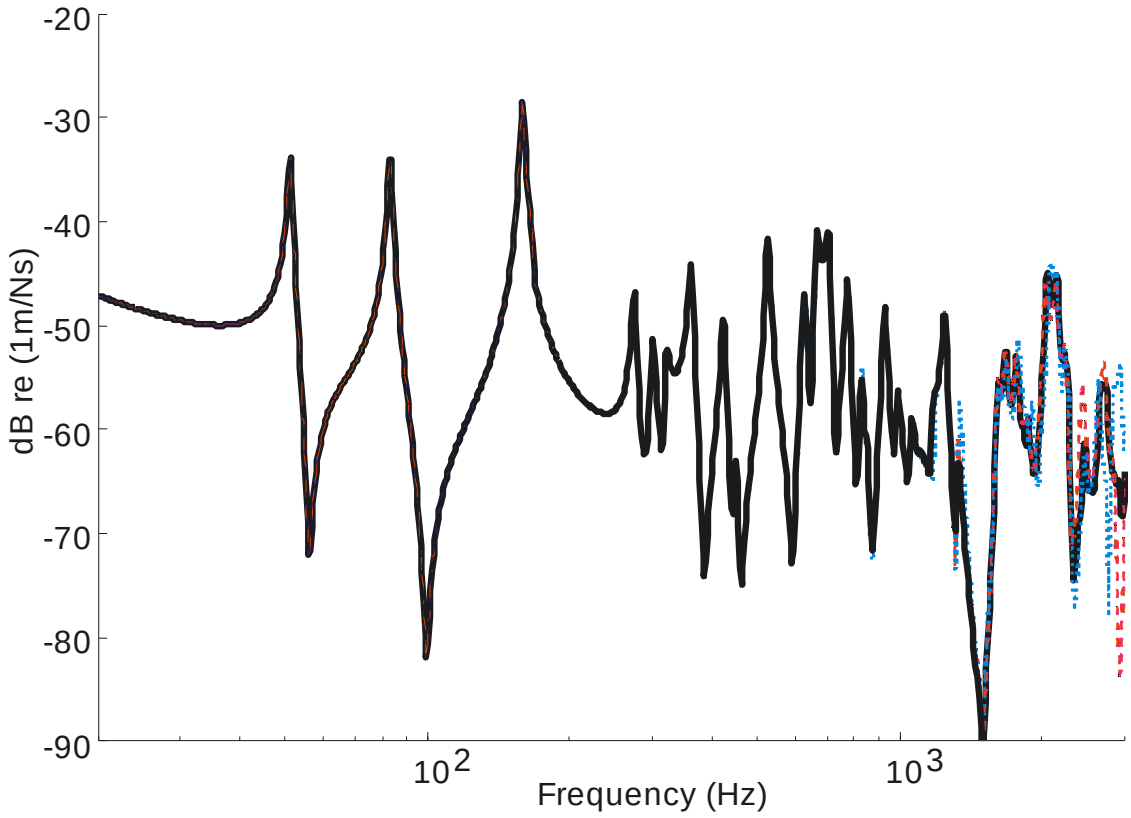

Figure 3.7: Transfer mobility of the baseline configuration: ——— full modal solution; – – – – CMS and 16 kept characteristic constraint modes; – – – CMS and update theory.

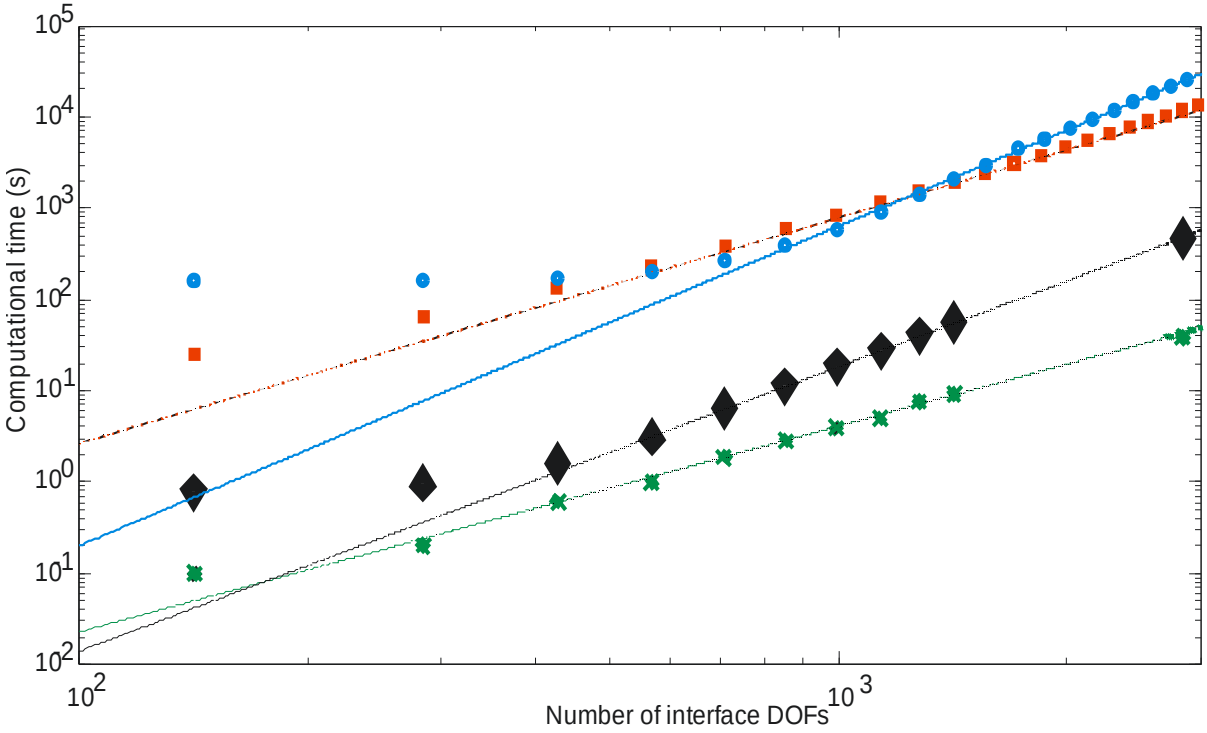

Figure 3.8: Computational time when evaluating FRFs as function of the number of interface DOFs: ● full modal solution; ■ CMS; ◆ CMS and characteristic constraint modes; ✖ CMS and update theory; ····· ; $t = 7\times10^{-7} N^{2.25}$, ----- $t = 8\times10^{-9} N^{3.12}$ — · — $t = 3\times10^{-5} N^{2.47}$; —— $t = 2\times10^{-8} N^{3.5}$ . .

The low-rank update approach leads to approximately 99% reduction in the computational time when compared to the pure CMS method, as can be seen in Figure 3.8. When the number of interface DOFs N is large ($N > 1000$) it saves nearly 90% in the computational time when compared to the CMS with truncated characteristic constraint modes. The computational time for this approach depends mainly on the number of connections since it defines the size of the inverse operation, but it is also determined to a lesser extent by the number of interface DOFs because this number defines the size of the rest of the matrix operations (i.e. multiplications and additions) as can be seen in equation (3.93). On the other hand, when the characteristic constraint method is used to reduce the size of the problem, the computational time depends almost entirely on the number of interface DOFs, since the most expensive operation performed when this method is used is the eigenvalue solution of the mass and stiffness matrices of the constrained DOFs.

The dependence of the computational time when evaluating the FRFs on the number of interface DOFs of all methods is shown in Figure 3.8. The update theory method is not

only cheaper than any other method but also scales better with the number of interface DOFs, N, growing for large N as $N^{2.25}$ as compared to $N^{3.12}$ for the CMS and characteristic constraint modes method. Therefore, the proposed approach reduces the computational time by factor of approximately N [56]. If the computational time is extrapolated for a full body in white with 3000 spot welds and 1.26×10^5 DOFs (42 DOFs per spot weld) it would take 2.4 days to solve the model using the proposed method. This number can be further improved using optimized algorithms and parallel computing with larger number of processors and increased RAM memory.

The results show that for FRFs calculation, the update theory is the preferred method, it is the cheapest method at all ranges on N and scales much better. However, if the statistics of the natural frequencies and mode shapes need to be computed when the update theory approach is followed, the calculation of the natural frequencies and modeshapes would lead to a different analysis, (i.e. would require a further modal analysis) and a considerable increase in the computational cost. On the other hand, using the characteristic constraint method there is not an increment in the computational cost when the natural frequencies and modeshapes are calculated.

3.5.1 Uncertainty analysis

As reference, the first four natural frequencies and modeshapes of the baseline condition will be analyzed. In this condition all the connections are located at the centre of the regions in which the position are allowed to change. Strain energy in the assembly is also analyzed.

The first natural frequency is a fundamental flexural mode in which the midline of the assembly experiences large deflections while the strain is maximum at the locations of the connections as can be observed in Figure 3.9 and Figure 3.10. The second natural frequency is a fundamental torsional mode in which the displacement is minimum at the connections location, however the strain is maximum at the midline of the assembly and equally distributed on the overlap area. The next mode is a second bending mode in which the displacement and strain are minimum at the midline and in general over the overlapped area. Finally, the fourth mode is a mixed third bending mode with cross

bending. In this case, the displacement and strain are maximum again in the midline of the assembly, but due to the presence of cross deflection, the strain energy is maximum at the outer connections.

For the uncertainty analysis, a MCS with 500 samples is used to estimate the envelope of the transfer mobility. The (x_i, y_i) coordinates of each of the i point connections are independent Gaussian random variables with their mean (μ_{xi}, μ_{yi}) located at the baseline position and

$$\sigma_{xi} = 0.25 S_x \text{ and } \sigma_{yi} = 0.25 S_y \tag{3.95}$$

where S_x and S_y are the x and y length of each element. In this case, the samples for which the coordinates of the point connection lay outside the element were discarded (<0.1% of the sampled locations).

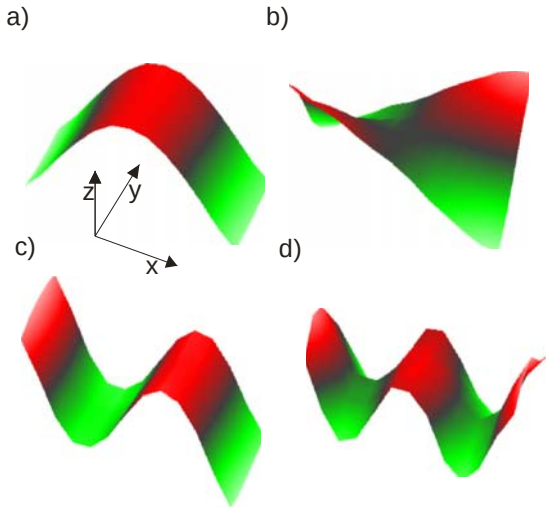

Figure 3.9: Modeshapes for the baseline condition

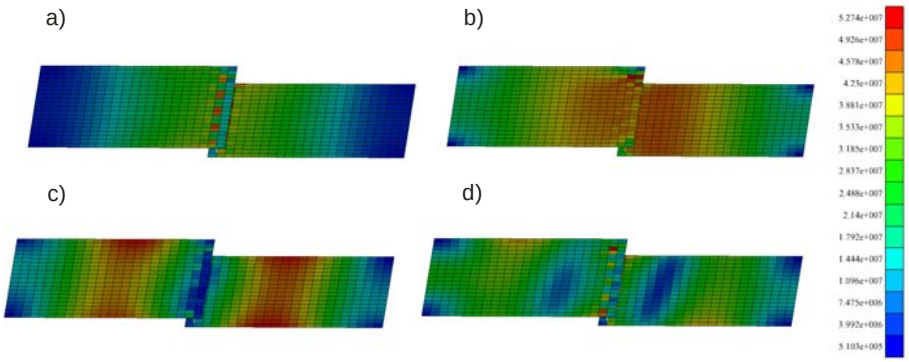

Figure 3.10: Strain energy computed for the first four assembly modeshapes.

Being the most time efficient method to calculate the FRFs in a MCS, the low rank update method is then applied for the subsequent uncertainty analysis.

The results from the MCS can be observed in Figure 3.11, where the FRF envelopes is together with the baseline FRF. Here it can be noted that the first and fourth natural frequencies are more sensitive to the connection locations since the strain energy is concentrated in the connections, small changes in its location affect the stiffness of the assembly in that area impacting on these natural frequencies. For the second and third natural frequencies, the strain is equally distributed in the overlapped area (where the connections lie), therefore these natural frequencies are less sensitive to changes in the connections (see Figure 3.9 and Figure 3.10).

For the baseline configuration for which all the connections lie at the midline, the natural frequencies are close to the maximum values within the MCS results since the midline experiences the highest strain values; when the spot welds deviate from this line the modal stiffness in the assembly is reduced. This means that the natural frequencies for the case in which the connections are in the mean location i.e. $(x_i, y_i) = (\mu_{xi}, \mu_{yi})$ are different to the mean natural frequencies of the ensemble (Figure 3.11 and Figure 3.12). The probability density functions (PDFs) of the natural frequencies are not Gaussian, even though (x_i, y_i) are Gaussian variables, as can be observed in Figure 3.12.

3.5.1.1 Broken or missing weld

In order to estimate the variability in the vibration response of this system due to missing or broken welds when the position of the remaining welds is uncertain, a MCS with 500 samples is used to estimate the envelope of the transfer mobility. The (x_i, y_i) coordinates of each of the *i* point connections are assumed to be independent Gaussian random variables with their means (μ_{xi}, μ_{yi}) located at the baseline position and their standard deviation are given by equation (3.95).

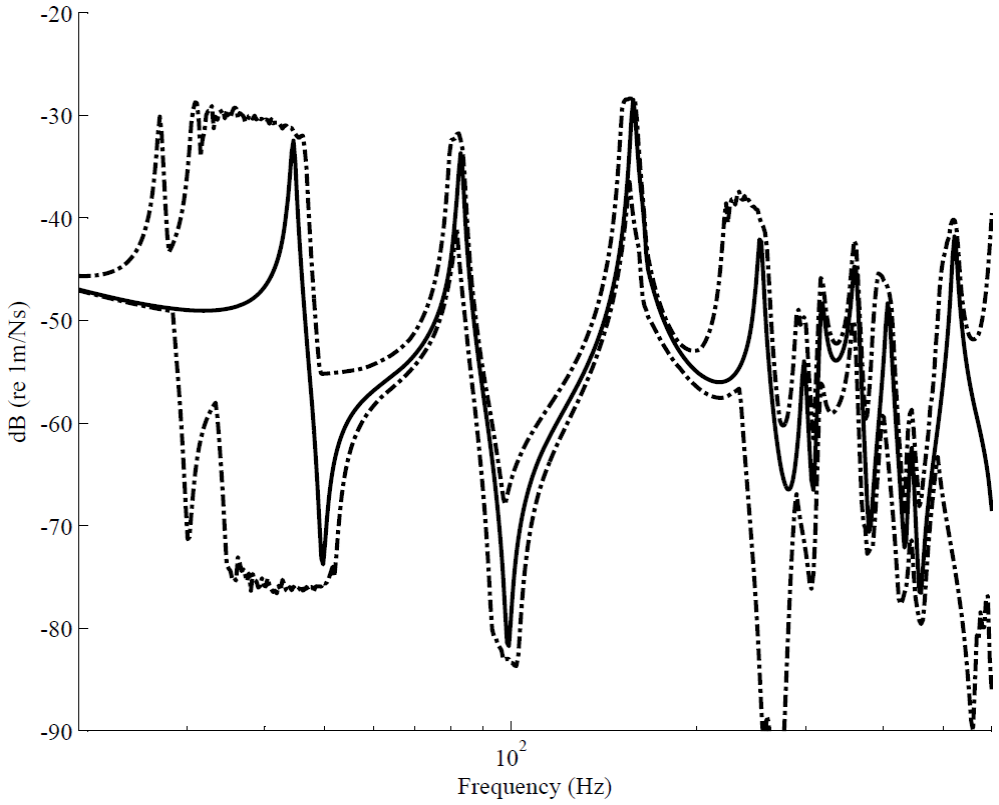

Figure 3.11: Response envelopes for the magnitude of the transfer mobility using MCS with 500 samples: – · – · – Maximum-minimum; ——— baseline.

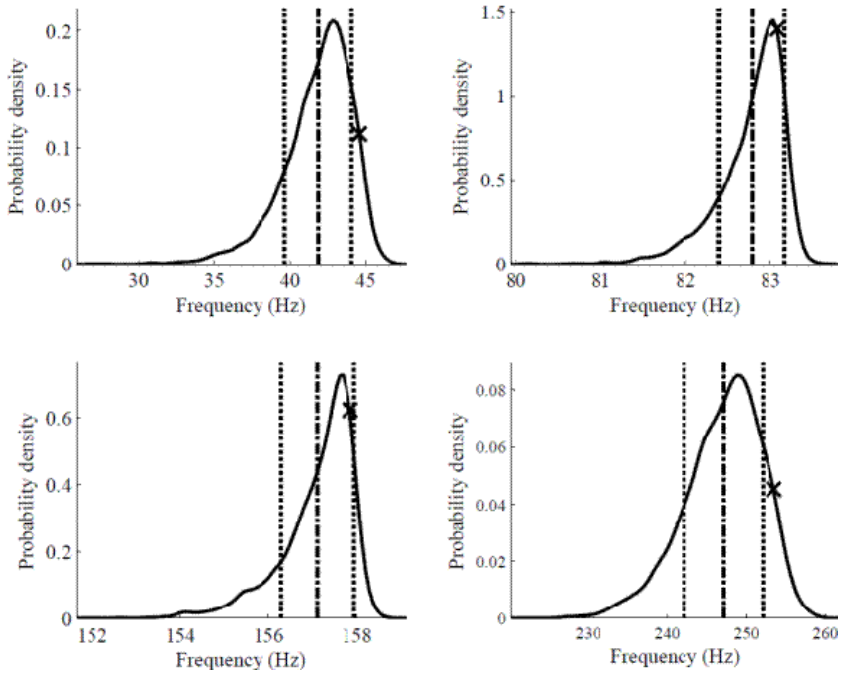

Figure 3.12: PDFs of the natural frequencies for MCS with 500 samples: (a) first ; (b) second; (c) third; (d) fourth natural frequencies: ——— MCS; −·−·− $\bar{\omega}_n$; ✖ $\omega_n^{(\mu_{xi},\mu_{yi})}$; ------ $\bar{\omega}_n \pm$ one standard deviation.

The stiffness of a missing or broken weld is set to zero. In doing so, the inverse of the unperturbed system and the CMS matrices do not need to be re-calculated. The 5 to 95% response envelope is computed for five cases; in each case one of the five spot welds is absent. This envelope is then compared to the random case with no absent connections. The results are shown in Figure 3.13.

When any spot weld is absent, the translational and rotational stiffness of the joint is reduced. This affects especially the first flexural mode since the strain energy is concentrated in the connections as can be observed in Figure 3.10. Then, the bounds of the first natural frequency are extended, especially when the outer connections are broken. This effect can be observed in Figure 3.13. On the other hand, the third natural frequency is relatively insensitive when any of the connections is absent because the strain energy is higher in the middle of the individual plates and lower in the connection area.

In general, the response is not affected greatly when the inner spot welds are missing. However, when the outer spot welds are missing there is a general change in the response envelopes as can be observed in Figure 3.13 (a) and Figure 3.13 (e).

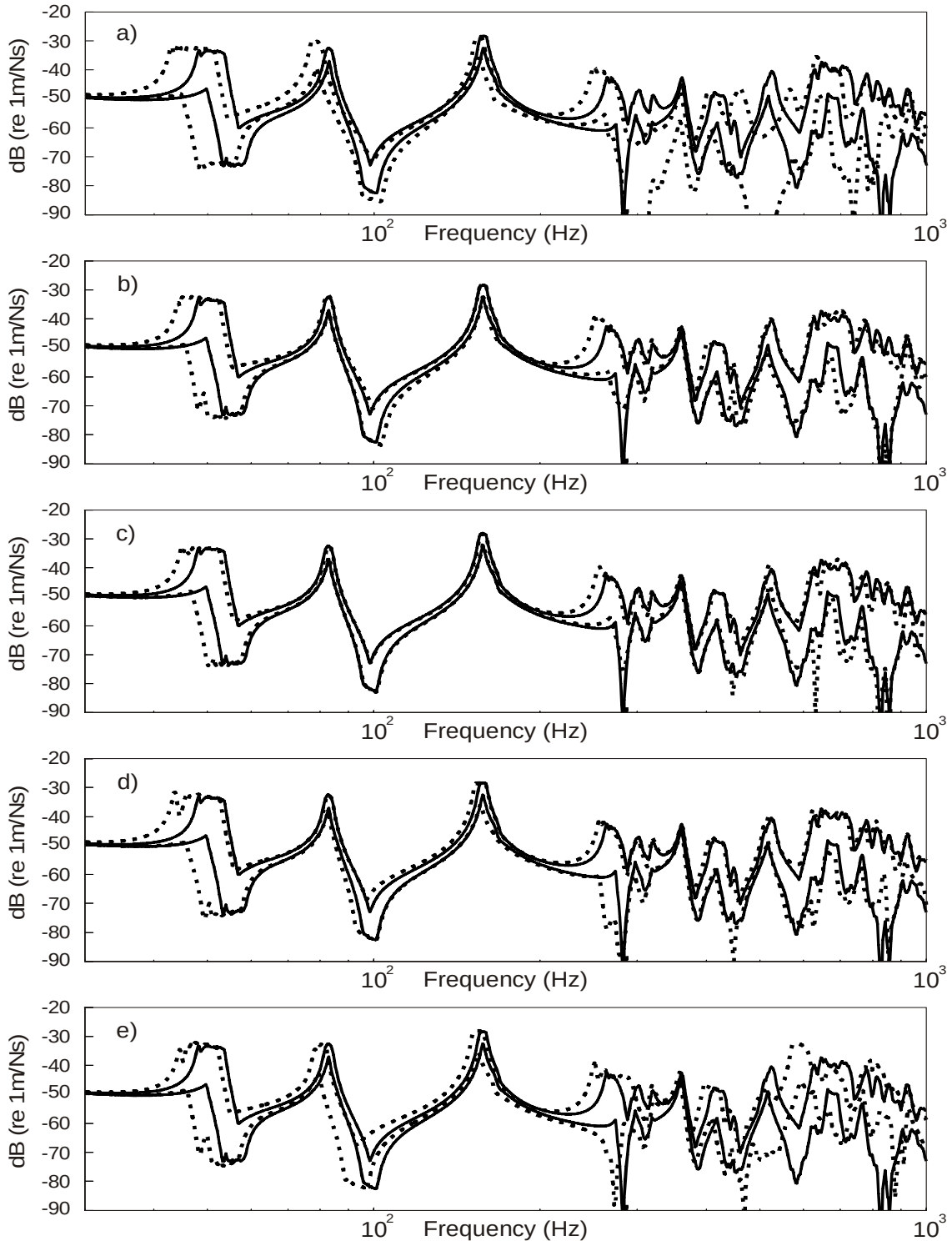

Figure 3.13: 5%-95% response envelopes for the magnitude of the transfer mobility using MCS with 500 samples: a) first; b) second; c)third; d)fourth; e)fifth spot weld being absent; —— baseline ▪▪▪▪▪▪ absent spot weld.

3.6 Conclusions

In this chapter multipoint constraints (MPC) in combination with component mode synthesis (CMS) were used to predict the response where there are uncertainties in the joint locations in a finite element (FE) model.

In chapter 2 it was shown that an MPC connection can accurately model the effects due to a change in the location of the joint. In this chapter it was seen that CMS gives a sub-structuring framework and a reduction in the number of the degrees of freedom (DOF) of the model. Combining both approaches, the response of the system can be evaluated for any connection location using the unchanged modal representation of the substructures in an accurate and numerically efficient manner.

However, when the number of degrees of boundary DOFs is large, then the CMS size reduction is less efficient since the number of the interface DOFs is not reduced. Two techniques are proposed to overcome this problem: (i) characteristic constraint modes [22] and (ii) low rank update theory [32].

The vibration response was calculated using these approaches for different connection positions and compared to a full modal solution. The predictions obtained gave a good agreement and the computational time was reduced by approximately 99% when compared to the full modal solution. When compared to the characteristic constraint mode method, the low rank update approach leads to a reduction in the computational time t at a rate of $t^{2/3}$.

The last approach was used in a Monte Carlo simulation (MCS) with 500 samples to evaluate the variability in the vibration response. The results show that probability density functions (PDFs) of the system natural frequencies are not Gaussian even though the connection locations are Gaussian variables.

Finally, a second MCS was used to evaluate the variability in the vibrational response due to missing or broken connections and/or uncertainty in the location of the spot-welds in a model of two plates with five spot welds. Results show that, for the example

considered, when any of the inner spot welds is missing and the location and size of the remaining connections is uncertain the vibration responses lie approximately within the bounds of the case in which all the connections are present. On the other hand, when any of the outer connections are absent the variability in the vibration response is greater.

4 A ROBUST SPOT WELD MODEL BASED ON MPC CONNECTIONS

As mentioned before, the spot weld is one of the most important structural joints in the automotive industry; a vehicle body typically contains thousands of spot-welds. The finite element (FE) method can be used to analyze spot welded structures and several models have been proposed in the literature. However, there are still issues in the application of these models.

In Chapter 2 it was seen that when MPCs are used to connect the elastic component to the substructures (solid, beam or springs) [7], [10], the connection can be placed at any location using the existing surface meshes. This latter feature offers a great advantage, since it is then possible to assemble components with different mesh characteristics or to assemble components with complex geometries, for which it is very difficult to have coincident nodes. Unfortunately, it was also seen in Chapter 2 that when a rotational spring is used in the spot weld model, the transfer mobility magnitude is sensitive to the element size. Moreover, Palmonella et al. identified the element area as a parameter that can be updated in order to reduce the error in the prediction of dynamic properties in a FE model when compared to experimental measurements [57]. It has also been found that for dynamic predictions, some of the lowest natural frequencies do not converge even if the element size is much smaller than the wavelength [58], [59].

In this study the cause of the large sensitivity to element size is identified and in order to overcome this difficulty a spot weld model base on MPC connections is proposed.

This model provides a better physical representation of the spot weld and as a result the forces at the connections are distributed over an area imposing a surface to surface link between the structures. This model is robust to changes in the mesh size and coincident meshes are not required.

In the following section the sensitivity of spot weld models to element size is discussed and demonstrated in an example of two simply supported plates with a single connection; which is the same example used in section 2.3.4. In section 4.2 a spot weld model robust to element size is proposed. In section 4.3 the application of the new spot-weld model is demonstrated in a model of two simply supported plates with three point connections. In order to evaluate the performance of the proposed element, mesh sensitivity and convergence are evaluated. The resulting natural frequencies are compared to experimental measurements. Finally conclusions are given in section 4.4.

4.1 SENSITIVITY OF SPOT WELD MODELS TO ELEMENT SIZE

In this section the sensitivity of the diagonal terms in the stiffness matrix of a Heterosis element with respect to element size is discussed. When the out of plane behaviour is studied, it is seen that the terms associated with the rotational DOFs are sensitive to the element size.

When two plates are connected using any of the existing spot weld models, constant stiffness values are added to all the diagonal terms of the DOFs involved in the connection. The magnitude of the plate rotational stiffness depends on the element size, while the added rotational stiffness does not, resulting in natural frequencies and/or dynamic or static solutions that are sensitive to element size.

To illustrate this, consider the Heterosis plate element [28]. This is a plate element derived from the Mindlin-Reissner plate theory. Midlin-Reissner plate theory is used to describe thick plates behaviour, however, as reduced order integration is used to evaluate the shear stiffness matrix, this element does not suffer from shear locking, possesses correct rank and can be applied to both thick and thin plates. This element is

described in detail in section 2.3.1.2. The out-of-plane co-ordinates $\left(w,\theta_x,\theta_y\right)$ of a point within the element are described in equations (2.37),(2.38) and (2.39). These equations can be written in matrix form as

$$\begin{Bmatrix} w(x,y) \\ \theta_x(x,y) \\ \theta_y(x,y) \end{Bmatrix} = \begin{bmatrix} \mathbf{N}^T & 0 & 0 \\ 0 & \mathbf{P}^T & 0 \\ 0 & 0 & \mathbf{P}^T \end{bmatrix} \mathbf{d}_e \tag{4.1}$$

where the nodal displacement vector is given by

$$\mathbf{d}_e = \begin{bmatrix} \mathbf{w}_j^T & \boldsymbol{\theta}_{x,j}^T & \boldsymbol{\theta}_{y,j}^T \end{bmatrix}^T \tag{4.2}$$

where j indicates the node number.

For out-of-plane vibration, the stiffness matrix of a plane isotropic element based on Mindlin-Reissner plate theory comprises bending and shear contributions [60], i.e.

$$\mathbf{K} = \mathbf{K}_b + \mathbf{K}_s \tag{4.3}$$

where the bending contribution to the element stiffness matrix can be expressed as

$$\mathbf{K}_b = \frac{t^3}{12}\int_A \left(\mathbf{B}_b^T \mathbf{D}_b \mathbf{B}_b\right) dA \tag{4.4}$$

and the contribution from the shear stiffness is given by

$$\mathbf{K}_s = t\int_A \left(\mathbf{B}_s^T \mathbf{D}_s \mathbf{B}_s\right) dA \tag{4.5}$$

where A is the area of the element, $\mathbf{B}_b$ and $\mathbf{B}_s$ are the strain-displacement matrices given by

$$\mathbf{B}_b = \begin{bmatrix} 0 & 0 & \dfrac{\partial \mathbf{P}^T}{\partial x} \\ 0 & -\dfrac{\partial \mathbf{P}^T}{\partial y} & 0 \\ 0 & -\dfrac{\partial \mathbf{P}^T}{\partial x} & \dfrac{\partial \mathbf{P}^T}{\partial y} \end{bmatrix}, \; \mathbf{B}_s = \begin{bmatrix} \dfrac{\partial \mathbf{N}^T}{\partial x} & 0 & \mathbf{P}^T \\ \dfrac{\partial \mathbf{N}^T}{\partial y} & -\mathbf{P}^T & 0 \end{bmatrix} \tag{4.6}$$

and the matrices of the material constants are

$$\mathbf{D}_b = \frac{E}{\left(1-v^2\right)} \begin{bmatrix} 1 & v & 0 \\ v & 1 & 0 \\ 0 & 0 & \dfrac{(1-v)}{2} \end{bmatrix}, \mathbf{D}_s = \begin{bmatrix} \kappa G & 0 \\ 0 & \kappa G \end{bmatrix} \tag{4.7}$$

where E is the Young's modulus, v is the Poissons ratio, G is the shear modulus and κ is the shear correction factor. The shear correction factor is an empirical constant applied to improve the accuracy of the predicted wave velocity. Generally this constant is taken to be 5/6.

Since the basis functions $\mathbf{N}$ and $\mathbf{P}$ in equation (4.6) are defined in terms of ξ and η, the appropriate derivatives are then given by

$$\begin{bmatrix} \dfrac{\partial \mathbf{N}^T}{\partial x} \\ \dfrac{\partial \mathbf{N}^T}{\partial y} \end{bmatrix} = \mathbf{J}^{-1} \begin{bmatrix} \dfrac{\partial \mathbf{N}^T}{\partial \xi} \\ \dfrac{\partial \mathbf{N}^T}{\partial \eta} \end{bmatrix}; \begin{bmatrix} \dfrac{\partial \mathbf{N}^T}{\partial x} \\ \dfrac{\partial \mathbf{N}^T}{\partial y} \end{bmatrix} = \mathbf{J}^{-1} \begin{bmatrix} \dfrac{\partial \mathbf{N}^T}{\partial \xi} \\ \dfrac{\partial \mathbf{N}^T}{\partial \eta} \end{bmatrix}; \begin{bmatrix} \dfrac{\partial \mathbf{P}^T}{\partial x} \\ \dfrac{\partial \mathbf{P}^T}{\partial y} \end{bmatrix} = \mathbf{J}^{-1} \begin{bmatrix} \dfrac{\partial \mathbf{P}^T}{\partial \xi} \\ \dfrac{\partial \mathbf{P}^T}{\partial \eta} \end{bmatrix} \tag{4.8}$$

where $\mathbf{J}$ is the Jacobian transformation matrix

$$\mathbf{J} = \begin{bmatrix} \dfrac{\partial x}{\partial \xi} & \dfrac{\partial y}{\partial \xi} \\ \dfrac{\partial x}{\partial \eta} & \dfrac{\partial y}{\partial \eta} \end{bmatrix} \tag{4.9}$$

Rather than evaluating the integrals in equations (4.4) and (4.5) in physical coordinates, it is more convenient to evaluate the integral over the non-dimensional domain (ξ,η), resulting in

$$\mathbf{K}_b = \frac{t^3}{12}\int_{-1}^{1}\int_{-1}^{1}\left(\mathbf{B}_b^T\mathbf{D}_b\mathbf{B}_b\right)|\mathbf{J}|d\xi d\eta \tag{4.10}$$

and

$$\mathbf{K}_s = t\int_{-1}^{1}\int_{-1}^{1}\left(\mathbf{B}_s^T\mathbf{D}_s\mathbf{B}_s\right)|\mathbf{J}|d\xi d\eta \tag{4.11}$$

When the integrals in equations (4.10) and (4.11) are evaluated it is found that the values for the rotational DOFs in the leading diagonals of $\mathbf{K}_b$ and $\mathbf{K}_s$ are

$$K_{b(\theta x,\theta x)} = K_{b(\theta y,\theta y)} = C_b\frac{Et^3\left(1-\nu/3\right)}{1-\nu^2} \tag{4.12}$$

and

$$K_{s(\theta x,\theta x)} = K_{s(\theta y,\theta y)} = C_s\frac{Ets_x s_y}{(1+\nu)} \tag{4.13}$$

where C_b and C_s are constants that depend on the node number, mesh characteristics, the shape functions and the integration scheme used in the particular element formulation. For example for the first corner node in the Heterosis element,

$$C_b \approx 0.0389 \text{ and } C_s \approx 0.00514 \tag{4.14}$$

Following equations (4.12), (4.13) and (4.3), the stiffnesses values for the rotational DOFs are

$$K_{(\theta x,\theta x)} = K_{(\theta y,\theta y)} = C_b \left(\frac{Et^3}{\left(1-v^2\right)} \right) \left(1-\frac{v}{3}\right) + C_s \frac{Ets_x s_y}{\left(1+v\right)} \tag{4.15}$$

The relative contributions to these rotational stiffnesses from the bending and shear contributions are:

$$\frac{K_{s(\theta x,\theta x)}}{K_{b(\theta x,\theta x)}} = \frac{C_s}{C_b} \left(\frac{3-v}{3\left(1-v\right)} \right) \left(\frac{s_x s_y}{t^2} \right) \tag{4.16}$$

Thus the contribution to the total stiffness from the shear term is large compared to that of the bending contribution except when the element dimensions (width and length) are much smaller than the thickness t, i.e. $s_x, s_y << t$. Hence the rotational stiffness terms in the leading diagonal of the element stiffness matrix depends on the element dimensions.

In contrast, the value for the translational degrees of freedom in the stiffness matrix is independent of s_x, s_y, the bending contribution is equal to zero, and the shear contribution is given by

$$K_{(w,w)} = C_{s,w} \frac{Et}{\left(1+v\right)} \tag{4.17}$$

As can be seen in equation (4.15), the rotational stiffness values in the element matrix depends on the element length. On the other hand, the rotational stiffnesses of the general spot weld models (CWELD, ACM2 and the simple MCP connection) are constant and independent of the element size [7], [10], [61]. Therefore, when the

stiffness matrices are assembled, the relative magnitude of the rotational stiffness added to the substructure stiffness depends on the element size, resulting in solutions which are sensitive to the element size. This effect is illustrated in the following example.

4.1.1 Numerical example

The numerical example used in this section is the same used in section 2.3.4: a system of two simply supported plates with a single elastic connection as shown in Figure 2.9. The material and geometric properties are given in Table 2-2. The plates are modelled using a mesh of identical rectangular Heterosis elements. Different element sizes ranging from 0.006 to 0.12 m are chosen in order to calculate the static deformation at point (0.38, 0.32) in plate 2 to a force at coordinate (0.38, 0.32) in plate 1.

The connection is modelled using the same MPC connection described in section 2.1. Two cases are analyzed when either a single translational or rotational spring is used. In the first, the translational and rotational spring stiffnesses are $K_w = 16000$ N/m , $K_{\theta x} = 0$ Nm/rad and $K_{\theta y} = 0$ Nm/rad respectively; the second case corresponds to $K_w = 0$ N/m , $K_{\theta x} = 1600$ Nm/rad and $K_{\theta y} = 0$ Nm/rad . An analytical solution of this system was estimated using a mobility approach in section 2.3. The numerical results are compared to this analytical solution and are presented in Figure 4.1. It can be seen that in the case in which only a rotational spring connects the plates (case 2) the static solution depends on the element size and does not converge as the element size decreases. On the other hand, when only a translational spring is used (case 1), the solution is not sensitive to the element dimensions; furthermore the error when compared to the analytical result is very small.

One way to remove or reduce the sensitivity of the model to element size is to develop a connection model that does not add stiffness to the rotational DOFs, but instead add an equivalent rotational stiffness to the system using an array of translational springs. Such a connection model is described in the following section and subsequently applied to spot weld modelling.

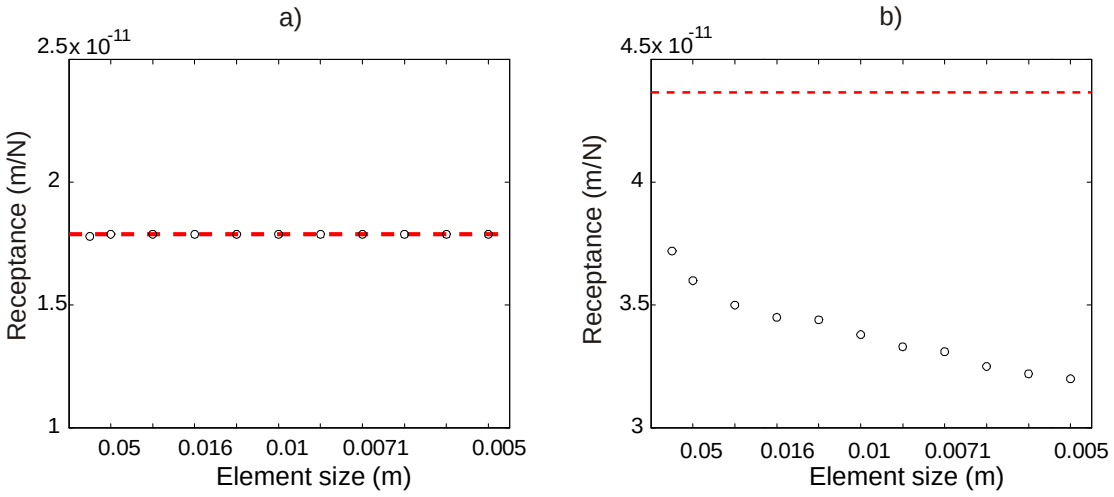

Figure 4.1: Receptance at 0 Hz as a function of element size; a) translational spring, b) rotational spring; ○ Finite Element solution, - - analytical solution.

4.2 Proposed spot weld based on MPC connections with equivalent rotational stiffness.

In this model, the spot weld is assumed to be circular with radius r. In order to add rotational stiffness to the connection, the proposed spot weld model contains N translational vertical springs $(N>2)$ located along the perimeter of the spot weld at angles of $\frac{2\pi p}{N}$ where $p=1,2\cdots N$ (see Figure 4.2). For a required equivalent translational stiffness, $K_{w,eq}$, the translational stiffness of each individual spring

$$K_w = \frac{K_{w,eq}}{N} \tag{4.18}$$

The equivalent rotational stiffness is given by

$$K_{\theta x,eq} = \sum_{j=1}^{N} K_w r^2 \cos^2\left(\frac{2\pi j}{N}\right) \tag{4.19}$$

Applying the identity ($\cos^2 x = 1/2\left(1+\cos\left(2x\right)\right)$), equation (4.19) can be rewritten as

$$K_{\theta x,eq} = \sum_{j=1}^{N} \frac{1}{2} K_w r^2 \left(1 + \cos\left(\frac{4\pi j}{N}\right)\right) = K_w r^2 \left(\frac{1}{2} N + \sum_{j=1}^{N} \frac{1}{2} \cos\left(\frac{4\pi j}{N}\right)\right) \tag{4.20}$$

Given that $\sum_{j=1}^{N} \cos\left(\frac{4\pi j}{N}\right) = 0$,

$$K_{\theta x,eq} = \frac{1}{2} K_w r^2 N \tag{4.21}$$

One can show similarly that the rotational stiffness $K_{\theta,eq} = K_{\theta x,eq}$ is independent of the rotational axis. Considering equation (4.18), we have that

$$K_{\theta,eq} = \frac{1}{2} K_{w,eq} r^2 \tag{4.22}$$

Equation (4.22) shows that $K_{\theta,eq}$ is independent of N. It was also found that even if the x and y axes are rotated an angle θ_{axis}, $K_{\theta,eq}$ is independent of θ_{axis}. for $N \geq 3$. It was also seen on section 3.3 that the computational efficiency of the low rank update method depends on the number of DOFs involved in the connection. Therefore, three springs are recommended in terms of computational efficiency (see Figure 4.2).

The main advantage of this model compared to the simple MPC model in section 2.1 is related to the fact that the new model provides a surface to surface link between components, in doing so the physics of the connection is modelled in a better way and the area of the spot weld is consistent with the spot weld dimensions. Finally $K_{\theta,eq}$ is proportional to the spot weld radius as can be seen in equation (4.22) and not to the element length.

For in-plane vibration springs in the appropriate direction are added in the central position of the weld. This has been proven effective in practice [5], [62]. The local DOFs of the individual springs are attached to the structures using MPCs in the same way as the simple model in section 2.1. The springs can be attached to the same or to

different elements of the structure. Thus not only can the spot weld be located anywhere in the model but it can also join structures with different mesh characteristics as shown in Figure 4.2.

4.3 Experimental validation

The experimental set-up comprised an assembly of two overlapped identical steel plates with free-free boundary conditions and with three spot welds along the overlapped area. This set-up was used previously by Lardeur et al [58]. The spot weld size is 7 mm and the plate thicknesses are 1.96 mm. According to Lardeur [58], this value was chosen because it is thin enough to satisfy thin plate theory conditions and thick enough to reduce effects due to geometrical imperfections. The geometry is shown in Figure 4.3.

The assembly was hung by rubber bands to replicate free boundary conditions. The first plate was excited using an LDS V201 shaker attached at coordinate $(x_i, y_i) = (84\text{mm}, 36\text{mm})$. The input force was measured using a PCB force gauge, type 208C01, screwed to a threaded stud which was glued to the plate using epoxy glue. A 25 mm long stinger was used to connect the force gauge and the shaker in order to minimise the effects of moments transmitted from the shaker.

The response was measured using a PCB accelerometer attached to the second plate at coordinates $(x_1, y_1) = (314\text{mm}, 84\text{mm})$ and $(x_2, y_2) = (236\text{mm}, 185\text{mm})$. A stepped sine signal was input to the shaker with a fine frequency resolution around resonances. The signals from the transducers were acquired by a Data Physics DP240 analyzer and the signls were postprocessed using MATLAB. The test was repeated six times for two different samples. In each case, the plates were dismounted from the experimental set-up and then mounted again.

The natural frequencies f_n are estimated from the measured FRFs using the single DOF circle fitting method [63]. In the frequency range of interest twelve modes were observed: 6 rigid body modes and 6 elastic modes. Only the elastic modes are considered in this study. The measured natural frequencies are given in Table 4-1.

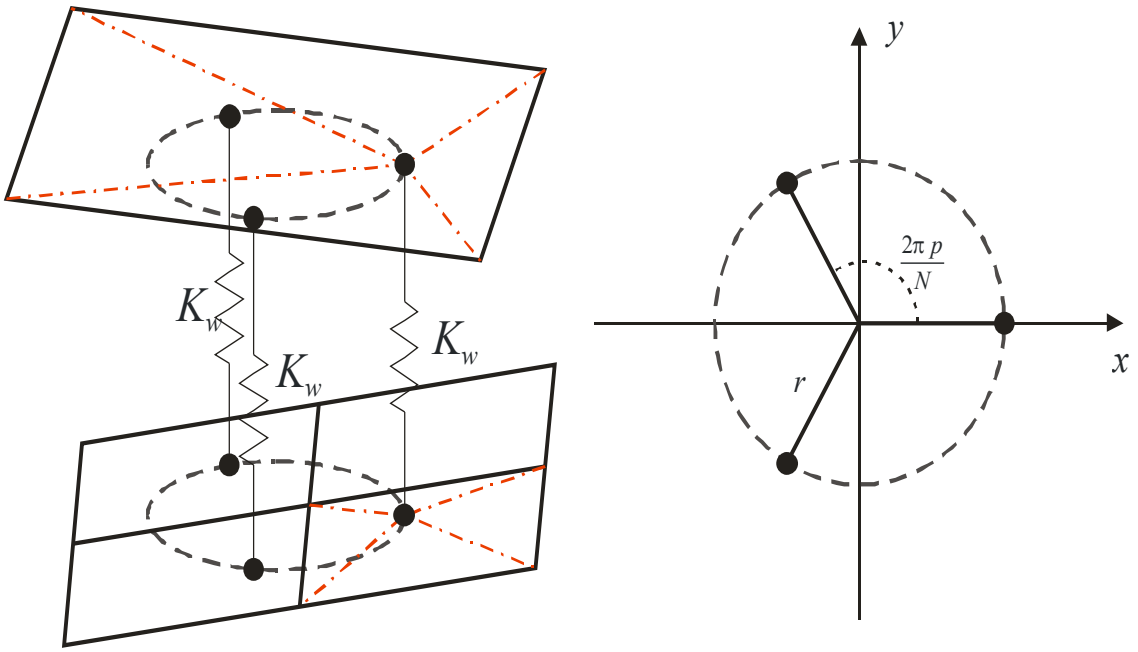

Figure 4.2: Graphical representation of the spot weld model: —— shell elements; -·-·- multipoint constraints; ---- spot weld region.

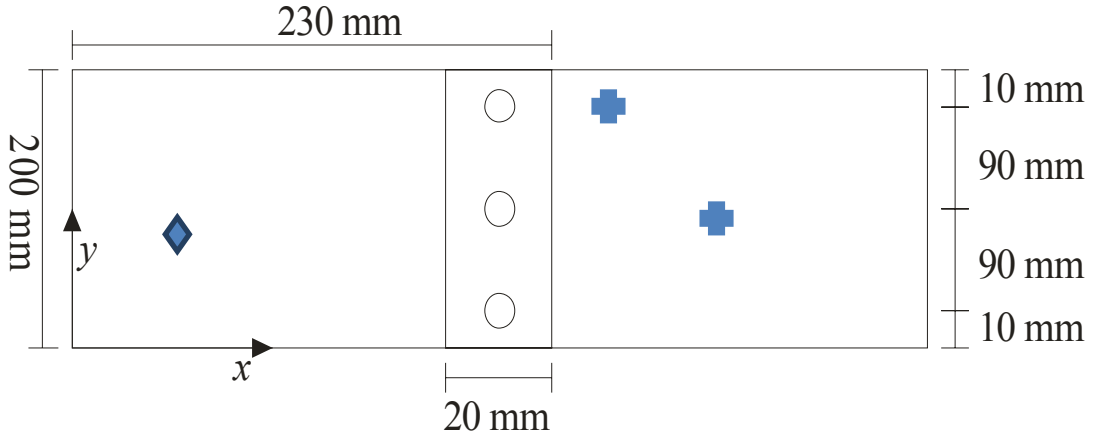

Figure 4.3: Geometric description of the spot welded assembly: ◆ excitation position; ✚ response positions.

	Mean natural frequencies (Hz) and standard deviation (%)											
	mode 1		mode 2		mode 3		mode 4		mode 5		mode 6	
	$\bar{f}_1$	σ_1	$\bar{f}_2$	σ_2	$\bar{f}_3$	σ_3	$\bar{f}_4$	σ_4	$\bar{f}_5$	σ_5	$\bar{f}_6$	σ_6
Assembly 1	52.38	0.07112	82.54	0.03643	154.66	0.00368	164.05	0.00843	272.18	0.02886	289.73	0.01440
Assembly 2	51.96	0.09493	81.98	0.09244	152.29	0.03781	163.95	0.03129	271.16	0.03923	289.95	0.02719

Table 4-1: Measured mean natural frequencies $\bar{f}$ and normalized standard deviation σ of these values.

These results show that the experimental variation of the measured natural frequencies is small between the measurements of the same assembly, while the difference between assemblies is greater but still small. Therefore these values will be used as reference for the numerical model.

4.3.1 Numerical model

The numerical model is shown in Figure 4.3. The plates were modelled using Heterosis elements [28]. The Young's modulus and density were estimated experimentally from beams cut out from the original assemblies. The dimensions of the beams were measured using a vernier calliper and the thickness was measured using a micrometer. The mass was measured using a mechanical balance with 0.01 gram resolution. The dimensions and weight of the beams are in Table 4-2. E is estimated using the measured fundamental frequency ω_{b1} and the analytical formula

$$\omega_{b1}^2 = \frac{EI_b}{\rho A_b}\frac{(k_1 l)^4}{l^4} \tag{4.23}$$

where ρ is the estimated density, l is the measured length. A_b, I_b are the cross section and second moment of area of the beam calculated from the measured dimensions. $(k_1 l)$ is the first non-zero solution to the transcendental equation of beams with free boundary conditions $\left(\cosh(kl)\cos(kl)=1\right)$.

ω_{b1} was estimated using the circle fitting method [63] on the measured FRFs. The FRFs were measured using an impact hammer to excite the beam and the response was measured at the antinodes using a laser vibrometer to avoid mass loading. The beams were hung at the nodal points using elastic bands. The estimated properties are shown in Table 4-3.

l (m)	a (m)	b (m)	ω_{b1} (rad/s)	weight (kg)
0.2	0.02	0.00196	1637	0.062

Table 4-2: Beam measured dimensions and weight.

ρ (kg/m^3)	I_b (m^4)	A_b (m^2)	E (N/m^2)
7908	1.25E-11	3.92E-05	2.15E+11

Table 4-3: Estimeted properties to be used in FE model.

Different element sizes ranging from 0.002 to 0.03 m were utilized in order to calculate the mesh sensitivity and convergence criteria.

The elastic connection was modelled using two models: a simple MPC model as described in section 2.1 and similar to the CWELD model [10] and the model described in section 1.1.4. For the simple model, the stiffnesses values used in all three connections are $K_w = 1\times10^{12}$ N/m and $K_{\theta x} = K_{\theta y} = 1\times10^{4}$ Nm/rad . These values are effectively rigid, i.e. effects of larger stiffness are negligible. When the proposed model is applied, the configuration described in section 4.2 is used, i.e. three translational springs with stiffness of $K_w = 0.33\times10^{12}$ N/m located around a circumference with radius r .

4.3.2 Results

The first six natural frequencies were obtained using the numerical model described previously and then compared to the experimental results. In order to evaluate the accuracy in the predicted natural frequencies with different element sizes the results are presented in Figure 4.4 and Figure 4.5 respectively. The % error when compared to the experimental results and sensitivity is calculated for an element size equal to 10mm, i.e. $s_x = s_y = 10$mm . The results can be seen in Table 4-4. The synthesis of the results is given in Table 4-5.

Both methods underestimate the natural frequencies. It must be emphasised that these models have not been updated in any way: a simple update of the connection properties could lead to more accurate estimates for both models. It can be seen in Table 4-4 that for modes 2,3,4 and 6 both models give similar results, with the proposed spot weld model giving slightly better results, however, the estimated natural frequencies are considerably improved for modes 1 and 5.

The sensitivity to the mesh size and convergence characteristics are considerably improved by using the new model in all modes as shown in Figure 4.4, Figure 4.5 and Table 4-4. On average, the sensitivity is improved almost five times as can be seen in Table 4-5.

Having a high sensitivity to the element size means that changes in the mesh characteristics lead to large changes in the predictions. This problem does not occur when the proposed model is used. Results also show that the simple MPC model does not converge, this model results in assemblies that are too flexible, especially when a small element size is used. On the other hand, when a coarse mesh is used the errors are substantially reduced, although coarse meshes might give inaccurate predictions in practical applications with complex geometries. Even then, the error is greater than that of the new spot weld model.

The lack of convergence and large sensitivity to changes in the element size for the simple MPC model are related to the application of rotational stiffnesses to the DOFs of the plate elements as described in section 4.1.

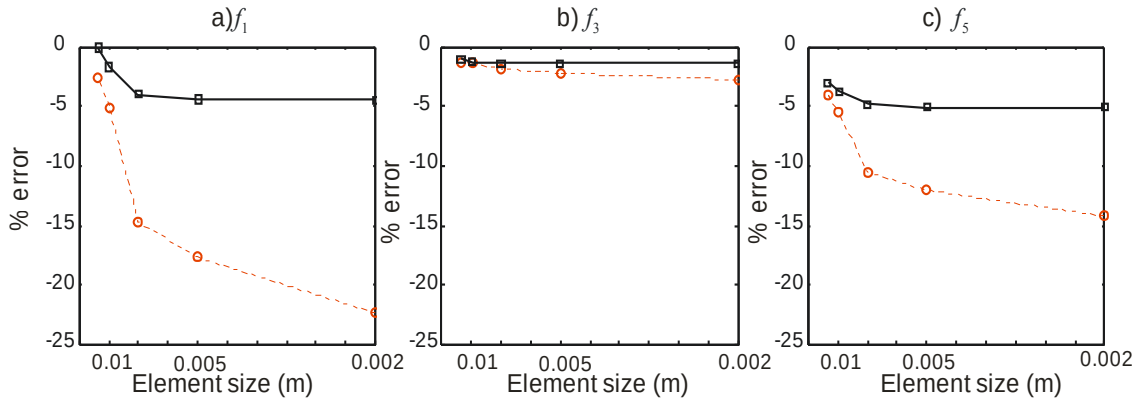

Figure 4.4: Variation of calculated natural frequencies with element size: - - - simple MPC model; —— proposed spot weld model: a) first; b) second; c) third flexural natural frequencies.

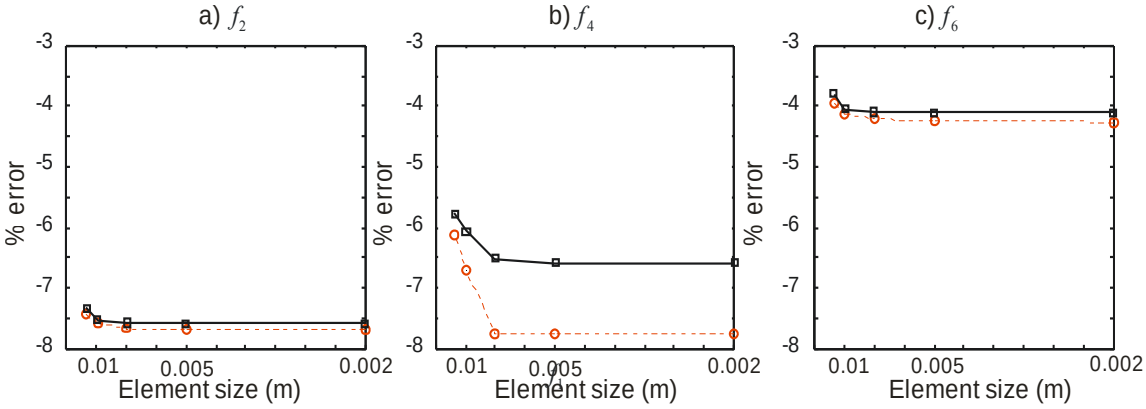

Figure 4.5: Variation of calculated natural frequencies with element size: - - - simple MPC model; —— proposed spot weld model: a) first; b) second; c) third torsional natural frequencies.

	% error natural frequencies		Sensitivity (Hz/m)	
mode number (n)	Simple MPC model	Proposed spot weld model	Simple MPC model	Proposed spot weld model
1	-14.68	-3.98	660.73	133.13
2	-7.66	-7.57	2.97	1.63
3	-1.85	-1.35	97.17	8.17
4	-7.74	-6.51	84.23	44.22
5	-10.53	-4.84	1216.25	224.44
6	-4.22	-4.10	19.08	11.35

Table 4-4: % error in predicted natural frequencies and sensitivity at element size equal to 10 mm.

	% error natural frequencies	Average Sensitivity (Hz/m)	Convergence
Simple MPC model	-7.779	346.7	Not achieved
Proposed spot weld model	-4.724	70.49	8mm

Table 4-5: Summary of results comparing performance of both models.

4.4 Conclusions

In this chapter a new spot weld model is proposed. This model imposes a surface-to-surface connection between two structures using simple spring elements and MPCs, therefore coincident meshes are not required. The application of the new spot-weld model is validated experimentally on a model of two simply supported plates with three spot weld connections. The performance is compared to a simple MPC connection.

It has been shown that when plate elements are based on Mindlin-Reissner plate theory, the stiffnesses in the rotational DOFs depend on the element size in a quadratic way. In addition, when the rotational stiffness of the connection is added to the system, it results in a high sensitivity of the static solution and natural frequencies to the element size. This was demonstrated on an assembly of two simply supported plates with a single connection.

The new model provides a better physical representation of the spot weld and as a result the forces at the connections are distributed over an area imposing a surface to surface link between the structures. This model does not add stiffness to the rotational DOFs, but instead it is composed of an array of three springs distributed along the spot weld circumference that add an equivalent rotational stiffness to the system. The results show that the new spot weld model reduces the sensitivity substantially and improves convergence with different mesh sizes. For the structures considered, convergence is achieved with an 8mm element size compared to a plate thickness of 1.96mm, whilst for the simple MPC model convergence is not achieved. The average sensitivity to element size at 10mm is reduced almost five times from 346.7 Hz/m to 70.49 Hz/m.

5 EXPERIMENTAL VALIDATION

The main objective of this thesis is to predict the vibrational behaviour of built-up structures subject to variations in the location and size of the spot welds. In chapter 3 an efficient method to perform a numerical analysis was presented. This method applies a low rank update theory in the CMS framework. In this chapter this method is validated using experimental results. In addition, the performance of the spot weld model proposed in chapter 4 is compared to a model similar to the CWELD model in Nastran.

A double hat structure, shown in Figure 5.1 was chosen for this purpose. This structure consists of hat section steel plates joined together by spot welds at the flanges. This structure was chosen for the following reasons: (i) it is a simplified representation of the beams used in car bodies. The thickness used is also typical of automotive sheet metal (0.7mm), (ii) the stiffness added due to the contact conditions at the flanges is negligible when compared to the stiffness of the profile and therefore it is not necessary to model the contact conditions in the flanges to obtain accurate predictions, (iv) considering the properties of each spot weld ((x, y) coordinates and radius) as independent variables, having only a few spot welds, fewer samples are necessary in order to predict the variability in the assembly due to variations in the spot weld location and size. Therefore an assembly with only four spot welds was chosen.

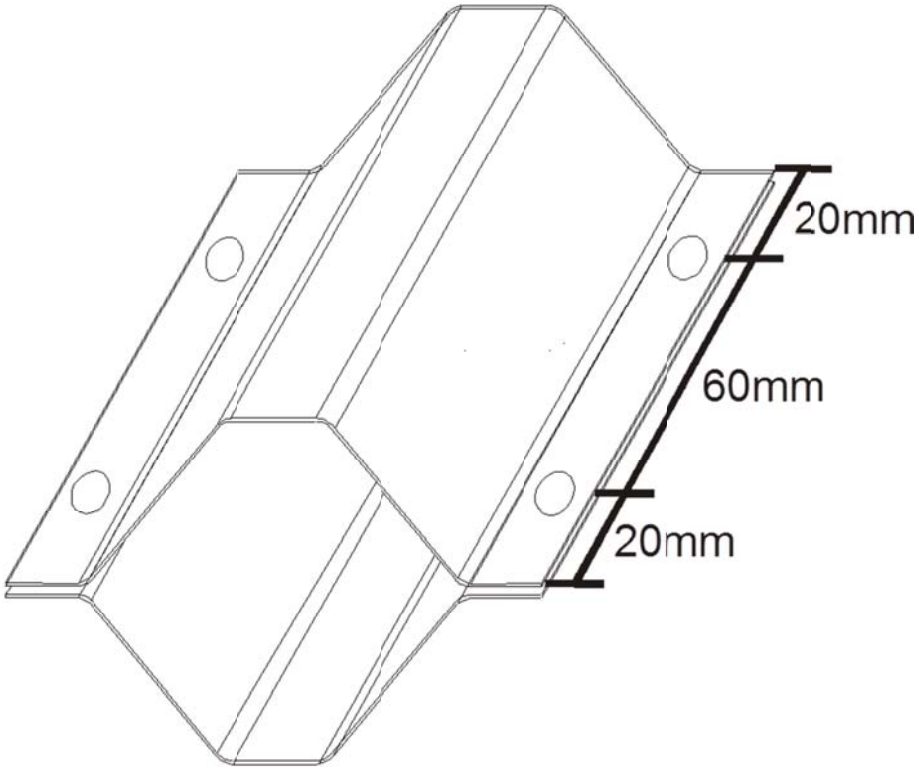

Figure 5.1: Spot welded assembly

In order to isolate the variability due to the spot welding process, it is desirable to minimize the variability of the individual hat section. Therefore the natural frequencies of the separate individual hat section plates were measured and a statistical analysis on the first seven natural frequencies was performed in order to determine the variability in the hat plates. Only a subset of the plates (for which the variability was small) was used for later assembly.

After being welded, the spot weld sizes and locations were measured. The natural frequencies, loss factors and mode shapes were estimated and analysed. Subsequently, the measured damping estimates together with the spot weld size and location were used as inputs for the FE model. Finally the result from the FE model and the experimental modal analysis are compared.

5.1 The hat plates

The hat plates were cut from steel cladding sheets. To manufacture the cladding sheets, flat sheet metal is rolled into the hat profile. Galvanised steel cladding profile 32/1000

was used. The dimensions are shown in Figure 5.2. The hat plates were cut from the full sheet and are 100 mm long, 0.7 mm thick and with flanges 14 mm wide as shown in Figure 5.3.

159 hat plates were fabricated and marked with an identification number.

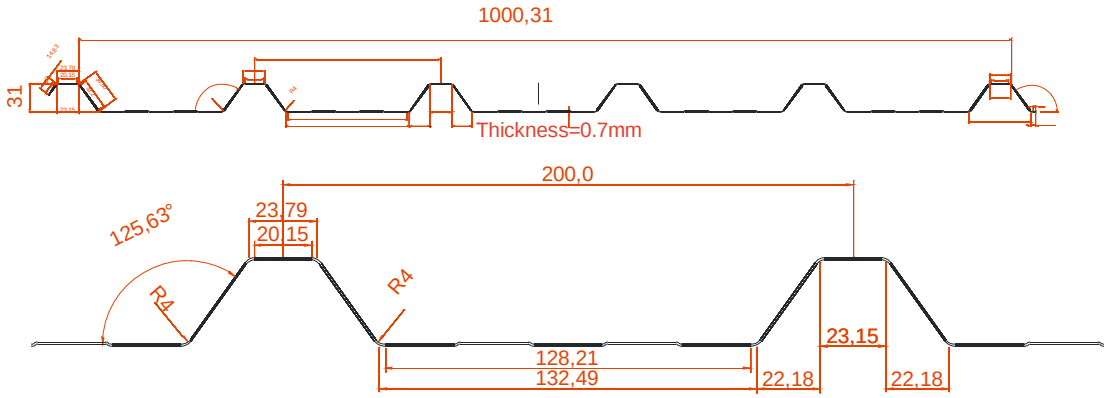

Figure 5.2: Cladding profile 32/1000

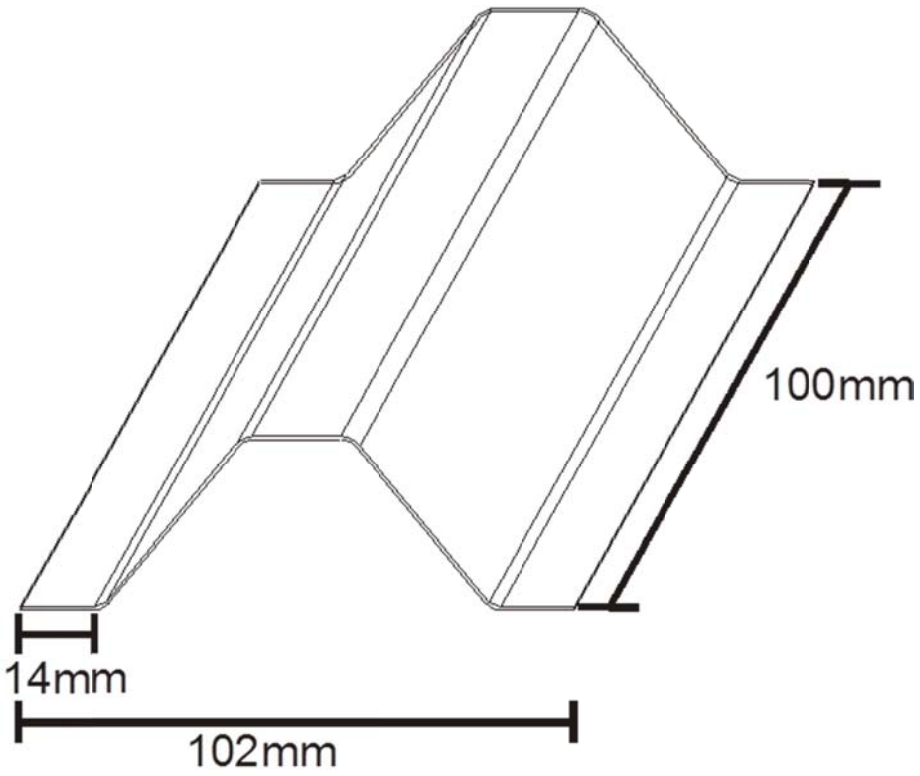

Figure 5.3: Single hat profile

5.1.1 Experimental modal analysis

The experimental modal analysis was carried out for all of the hat plates using a hammer test with fixed accelerometer position and fixed impact location. The structures were tested in free conditions, supported by an elastic band on one edge of the plates (see Figure 5.4).

The FRFs were acquired using a Data Physics DP 730 Dynamic Signal Analyzer. The plate acceleration was measured using a PCB 352C22 accelerometer at a point 5 mm from the midline of the plate and 10 mm from the top edge. The excitation was applied using a PCB 086D80 hammer to strike the plate at the flange of the plate 20 mm from the bottom of the plate and 7 mm from the edge of the plate as shown in Figure 5.4. These positions allow the measurement of all the first seven elastic modes.

In order to acquire the first seven modes, the measurements were taken from 0.1 to 1600 Hz and 3200 frequency lines, hence a frequency resolution of 0.5 Hz and a measurement time of 2 seconds. An average of three measurements was taken for each FRF using the analyser software (signalcalc730) and then exported to MATLAB to perform modal analysis. Figure 5.5 shows a typical input force signal in the time and frequency domain. It can be seen that the spectrum is reasonably flat in the measurement frequency range. Figure 5.6 shows a typical FRF and coherence for these measurements. The coherence is poor at antiresonances due to a low signal to noise ratio in these regions. However, generally it can be judged satisfactory.

In addition to the elastic modes, 6 rigid modes are found below 10 Hz. However their effects on the elastic modes are insignificant. Only the elastic modes are considered in this study.

The experimental natural frequencies were estimated from the measured FRFs using the single DOF circle fitting method [63]. Figure 5.7 illustrates a circle fitted to measured data around a natural frequency. The natural frequencies are estimated as the frequency at which the response is maximum, since damping is in general low, the error generated by this estimation is small.

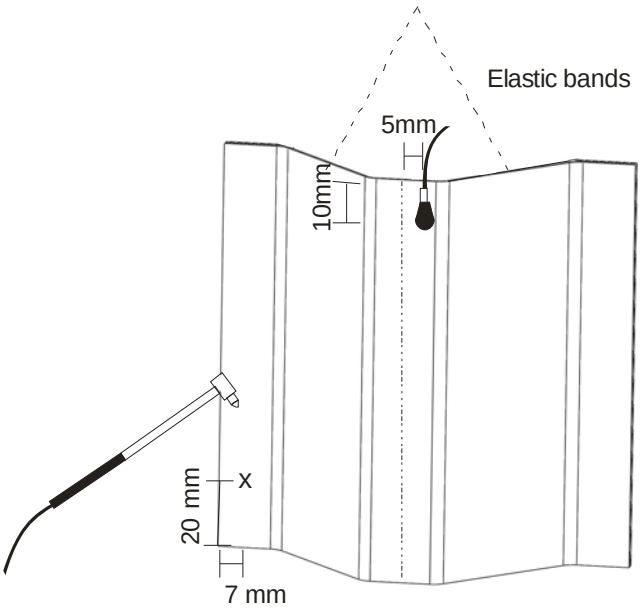

Figure 5.4: Experimental setup for FRF measurement of single hat plates using an impact hammer:

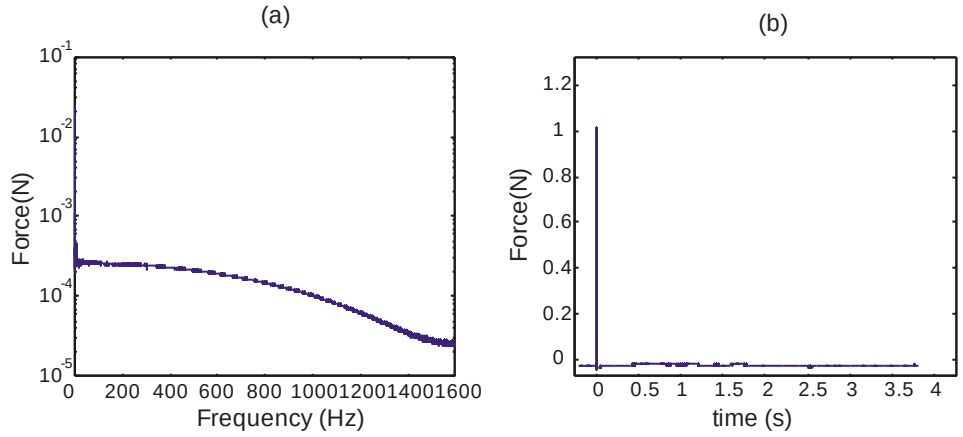

Figure 5.5: Typical force signal in (a) the frequency and (b) the time domains.

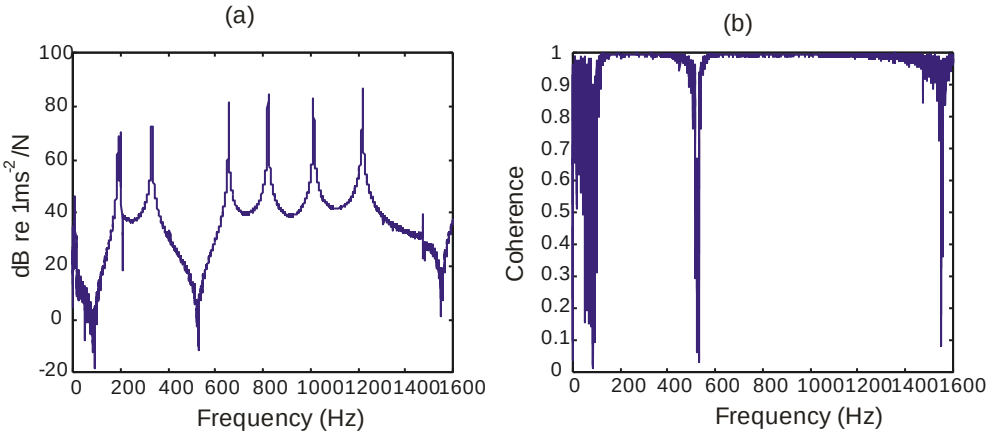

Figure 5.6: Typical (a) FRF and (b) coherence measurements

In order to estimate the modal loss factor, three data points were selected at frequencies greater than the natural frequency and three more points were selected at lower frequencies. These points were used two at a time in order to calculate nine loss factor estimates. The loss factor was estimated as [63]

$$\eta_n = \frac{2(\omega_a - \omega_b)}{\omega_n\left(\tan\left(\theta_a/2\right) - \tan\left(\theta_b/2\right)\right)} \tag{5.1}$$

where ω_a and ω_b are the frequencies of the chosen pair of data points, while θ_a and θ_b are the angles subtended by these data points and the estimated natural frequency as shown in Figure 5.7. Finally the nine values were averaged in order to estimate the modal loss factor. The standard deviation was calculated in order to determine the variability on the estimation. Figure 5.8 shows the mean and standard deviation from the nine loss factor estimates of a typical sample. The modal loss factors are always lower than 3.5×10^{-3}. It can be seen that damping on modes 1 and 2 exhibit larger variability compared to the other modes, however the standard deviation is still small when compared to the mean.

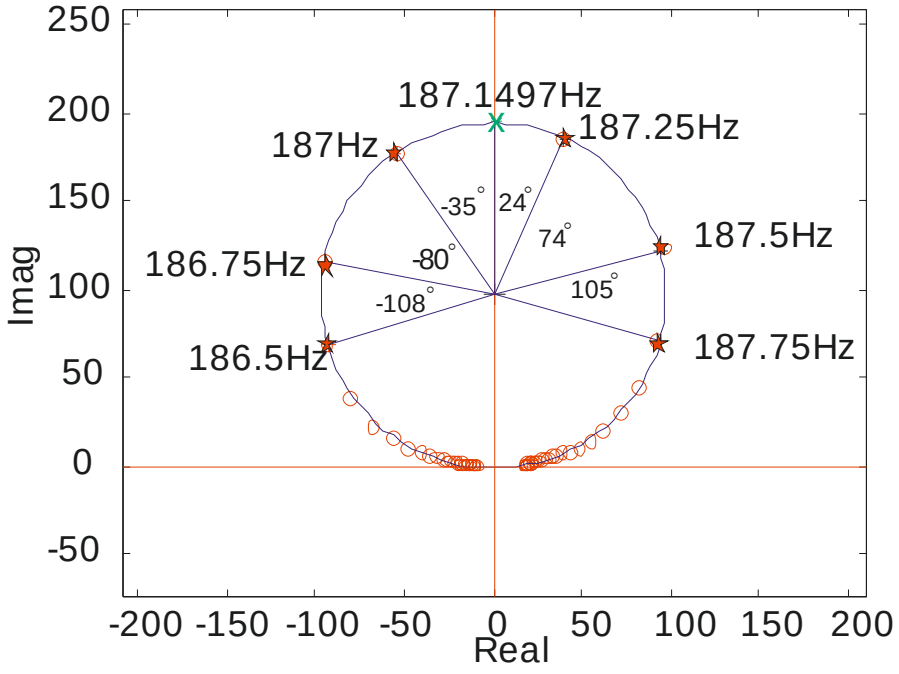

Figure 5.7: Circle fitting for modal analysis: X natural frequency: ○ data points: ★ points selected to measure the modal loss factor.

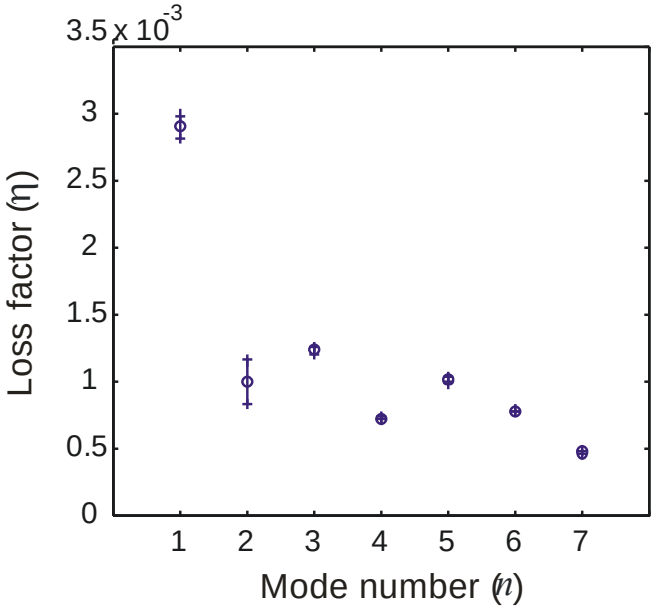

Figure 5.8: Loss factor estimation in typical sample: o mean; + mean+/- standard deviation

5.1.2 Modeshapes of single plate

The mode shapes of the single hat profiles were measured in only three samples. The FRFs were acquired as described in section 5.1.1. except for the impact locations. In this case the impact locations were distributed in a 3 by 3 array on each face of the hat plate as shown in Figure 5.9. The modal constant was calculated as

$$A_n = D_n \omega_n^2 \eta_n \tag{5.2}$$

where D_n is the diameter of the fitted circle in the Nyquist diagram for the nth natural frequency as observed in Figure 5.7.

Figure 5.10 shows an example of the measured mode shapes of the first 7 modes of a single hat plate. The natural frequencies and mode shape description are given in Table 5-1. "Bending 1" refers to a simple 1st bending mode of the side panels while "bending 2" refers to a 1st bending out of phase mode of the side panels.

The results from the other two samples exhibit the same behaviour: modeshapes occur in the same order and the difference between the natural frequencies of the different samples is always lower than 1%.

The first three modes are global modes of the structure and the remaining four modes are bending and torsional modes of the side panels as can be seen in Figure 5.10. These side panels dominate the behaviour of the plate at lower frequencies since they exhibit the largest area of all the five sections and hence have the lowest stiffness.

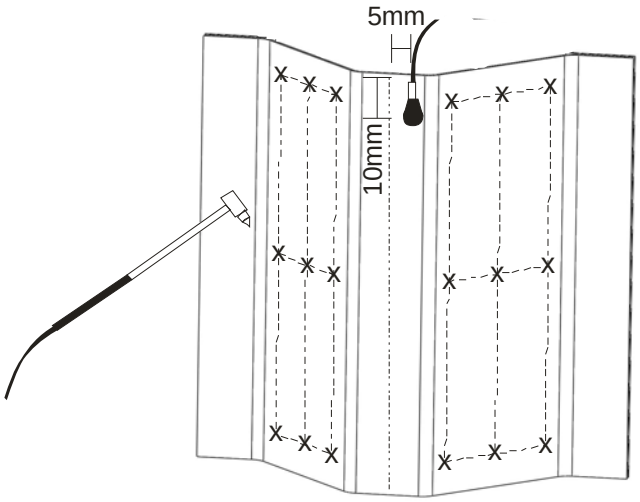

Figure 5.9: Impact positions for the experimental measurement of the single hat profiles mode shapes.

Mode number (n)	f_n (Hz)	Modeshape description
1	190.06	Flapping
2	203.69	1st torsion
3	331.33	1st bending in the XY plane
4	655.61	Side panels bending 1 -out of phase-
5	820.17	Side panels bending 2 -out of phase-
6	1015.2	Side panels bending 1 -in phase-
7	1222.5	Side panels bending 2 -in phase-

Table 5-1: Single hat profiles mode shape description and mean natural frequency

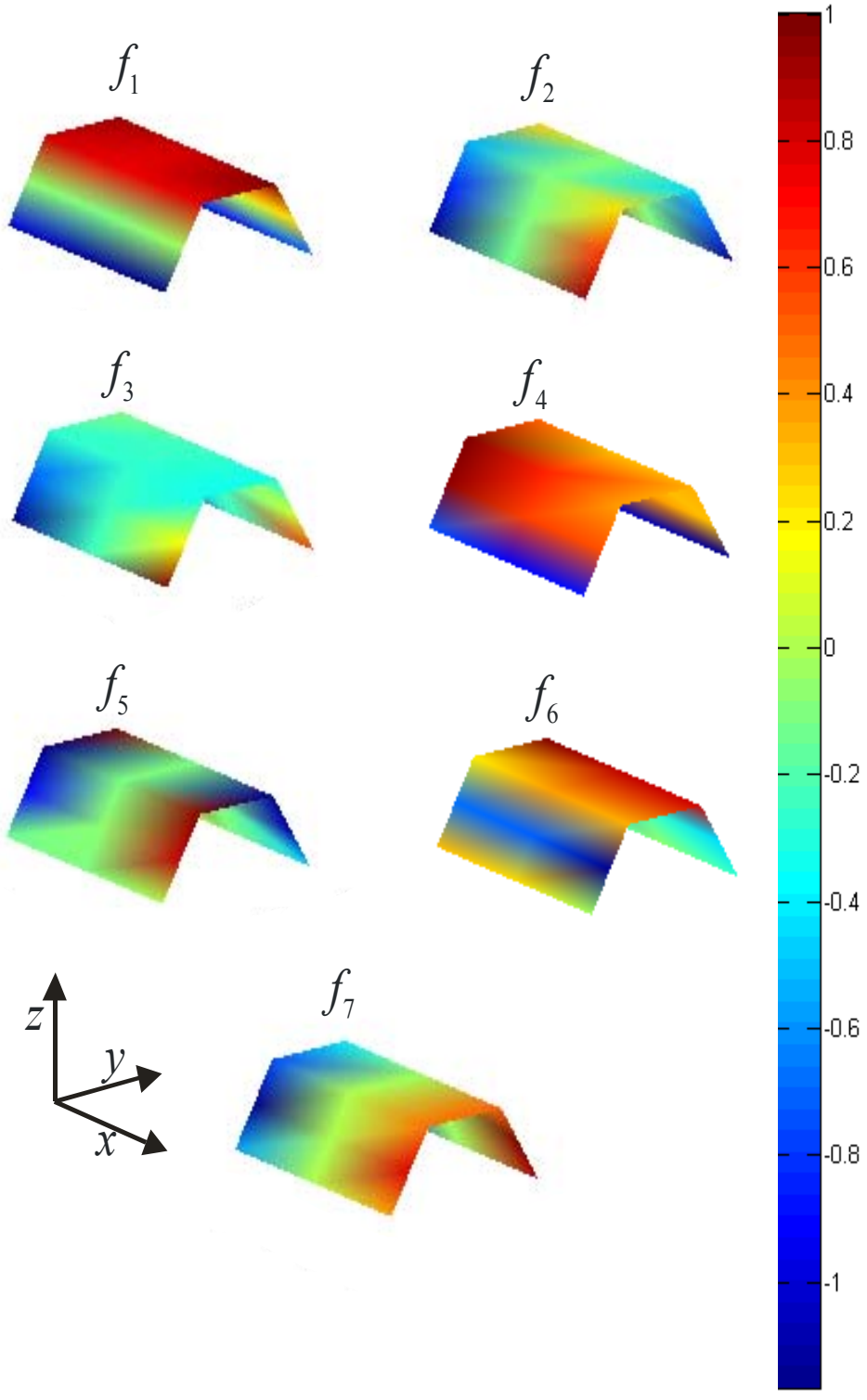

Figure 5.10: Measured modeshapes of a single plate.

5.1.3 Results

The mean and standard deviation for the estimated natural frequencies and loss factors for all 159 plates are shown in Table 5-2 and Figure 5.11. In general the dispersion of the natural frequencies between samples is small and always between 1~ 2 % of the mean value. The estimated loss factors show values of approximately 1×10^{-3} in all modes except modes 1 and 3, which interestingly also exhibit the largest standard deviation as shown in Figure 5.11. The reasons for this behaviour are unknown; it is believed that there might be repeatability issues between samples. In any case, the modal loss factors are small.

mode number (n)	1	2	3	4	5	6	7
$\overline{f}_n$ (Hz)	189.2	203.1	329.0	657.1	821.2	1018	1224
σ_{f_n} (Hz)	2.33	3.06	5.39	7.22	8.39	18.76	20.87
$\overline{\eta}_n$	4.59E-03	9.17E-04	4.24E-03	8.06E-04	1.08E-03	8.02E-04	5.59E-04
σ_{η_n}	1.88E-03	3.21E-04	2.70E-03	1.28E-04	3.07E-04	5.38E-05	9.04E-05

Table 5-2: Mean and normalized standard deviation of natural frequencies and loss factor.

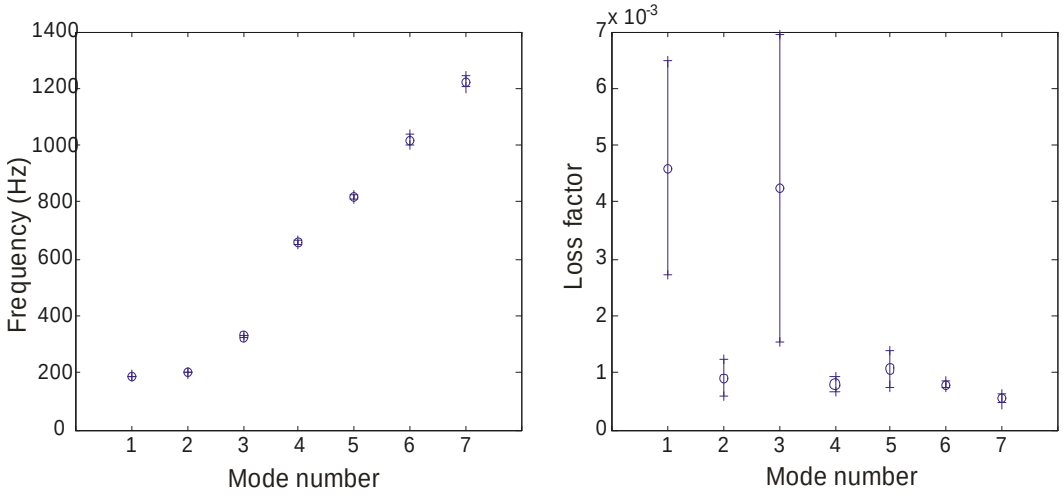

Figure 5.11: Natural frequencies and loss factor statistics : o mean; + mean+/- standard deviation.

5.1.4 Statistical analysis

In this section a statistical analysis of the first seven natural frequencies is presented in terms of the normalized error

$$\varepsilon_n = \frac{\omega_n^{\,2} - \bar{\omega}_n^{\,2}}{\bar{\omega}_n^{\,2}} \tag{5.3}$$

ω^2 was chosen because ε_n is likely to be proportional to the stiffness. The histograms are shown and statistics (mean, standard deviation, skew and kurtosis) are calculated and examined. Finally, in order to test the goodness-of-fit of the response distributions to a normal distribution a χ^2 test is carried out.

The skewness of a random variable is the third moment, normally interpreted as a measure of the asymmetry of a probability distribution [64]. The skew can be positive or negative; a negative skew indicates that the tail on the left side of the PDF is longer than the right side and vice versa. In a normal distribution, the skew is equal to zero. The kurtosis of a random variable is the fourth moment. Kurtosis measures how heavy the tails of the PDF are; higher kurtosis means bigger tails. The kurtosis of a normal distribution is 3.

The χ^2 goodness-of-fit test is based on a comparison between observed frequencies of categories and corresponding expected frequencies under the hypothesis to be tested [65–67], in this case compared to a normal distribution. The χ^2 test is conducted on classified (binned) data and outlying bins are summed to ensure at least five counts in each; this reduced the skewing effect of out-lying results. There is not a clear constraint regarding the minimum size of the sample in order to obtain a valid answer, as an approximation it has been found that the sample should be at least four or five times the number of cells, k [65].

The computed χ^2 statistic has the value of 0 for a perfect fit and is large when the fit is bad. The null hypothesis is therefore rejected if $\chi^2 > \Upsilon$, where Υ is a constant taken

from the χ^2 distribution with α significance level and $k-r-1$ degrees of freedom, where r is the number of estimated parameter. In this case, $r=2$, i.e. mean and standard deviation. The significance value indicates the probability of obtaining those or more extreme results [65] , which means that a higher significance level leads to a more rigorous test.

Figure 5.12 shows the histograms of the first seven natural frequencies when compared to normal distribution. Table 5-3 shows the skew, kurtosis and the χ^2 statistic results. From examination of the χ^2 values in this table, one cannot reject the hypothesis that the first, third, fourth, fifth, sixth and seventh modal frequencies fit into a normal distribution.

It can be seen in Table 5-3 that the skew and kurtosis values of all of the ε_n are close to the values of a normal distribution, 0 and 3 respectively. Conversely, for the second mode the kurtosis value is the closest to 3 and the skew value is the second closest to 0 and yet is the only modal frequency in which the hypothesis can be rejected. The normal distribution can be rejected as a likely fit for the distribution of the second natural frequency, probably due to the high number of samples close to the mean with an uneven spread as can be observed in Figure 5.12.

mode number (n)	1	2	3	4	5	6	7
σ_n	0.0247	0.0300	0.0327	0.0220	0.0205	0.0371	0.0343
Skew	0.562	-0.229	-0.058	0.478	0.501	0.692	0.699
Kurtosis	3.883	3.091	3.204	3.862	3.918	4.221	4.304
k	9	9	9	9	9	9	9
χ^2	9.015	13.687	4.620	6.441	2.880	6.896	3.615
Υ	10.645	10.645	10.645	10.645	10.645	10.645	10.645

Table 5-3: Skew, Kurtosis and χ^2 probability results for goodness-of-fit tests of ε_n.

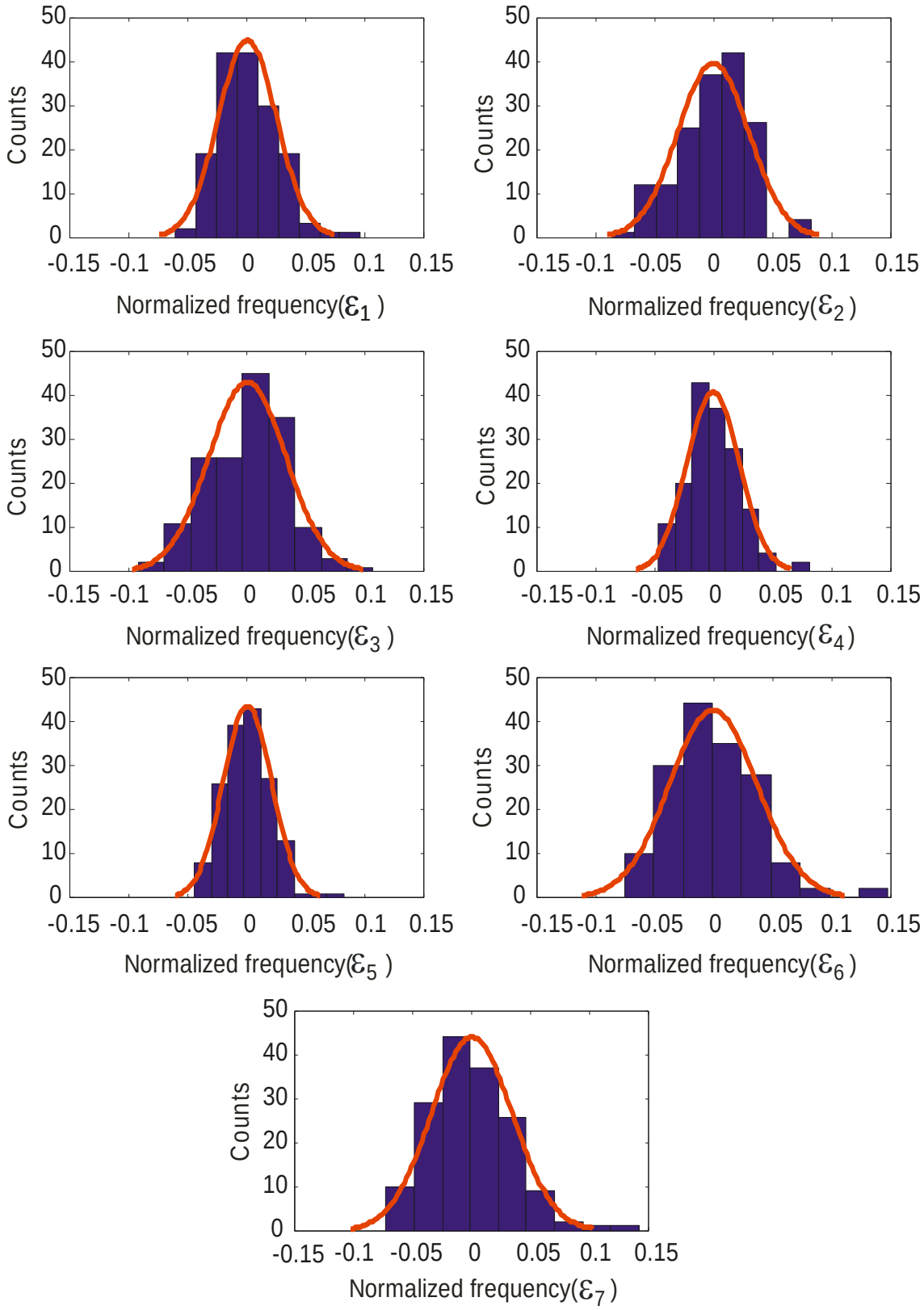

Figure 5.12: Distribution of the first seven natural frequencies (single profiles): Experimental data; Gaussian distribution.

5.1.5 Correlation coefficients

In order to measure the level of correlation between modes, the Pearson product-moment correlation coefficient between ε_l and ε_m

$$r_{l,m} = \frac{\sum_{i=1}^{N}\left(\varepsilon_{l,i} - \overline{\varepsilon}_l\right)\left(\varepsilon_{m,i} - \overline{\varepsilon}_m\right)}{\sqrt{\sum_{i=1}^{N}\left(\varepsilon_{l,i} - \overline{\varepsilon}_l\right)^2}\sqrt{\sum_{i=1}^{n}\left(\varepsilon_{m,i} - \overline{\varepsilon}_m\right)^2}} \tag{5.4}$$

is calculated [68], where i is the sample number, and N is the total number of samples, $\overline{\varepsilon}_l, \overline{\varepsilon}_m$ are the mean normalized error of modes l and m respectively and $\varepsilon_{l,i}, \varepsilon_{m,i}$ are the normalized errors of modes l and m and sample i. $r_{l,m}$ is a measure of the correlation between random variables ε_l and ε_m, giving a value between +1 and -1 inclusive. When $r_{l,m} = 1$ or $r_{l,m} = -1$ then ε_l and ε_m are perfectly correlated, when $r_{l,m} = 0$, ε_l and ε_m are completely uncorrelated. Table 5-4 shows the correlation coefficients between the natural frequencies. Examples of a strong correlation, $r_{1,5} = 0.956$, weak correlation, $r_{1,2} = 0.497$, and a moderate correlation, $r_{1,3} = 0.718$, are shown in Figure 5.13.

Modes 1,4,5,6 and 7 are strongly correlated between each other since all of them depend on the deflection of the side panels. Modes 2 and 3 are modes related to the deflection of the structure in different directions (torsion and bending in the XY plane); hence the correlation between these modes and modes 1,4,5,6 and 7 is weak. However, they are well correlated between each other.

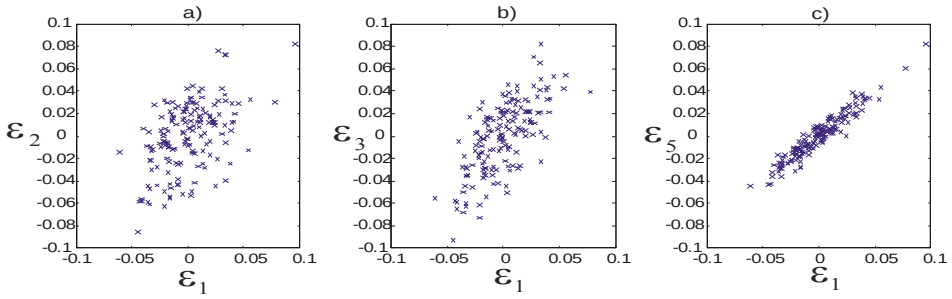

Figure 5.13: Dispersion plots: a) modes 1 and 2, $r_{1,2} = 0.497$; b) modes 1 and 3, $r_{1,3} = 0.718$; c) modes 1 and 5, $r_{1,5} = 0.956$.

n	1	2	3	4	5	6	7
1	-	0.497	0.718	0.875	0.956	0.933	0.930
2	0.497	-	0.900	0.573	0.638	0.513	0.571
3	0.718	0.900	-	0.611	0.765	0.664	0.701
4	0.875	0.573	0.611	-	0.932	0.914	0.919
5	0.956	0.638	0.765	0.932	-	0.931	0.956
6	0.933	0.513	0.664	0.914	0.931	-	0.989
7	0.930	0.571	0.701	0.919	0.956	0.989	-

Table 5-4: Correlation coefficients between ε_n

5.2 The assembled structures

The hat profiles studied in the previous section were assembled using four spot welds as shown in Figure 5.1. A manual spot welder mounted in a bench vice was used to weld the hat plates together. The nominal spot weld diameter depends on the electrode diameter and in this case is equal to 4mm. The spot weld locations were marked by hand using a linear length gauge at the nominal positions shown in Figure 5.1. In order to assure the alignment between the plates at the time of assembly an insert was designed, the profile and the manufactured insert can be observed in Figure 5.14.

In order to focus on variability in the spot welds and to minimize the variability in the assembled structures that arises from variability in the unassembled components, only single plates for which

$$|\varepsilon_n| \leq 0.04 \text{ where } n = 1 \text{ to } 7 \tag{5.5}$$

and

$$\sqrt{\sum_{n=1}^{7} \varepsilon_n^{\,2}} \leq 0.07 \tag{5.6}$$

were used and the remainder were rejected. This means that not only those plates which had variations greater that 4% for any eigenvalue were discarded, but also those plates that exhibit consistently large errors for all eigenvalues. Given these conditions, 108 of the 159 manufactured single plates were retained and were assembled to give 54 spot welded assemblies.

After assembly, the locations of the spot welds at each of the assemblies were measured as well as the natural frequencies of all 54 assemblies. Finally the mode shapes of three samples were measured.

5.2.1 Measurement of spot weld size and location

In order to measure the location and size of the four spot welds for each of the 54 assemblies, a picture was taken using a digital camera. The picture was imported into MATLAB and eight points at the perimeter of the spot welds were selected using the command *ginput*. The spot weld centre and diameter were calculated using the circle fit MATLAB routine applied in the modal analysis. The dimensions were calibrated using two plastic rulers as shown in Figure 5.15

In order to ensure that the pictures were taken from the same position repeatedly, the assemblies are placed in a jig aligned against a wall, with the camera mounted in a tripod facing downwards as shown in Figure 5.16. The pictures were taken using the camera self timer in order to avoid movement that might be induced by manual operation.

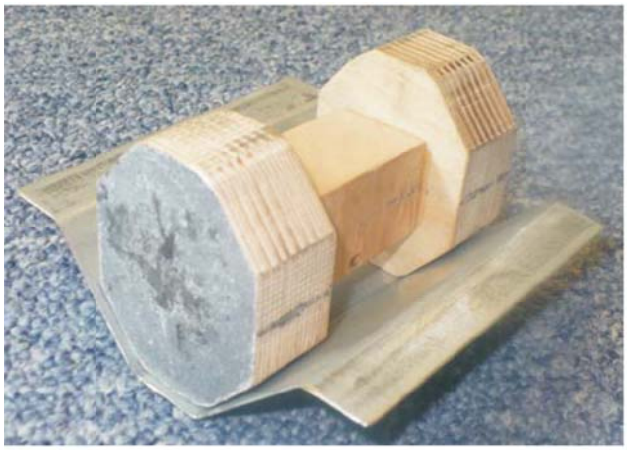

Figure 5.14: Insert used to assure alignment between profiles.

After every 5 samples were photographed, sample number 1 was photographed again in order to assess repeatability. The maximum error between all measurements taken from sample 1 was less that 0.3 mm. Figure 5.17 (a) shows the results of all measurements on sample 1.

Figure 5.17 (b) shows the measured spot weld positions from all 54 samples. It can be seen that the variability of the location of the spot welds are similar for all four locations.

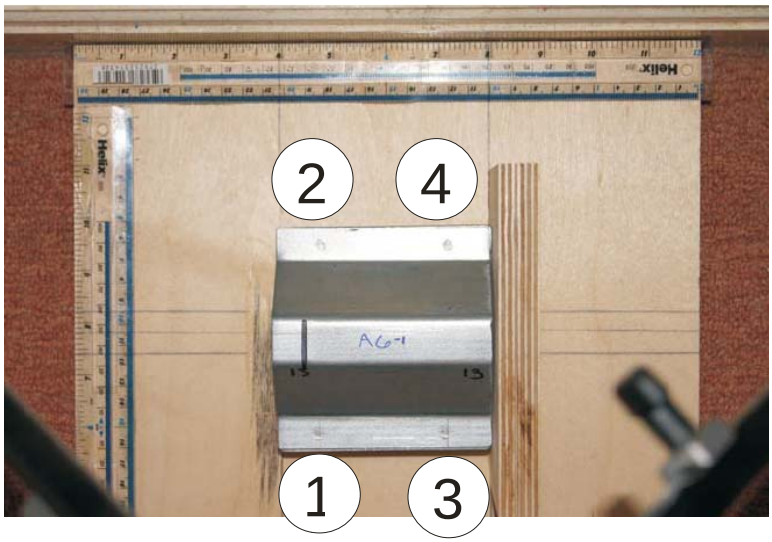

Figure 5.15: Photograph sample and weld numbers.

Figure 5.16: Fixture and arrangement used to take the sample pictures.

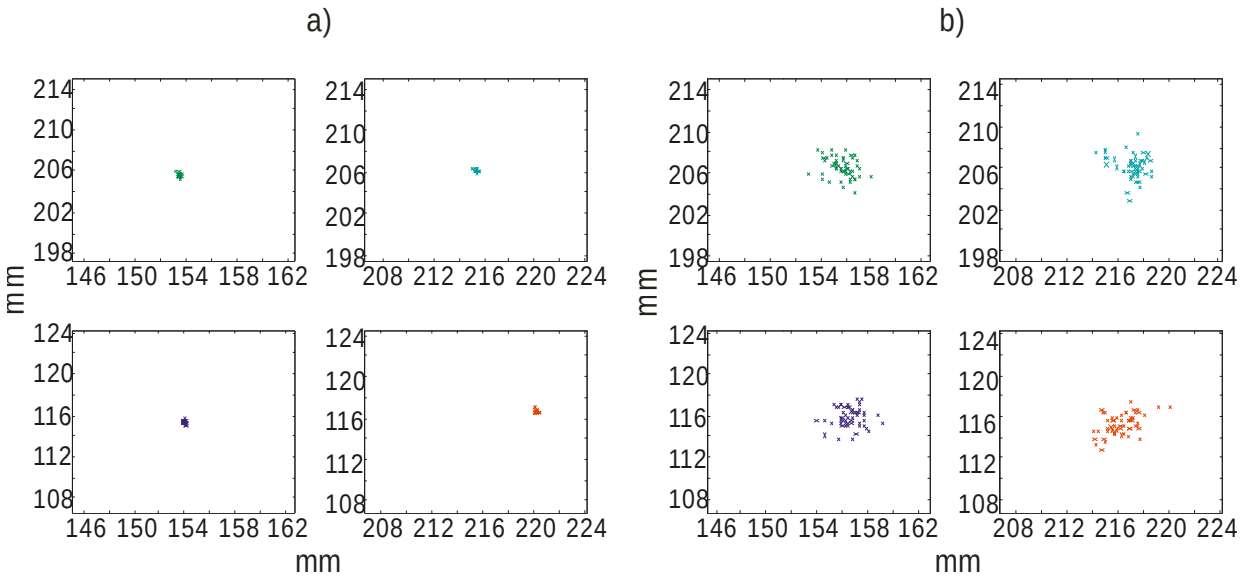

Figure 5.17: Measured spot weld positions: a) sample 1 measurements; b) full ensemble.

5.2.1.1 Analysis of spot weld location

The coordinates (x_s, y_s) of each spot weld were analysed in terms of its deviation from the mean i.e.

$$\Delta x_s = x_s - \overline{x}_s \text{ and } \Delta y_s = y_s - \overline{y}_s \tag{5.7}$$

where $s = 1,2,3,4$ is the spot weld number as shown in Figure 5.15. The correlation coefficients between Δx_s and Δy_s are shown in Table 5-5. The correlation coefficients

between these variables were calculated using equation (5.4). The correlation between the spot weld coordinates is low in general, which means that these variables can be treated as independent. Furthermore, the lack of correlation indicates us that systematic errors in the measurements are low, i.e. translations and/or rotations of the sample when the pictures are taken. The strongest correlation is between Δy_2 and Δy_4, the vertical coordinates of spot weld 2 and 4 are correlated due to the manufacturing process, Δy_1 and Δy_3 are correlated in the same way.

Figure 5.19 shows the histograms of the spot weld coordinates together with normal distributions. The standard deviation, skew and kurtosis were calculated for the eight spot weld coordinates. The results are summarized in Table 5-6. Also the χ^2 goodness-of-fit test was performed.

When χ^2 is compared to Υ in Table 5-6 it can be seen that Δx_4 is the only coordinate for which the hypothesis that the spot weld coordinates come from a normal distribution can be rejected. Δx_4 exhibits the highest skew value and its kurtosis is not close to 3. In Figure 5.19 it can be seen that Δx_4 is clearly skewed to the right and there are a high number of counts at the left end.

	Δx_1	Δy_1	Δx_2	Δy_2	Δx_3	Δy_3	Δx_4	Δy_4
Δx_1	1.000	-0.029	-0.109	-0.016	0.431	0.286	-0.239	0.070
Δy_1	-0.029	1.000	0.056	-0.339	0.031	0.435	-0.050	-0.355
Δx_2	-0.109	0.056	1.000	-0.223	-0.513	-0.195	0.582	-0.256
Δy_2	-0.016	-0.339	-0.223	1.000	-0.128	-0.447	0.026	0.634
Δx_3	0.431	0.031	-0.513	-0.128	1.000	0.530	-0.424	0.062
Δy_3	0.286	0.435	-0.195	-0.447	0.530	1.000	-0.393	-0.176
Δx_4	-0.239	-0.050	0.582	0.026	-0.424	-0.393	1.000	-0.043
Δy_4	0.070	-0.355	-0.256	0.634	0.062	-0.176	-0.043	1.000

Table 5-5: Correlation coefficients between spot weld coordinates.

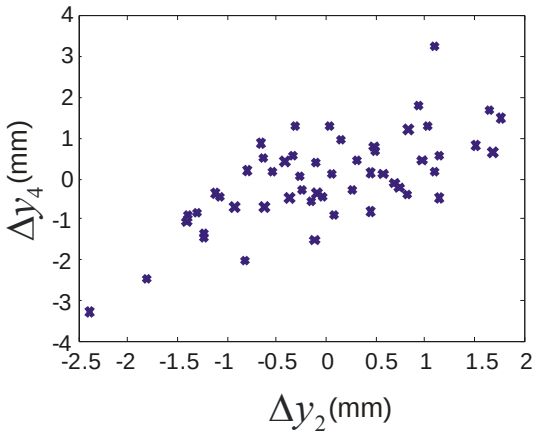

Figure 5.18: Dispersion plot between Δy_2 and Δy_4.

	Δx_1	Δy_1	Δx_2	Δy_2	Δx_3	Δy_3	Δx_4	Δy_4
σ	0.869	0.912	0.895	0.978	1.254	1.009	0.769	1.073
Skew	-0.0943	-0.0824	-0.2696	-0.0132	0.2106	-0.1088	-0.8594	0.0167
Kurtosis	3.63	2.45	2.91	3.23	3.75	2.28	4.13	4.22
k	6	6	6	6	6	6	6	6
χ^2	4.783	2.293	0.458	1.874	4.300	1.899	8.302	3.730
Υ	6.250	6.250	6.250	6.250	6.250	6.250	6.250	6.250

Table 5-6: Standard deviation, skew, kurtosis and χ^2 probability results for goodness-of-fit tests of spot weld coordinates.

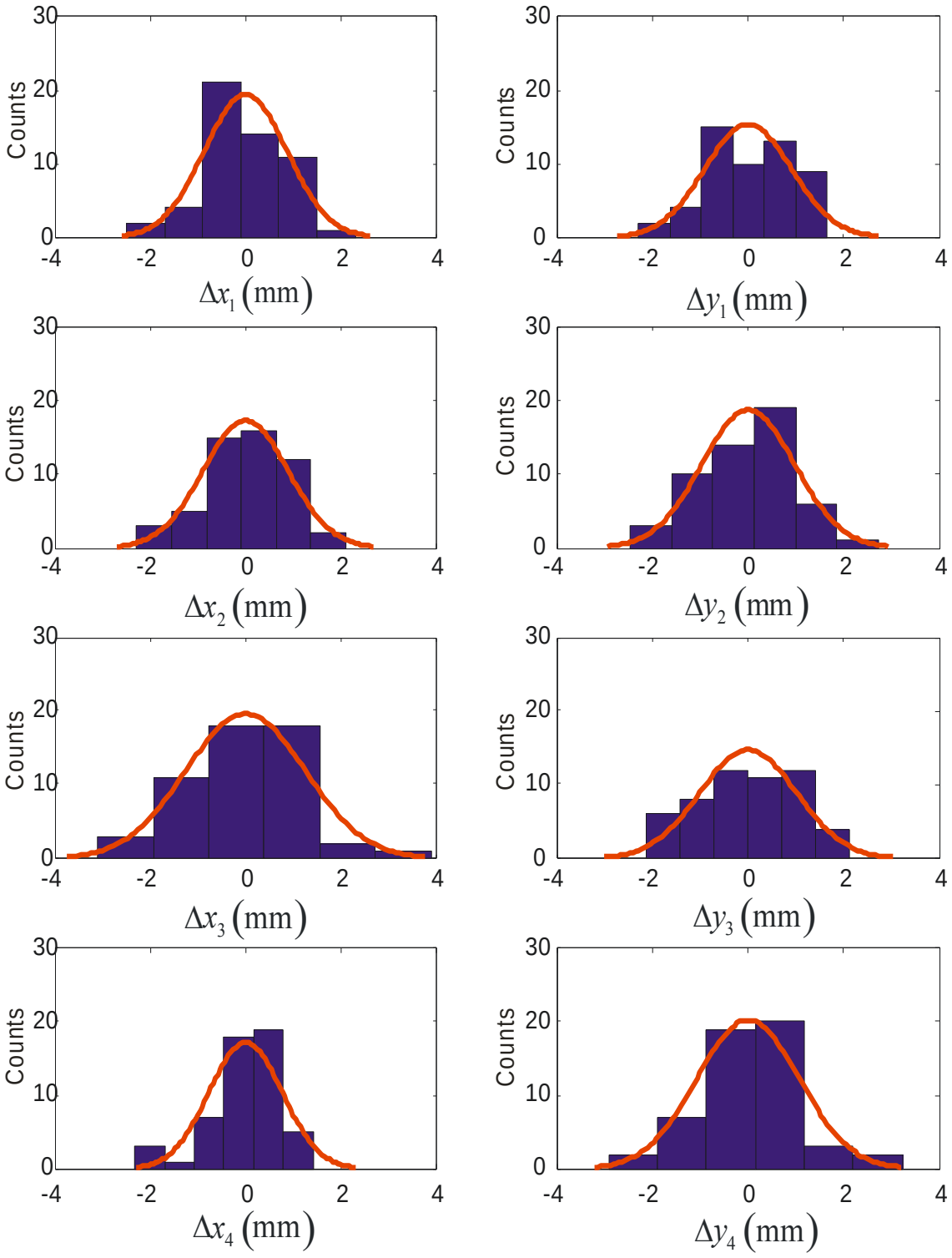

Figure 5.19: Distribution of the spot weld coordinates: Experimental data; Gaussian distribution

5.2.1.2 Spot weld size analysis.

The spot weld size depends on the electrode size and the time of flow of the electrical current, which is a parameter that is set in the spot welding equipment and kept fixed during spot welding.

The spot weld diameter was analysed as a single random variable since the diameter of the spot weld does not depend on the spot weld position. Again the σ, skew, kurtosis are calculated and χ^2 test performed, the results can be observed in Table 5-7.

It can be seen that the hypothesis that the spot weld diameter distribution fits a normal distribution can be rejected. The hypothesis is rejected especially for the high kurtosis value of the experimental data. This can also be observed in Figure 5.20, where the peak is much narrower compared to the normal distribution. The data from the analysis of the position and location of the spot weld will be used as an input for the FE analysis in section 5.4.1.

	Mean	σ	Skew	kurtosis	k	χ^2	Υ
Spot weld diameter	3.63	0.24	-0.675	12.12	22	105.68	27.20

Table 5-7: μ, σ, Skew, Kurtosis and χ^2 probability results for goodness-of-fit tests of the spot weld diameter.

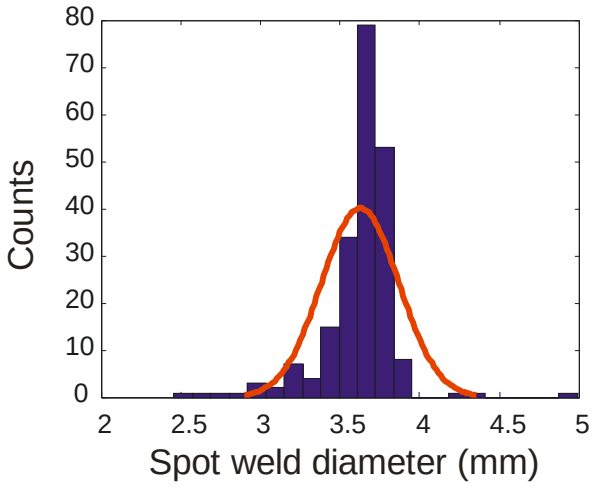

Figure 5.20: Histogram of spot weld diameter: Experimental data; Gaussian distribution.

5.2.2 Experimental modal analysis

The experimental modal analysis was carried out in the same way as with the single hat plates; using a hammer test with fixed accelerometer and impact location. Except that in this case the transfer functions were measured from hat plate to hat plate as shown in Figure 5.21. The 54 structures were tested in vertical free-free conditions supported by an elastic band on one edge of the plates.

The FRFs were acquired using the same equipment as in the single hat plate structures: Data Physics DP 730 Dynamic Signal Analyzer, PCB 352C22 accelerometer and a PCB 086D80 impact hammer. The accelerometer and impact positions are shown in Figure 5.21. The positions were decided based on the mode shapes from an earlier FE analysis. Using this configuration, the first seven elastic modes can be measured and the mass loading effects are minimised.

Again, the shape of the input signal was verified in the time and frequency domain. Figure 5.22 shows a typical input force signal in the time and frequency domain. In general, the spectrum is reasonably flat in the frequency range of the measurement.

The coherence was also verified. Since the transfer function is measured from one plate to the other, the coherence is poor at low frequencies and at antiresonances, where the

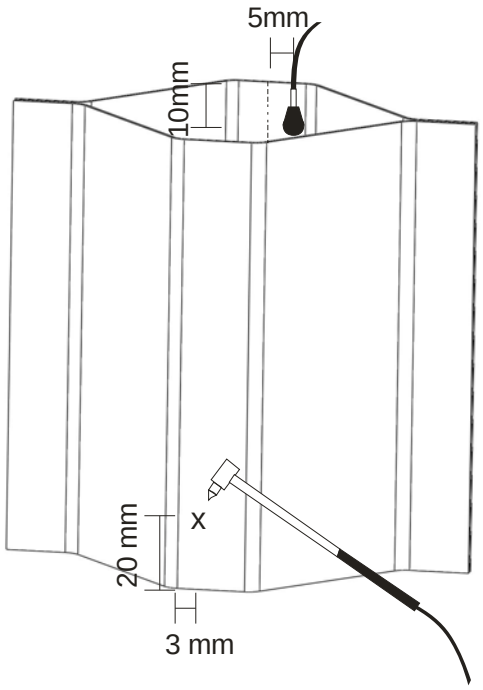

Figure 5.21: Experimental setup for FRF measurements of spot welded assemblies using impact hammer.

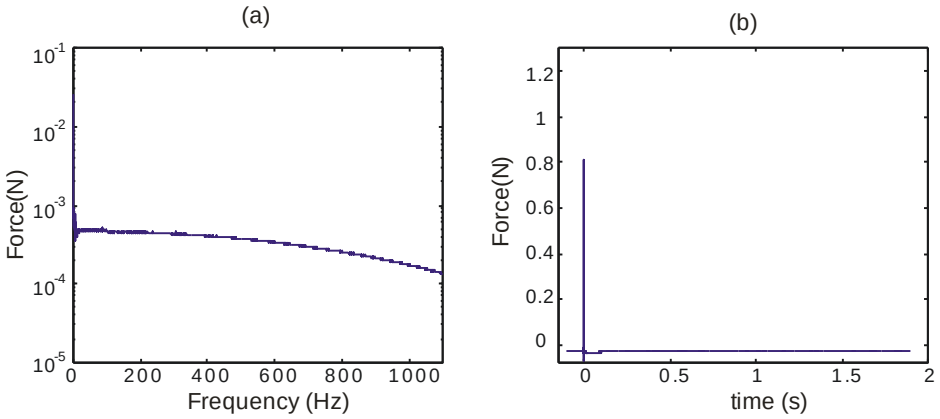

Figure 5.22: Typical force signal in the frequency and time domain.

level of the signal to noise ratio is low. However, in the frequency range of interest the coherence is close to one as can be observed in Figure 5.23.

In the frequency range of interest (up to 1100 Hz), seven elastic modes can be found as shown in Figure 5.23. The experimental natural frequencies and loss factors are estimated using the circle fitting method [63] in the same way as in section 5.1.1. The maximum response in the fitted circle is assumed to be ω_n and η_n is calculated as the

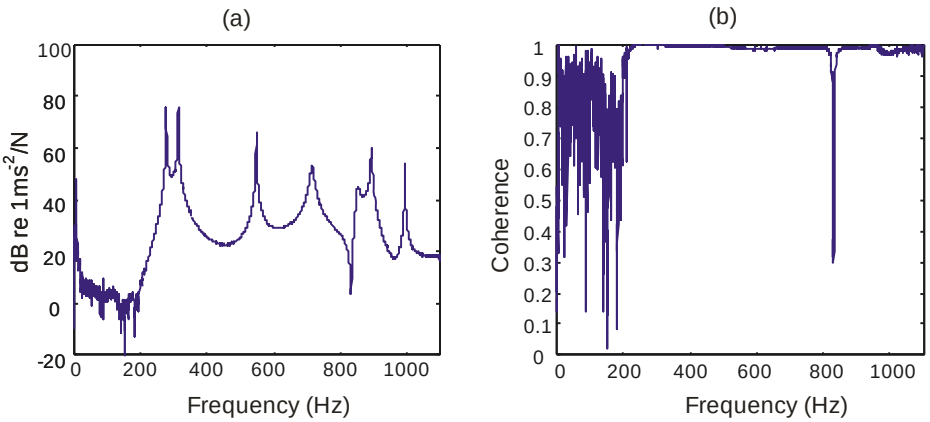

Figure 5.23:Typical FRF and coherence measurements (η).

average of nine η_n estimates from six data points; three data points to the right of ω_n and three more points to the left of ω_n. Each of η_n are estimated using equation (5.1).

Figure 5.24 show the mean and standard deviation from the nine estimates used to calculate the loss factors. The loss factors are in general higher compared to the estimates of the single plates in Figure 5.8, where the maximum η_n is a third of the maximum η_n estimated in the assembled structures. Some of the samples had a maximum $\eta_n \approx 0.005-0.007$ as in Figure 5.24 (a) and some of them had a maximum $\eta_n \approx 0.009-0.011$ as in Figure 5.24 (b). Only in some cases the loss factor exhibits a larger standard deviation as can be observed in η_5 and η_6 in Figure 5.24 (b), however it is still small and the mean can be considered as an adequate damping estimate.

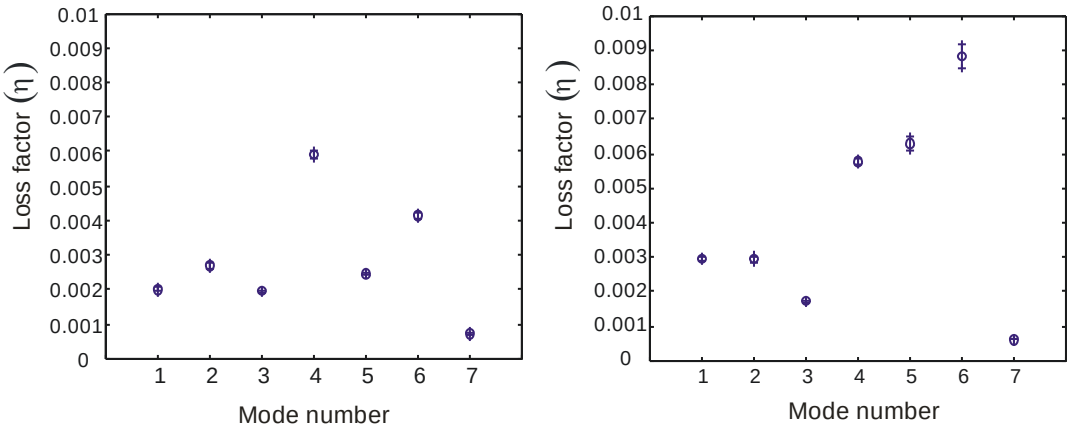

Figure 5.24: Loss factor estimation in two typical samples: o mean; + mean+/- standard deviation.

5.2.3 Spot welded assemblies' experimental modeshapes.

The modeshapes of the spot welded assemblies were measured in the same way as the single plates: a fixed accelerometer and a roving impact hammer, 9 impact locations distributed in a 3 by 3 array (see Figure 5.9) at each of the four faces of the assembly (36 impact locations).

The modal constant was calculated using equation (5.2). Figure 5.25 shows the first seven experimental modeshapes of a spot welded assembly, where a positive value corresponds to motion in the outward normal direction. The natural frequencies are given in Table 5-8. The first four modes can be recognized as ovalling modes, where modes 2 and 4 have out of phase motion between the front and rear section. Modes 1,3 and 2,4 can be identified as orthogonal pairs.

Mode number (n)	f_n (Hz)
1	303.72
2	341.66
3	552.80
4	722.67
5	948.34
6	978.94
7	1036.72

Table 5-8: Mean natural frequencies of spot welded assembly.

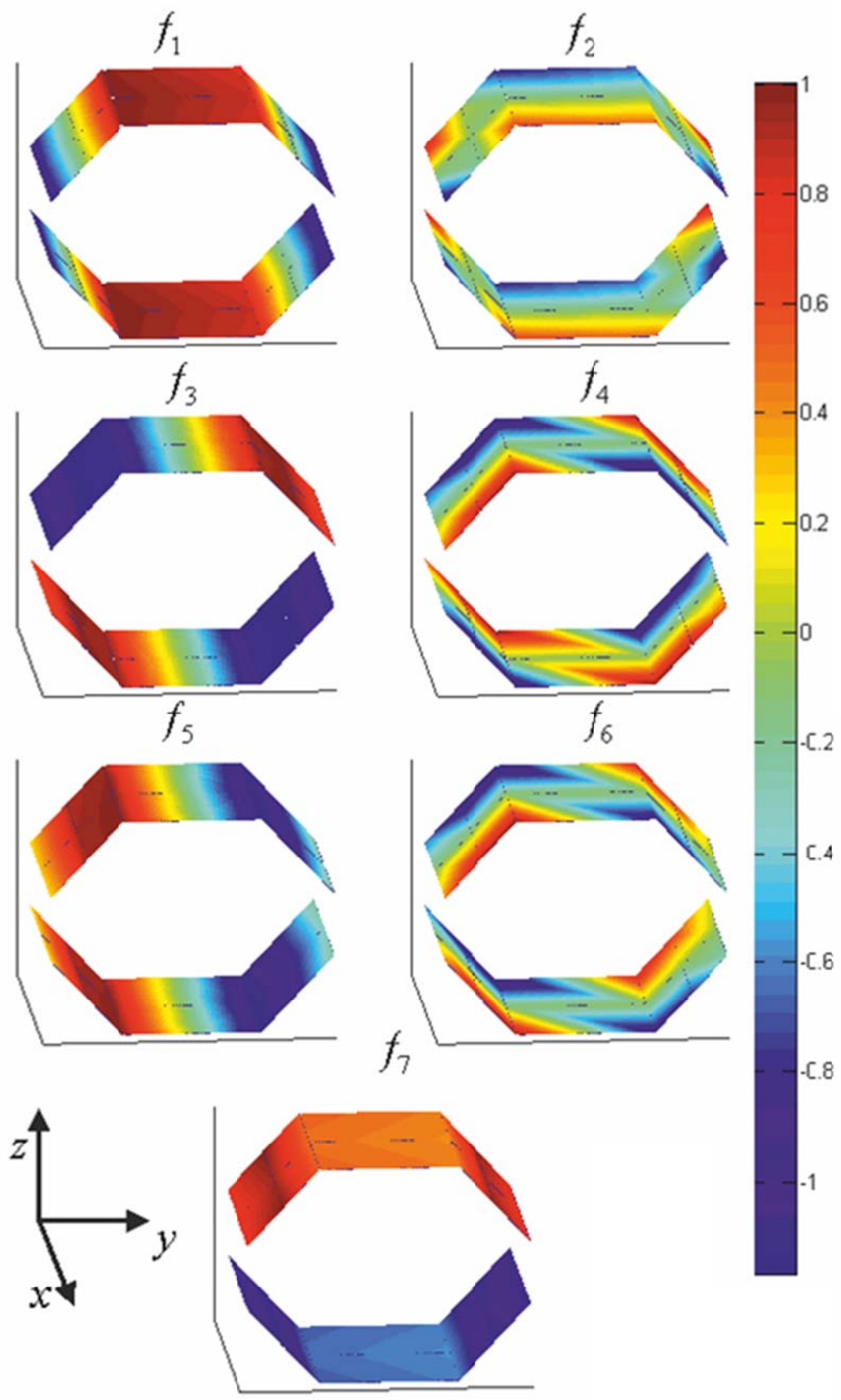

Figure 5.25: Experimental modeshapes for spot welded plates.

The modeshapes presented correspond to a specific sample. The behaviour of the other two samples is similar, presenting the same modeshapes in the same order.

5.2.4 Results

The experimental modal analysis was performed for all the samples and then repeated four more times. The variations from the same sample are lower than 1% for the natural frequencies and lower than .1% for the modal damping estimation; these variations are small especially when compared to the dispersion between samples. Therefore only the average results are reported and carried forward as the properties of each sample for the variability analysis between samples.

The mean and standard deviation for the natural frequencies and loss factor estimates across all 54 assemblies are shown in Table 5-9. This results can also be observed in Figure 5.26. It can be seen that for $n = 1, 2, 5, 6$ there is a larger variability where $\sigma_{f_n} \approx 0.02 f_n \sim 0.032 f_n$. For $n = 7$ there is an intermediate variability where $\sigma_{f_7} \approx 0.012 f_7$. For $n = 3, 4$ there is a small variability where $\sigma_{f_n} \approx 0.002 f_n \sim 0.005 f_n$.

The loss factor estimates show a large variability between samples. This is expected since the contact conditions can vary greatly between samples. In any case, the loss factor values are still very low and typically $\eta_n \leq 0.007$.

mode number (n)	1	2	3	4	5	6	7
$\overline{f}_n$ (Hz)	290.0	326.8	549.3	713.3	905.9	935.9	1014
σ_{f_n} (Hz)	7.66	7.64	1.53	3.99	27.9	30.0	12.4
$\overline{\eta}_n$	2.67E-03	4.31E-03	1.76E-03	5.52E-03	3.05E-03	4.74E-03	5.31E-04
σ_{η_n}	6.45E-04	6.83E-04	2.16E-04	1.15E-03	1.47E-03	1.68E-03	1.08E-03

Table 5-9: Mean and standard deviation of natural frequencies and loss factor estimates.

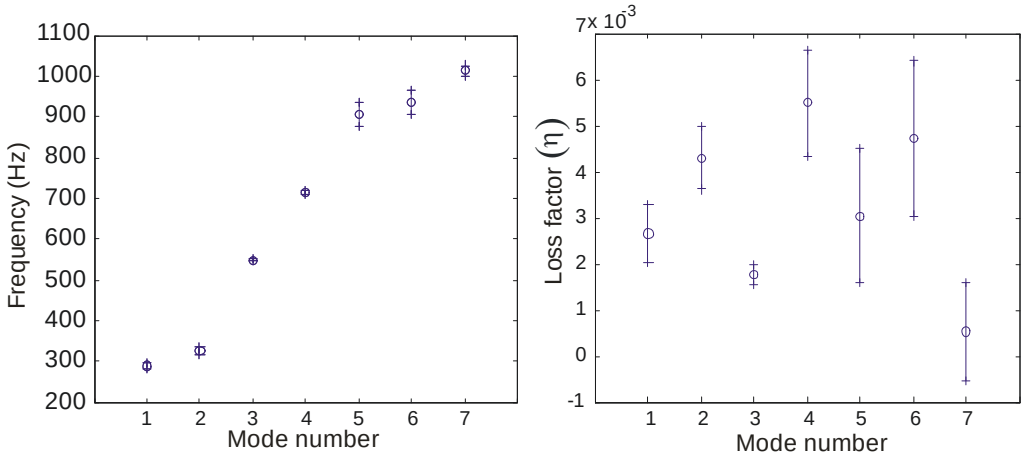

Figure 5.26:Natural frequencies and loss factor across the ensemble: mean; mean+/- standard deviation.

5.2.5 Statistical analysis

The probability distribution of the natural frequencies was analysed in terms of the normalized error

$$\varepsilon_n = \frac{\omega_n^{\,2} - \bar{\omega}_n^{\,2}}{\bar{\omega}_n^{\,2}} \tag{5.8}$$

Figure 5.27 shows the histograms of the first seven natural frequencies when compared to normal distribution. Table 5-3 shows the skew, kurtosis and the χ^2 probability results. It can be seen that modes 1,2,5,6 exhibit a larger variation and low kurtosis values, while modes 3 and 4 exhibit a very small variation with kurtosis values close to 3, while mode 7 exhibits an intermediate variation and a large kurtosis value.

The hypothesis that the natural frequencies fit a normal distribution can be rejected for mode 5, probably due to the heavy tails.

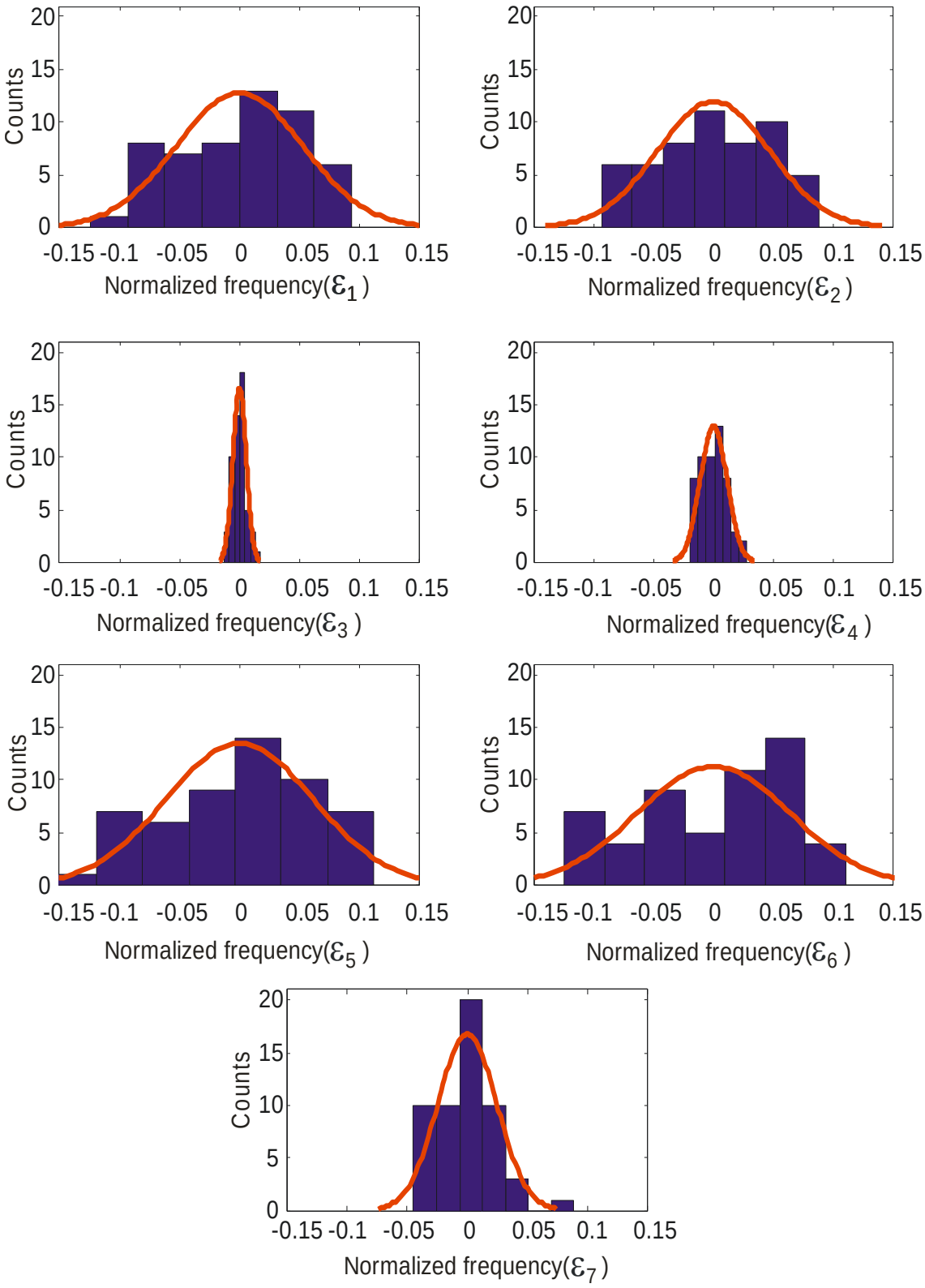

Figure 5.27: Distribution of the first seven natural frequencies (assembled profiles):
Experimental data; Gaussian distribution.

mode number (n)	1	2	3	4	5	6	7
σ_n	0.0526	0.0466	0.0056	0.0112	0.0613	0.0638	0.0245
Skew	0.797	0.622	0.491	0.120	0.913	0.790	0.524
Kurtosis	2.189	2.061	3.784	2.725	2.468	2.031	4.674
k	7	7	7	7	7	7	7
χ^2	5.95	4.21	3.27	1.19	8.14	5.85	3.05
Υ	7.78	7.78	7.78	7.78	7.78	7.78	7.78

Table 5-10: Skew, kurtosis and χ^2 probability results for goodness-of-fit test of ε_n.

The results from the statistical analysis suggest that modes 3 and 4 are not affected by the spot weld location, and since σ values are similar to those of the single hat profiles, it might confirm that they are only sensitive to variations in the geometry of the hat profiles and/or to variations in the material properties.

On the other hand, modes 1,2,5,6 are affected by the characteristics of the spot welds and exhibit a larger value of standard deviation. The low kurtosis values might be a sign of a low number of samples, i.e. more samples are needed to predict the correct PDF. In any case and based on the χ^2 goodness-of-fit results, one cannot reject the hypothesis that all the natural frequencies fit to a normal distribution.

These results will be compared with the results from the FE analysis in section 5.4.1.

5.2.6 Correlation coefficients

In section 5.2.3, it was observed that most of the modes considered depend greatly on the bending of the side panels, therefore it is expected that the natural frequencies are correlated between each other. In section 5.2.5 the statistical analysis of the experimental frequencies across the ensemble showed that some of the frequencies show a larger variation when compared to the standard deviation of the substructures, therefore it would be expected that the natural frequencies that exhibit a large variation are correlated between each other.

The level of correlation between modes is measured using the Pearson product-moment correlation coefficient [68] between ε_l and ε_m is calculated using equation (5.4).

Table 5-11 shows the correlation coefficients between ε_n. It can be confirmed that all the modes with large variability are correlated between each other, while the modes with smaller variabilities are not correlated to any other mode and not even between each other.

Figure 5.28 shows some of the dispersion plots with strong correlation, $r_{1,5} = 0.984$; weak correlation, $r_{6,7} = 0.177$; and a mild correlation, $r_{2,4} = 0.638$

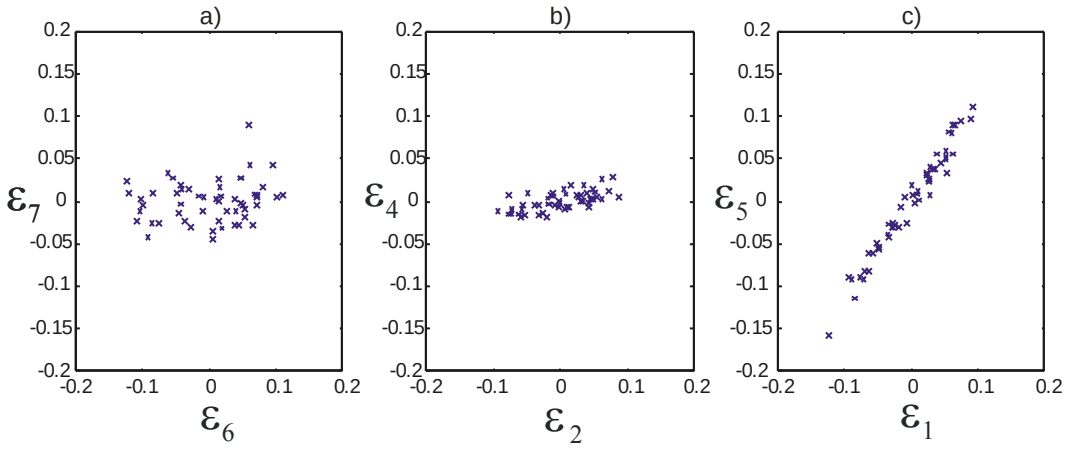

Figure 5.28: Dispersion plots: a) $r_{6,7} = 0.208$; b) $r_{2,4} = 0.638$; c) $r_{1,5} = 0.984$

n	1	2	3	4	5	6	7
1	-	0.953	0.397	0.606	0.984	0.966	0.208
2	0.953	-	0.447	0.638	0.951	0.966	0.171
3	0.397	0.447	-	0.178	0.445	0.412	0.517
4	0.606	0.638	0.178	-	0.574	0.585	-0.219
5	0.984	0.951	0.445	0.574	-	0.959	0.194
6	0.966	0.966	0.412	0.585	0.959	-	0.177
7	0.208	0.171	0.517	-0.219	0.194	0.177	-

Table 5-11: Correlation coefficients between ε_n.

5.3 The single profile finite element model

The FE model for the single plates was first built in ANSYS as shown in Figure 5.29. The mass and stiffness matrices were extracted to Matlab where Heterosis elements with the correct attributes were coupled into the missing areas, where the spot weld element will be located.

In order to experimentally estimate the material properties, simple beams were cut from the cladding sheets. The dimensions of the beams were measured using a vernier calliper and the thickness was measured using a micrometer. The weight was measured using a mechanical balance with 0.01 gram resolution. The dimensions and weight of the beams are in Table 5-12. E is estimated using the measured fundamental frequency ω_{b1} and the analytical formula

$$\omega_{b1}^2 = \frac{EI_b}{\rho A_b}\frac{(k_1 l)^4}{l^4} \tag{5.9}$$

where ρ is the estimated density, l is the measured length. A_b, I_b are the cross section and second moment of area of the beam calculated from the measured dimensions. $(k_1 l)$ is the first non-zero solution to the transcendental equation of beams with free boundary conditions $\left(\cosh(kl)\cos(kl)=1\right)$.

ω_{b1} was estimated using the circle fitting method [63] on the measured FRFs. The FRFs were measured using an impact hammer to excite the beam and the response was measured at the antinodes using a laser vibrometer to avoid mass loading. The beams were hung at the nodal points using elastic bands. The estimated properties are shown in Table 5-13.

In order to verify the construction of this model, the natural frequencies from the FE results are compared to the experimental average in Table 5-14. It can be seen that the difference between the two is always less than 2.5%. It should be noted that the

predicted natural frequencies are not always above or below the experimental values. Therefore, a change in the properties of the material would not necessarily lead to a better model.

The transfer function from an excitation at the top of the profile to the centre of the area modelled with Heterosis elements was evaluated and compared to experimental results for some of the samples in Figure 5.30. The agreement between both of them is good, where the resonances and antiresonances show the same behaviour.

l (m)	a (m)	b (m)	ω_{b1} (rad/s)	weight (kg)
0.29	0.0246	0.00071	280.07	0.03996

Table 5-12: Beam measured dimensions, first natural frequency and weight.

ρ (kg/m^3)	I_b (m^4)	A_b (m^2)	E (N/m^2)
7890	7.34E-13	1.75E-05	2.09E+11

Table 5-13: Estimated properties to use in the FE model.

The position of the resonances on the experimental results describes the variability of the manufacturing process while the FE result represents a sample with its natural frequency close to the experimental mean and not an additional sample as shown in Figure 5.30. This can be confirmed in Figure 5.31, where the FE natural frequency model profile lies close to the middle of the range when compared to the measured profiles.

The accuracy in the predicted modeshapes was evaluated using the modal assurance criterion (MAC), which is a widely used technique to estimate the degree of correlation between modeshape vectors. When a measured modeshape $\boldsymbol{\varphi}_m$ is compared to a subset of the computed modeshape $\boldsymbol{\varphi}_c$, where only the DOFs present in $\boldsymbol{\varphi}_m$ are extracted, the DOFs in $\boldsymbol{\varphi}_c$ need to be resolved in the appropriate direction to match the direction of the DOFs present in $\boldsymbol{\varphi}_m$. The MAC as defined in [69] is used in this study, i.e.

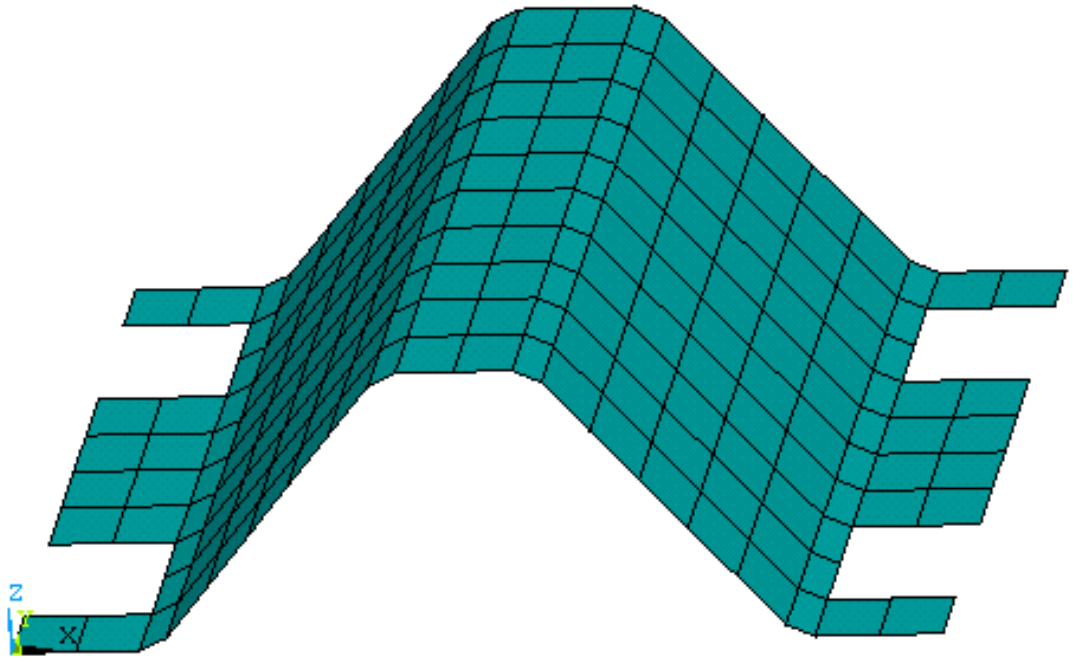

Figure 5.29: ANSYS FE model

	f_1 (Hz)	f_2 (Hz)	f_3 (Hz)	f_4 (Hz)	f_5 (Hz)	f_6 (Hz)	f_7 (Hz)
FE model	188.84	198.08	324.28	663.28	819.58	1024.9	1216.2
Experimental average	188.78	203.004	328.3955	656.15	819.84	1015.3	1221.5

Table 5-14:FE natural frequencies compared to the experimental mean values.

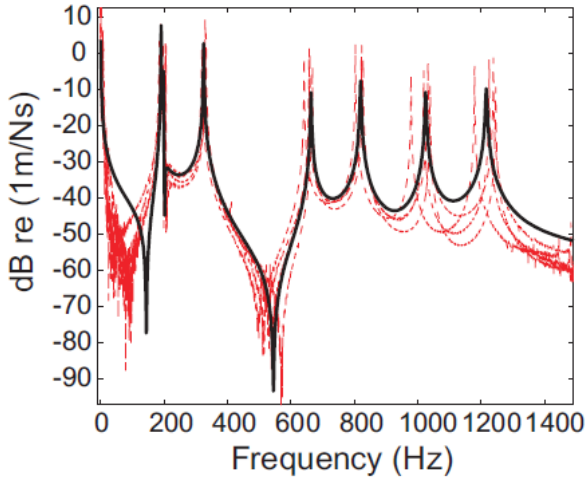

Figure 5.30: Transfer mobility: - - - experimental; —— FE model.

$$MAC = \frac{\left|\boldsymbol{\varphi}_m^T \boldsymbol{\varphi}_c\right|^2}{\left(\boldsymbol{\varphi}_c^T \boldsymbol{\varphi}_c\right)\left(\boldsymbol{\varphi}_m^T \boldsymbol{\varphi}_m\right)} \tag{5.10}$$

The *MAC* value is a scalar with values between 0 and 1, where 1 means that that one mode shape vector is a scaled multiple of the other. The **MAC** is a matrix of *n* x *n* size, where *n* is the number of modes considered in the evaluation. When the experimental and predicted modes are identical the diagonal terms are equal to 1, but the off diagonal terms are not necessarily equal to zero. This is because even if $\boldsymbol{\varphi}_m$ and $\boldsymbol{\varphi}_c$ are different modeshapes, they are not orthogonal vectors (although they are orthogonal with respect to the mass and stiffness matrices).

There are modes that are similar to each other and with the number of measured points they cannot be completely differentiated, that is the case of modes 4 and 6 as can be observed in Figure 5.32 where the graphical representation of the **MAC** matrix is shown. Other modes might exhibit some smaller similarities, like for example modes 3 and 7. However the prediction of the mode shapes is adequate, since the mode shapes are presented in the right order and the **MAC** diagonal values are always higher that 0.7 as can be seen in Figure 5.32. Similar behaviours were observed when the computed mode shapes were compared to mode shapes measured for different samples.

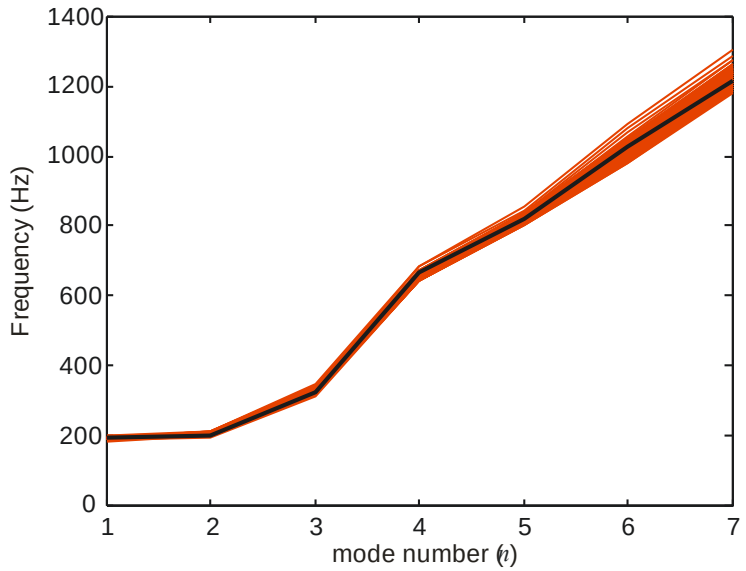

Figure 5.31: Natural frequencies profiles: —— measured; ━━ deterministic FE model.

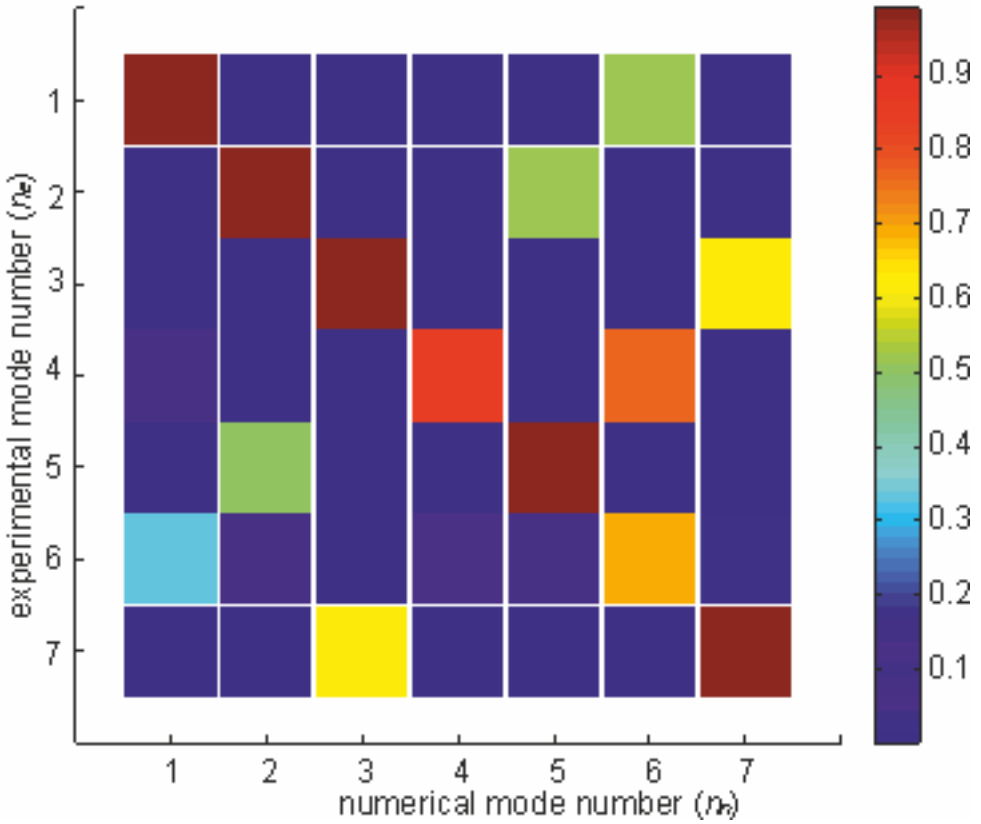

Figure 5.32: Graphical representation of MAC matrix.

5.4 The spot welded profile finite element model

The spot welded model was created taking two of the single profiles models as described in section 5.3. These two models were assembled together using the CMS approach described in section 3.2, where the response of the assembled structures is calculated by updating the response of the unassembled system. The spot welds are respresented using the model proposed in section 4.2, this model is capable of simulating changes in the spot weld location and diameter.

In order to estimate the variability in the vibration response of this system due to uncertainties in the location and diameter of the spot welds, a MCS with 500 samples is used to estimate the envelope of the transfer mobility. The (x_s, y_s) coordinates of each of the s spot welds are assumed to be independent Gaussian random variables with their means located at the baseline position and standard deviation given in Table 5-6.

The diameter of the spot weld is also considered as an independent random variable with mean and standard deviation given in Table 5-7.

The transfer functions were measured from hat plate to hat plate as shown in Figure 5.21. This is the same transfer function measured in the 54 physical samples. The response envelope is compared to the measurements in Figure 5.33.

Figure 5.33 shows that the main difference between the numerical and experimental results can be observed at low frequencies, where the experimental rigid modes show some variability due to changes in elastic mounting and can be observed from 0 up to 8.5 Hz while in the numerical results this modes are always at 0 Hz. In the MCS result there are no variations on f_3 and f_4, but this corresponds to the behaviour in the experimental results where the variation in f_3 and f_4 exhibit small spread, especially when compared to other natural frequencies as can be observed in Figure 5.33 and confirmed in Figure 5.27. Then the small variability of f_3 and f_4 in the experimental results is related to the variability on the single profiles and not to the position of the spot welds, taking into consideration that in the FE model the properties of the substructures are considered as deterministic.

It can also be noted that f_3 is overestimated while f_4 is underestimated, this means that there is a modelling error in the way in which the single plates where modelled. This is more likely to be related to the geometric properties of the profile rather than to the material properties. If the model of the single plate were improved, then the accuracy in the prediction of these two natural frequencies would improve as well.

The variation in the lowest two natural frequencies and the mobility magnitudes at resonances are estimated very accurately. This means that the variability of these natural frequencies is related to the variation of the spot welds, rather than variation in the substructures properties.

Above 800 Hz the envelope covers an area where f_5 and f_6 vary, in this area the frequency ranges for f_5 and f_6 overlap. This behaviour can be observed in the MCS envelope as well as in the experimental FRFs. On the other hand, the mobility magnitude at resonances in these two modes are usually under estimated, which means that the modal loss factors η_5 and η_6 used in the simulation are high compared to the real values. In practice, these show a large variability as observed in Figure 5.26 and in Figure 5.33, where the peak values exhibit a curved shaped spread rather than a flat spread as can be observed in the MCS envelope using a constant value for the loss factor η_n. In any case, the MCS FRF envelope is similar to the envelope of measured FRFs and the shape is very similar, which means that the method is efficiently predicting the variations in the response due to uncertainties in the location and in the size of the spot welds. This method can also reproduce the FRF percentiles when compared to the experimental results as can be observed in Figure 5.34.

The predicted natural frequencies using MCS are compared to the measured natural frequencies in Figure 5.35, where it can be seen that the MCS results overlap the experimental results when the proposed spot weld model is used. In contrast, when the simple spring spot weld model is used, the natural frequencies are clearly underestimated, as explained before; this is due to the fact that the simple spring model does not represent the area of contact which adds stiffness in the flanges, on the other hand, the change in diameter cannot be modelled using this simple model.

The statistical analysis of each natural frequency will be performed in the next section, but before that, it is important to determine if the modes above 800 Hz change order or not. In order to do that, the **MAC** matrix will be calculated for each one of the MCS comparing it to the experimental measurement described in section 5.2.3.

The **MAC** matrix is first calculated for the baseline configuration, which means that all the spot welds are located at its mean position. When the new **MAC** matrix is calculated and compared to the one calculated for the single profile, it can be seen that in this case, the diagonal values are closer to one as shown in Figure 5.32, this is due to the fact that more locations are used in order to calculate each $\mathbf{MAC}(i,i)$ value; 36 vs

18. It is also related to the fact that simpler modeshapes are in the assembly where only first bending is involved with out of phase – in phase combinations as can be observed in Table 5-8.

When the **MAC** matrix of the average of the assembly is analysed, the modes appear to be in the same order. When the sample with the minimum **MAC**(i,i) value is analysed, the modes 6 and 7 swap order as can be seen in Figure 5.36 c. When the sample with the second minimum **MAC**(i,i) value is analysed, modes 4 and 5 start to look very similar but these modes do not appear to swap order. Therefore, only one sample out of the 500 samples experiences a change in the order of the modes, this case sample will not be considered for the statistical analysis in the following section.

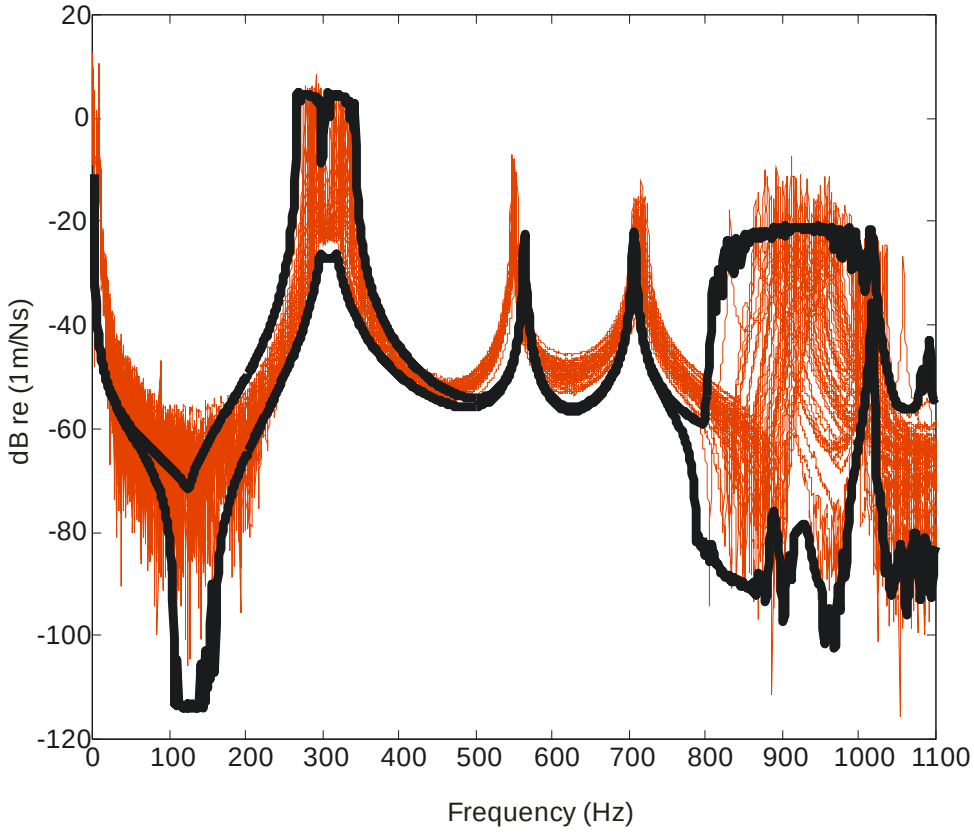

Figure 5.33: Response envelopes for the magnitude of the mobility: —— measured; ▬▬ FE envelope.

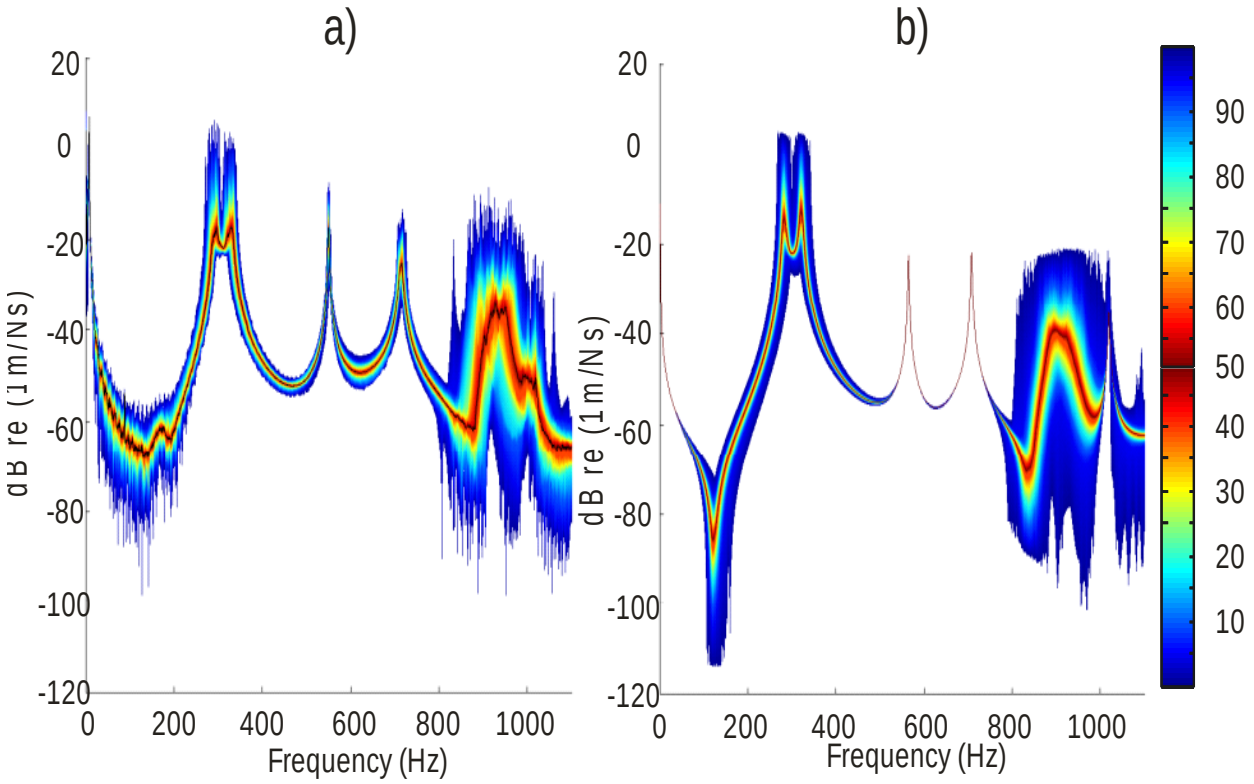

Figure 5.34: FRF percentiles in the frequency domain: a) measured; b) FE MCS.

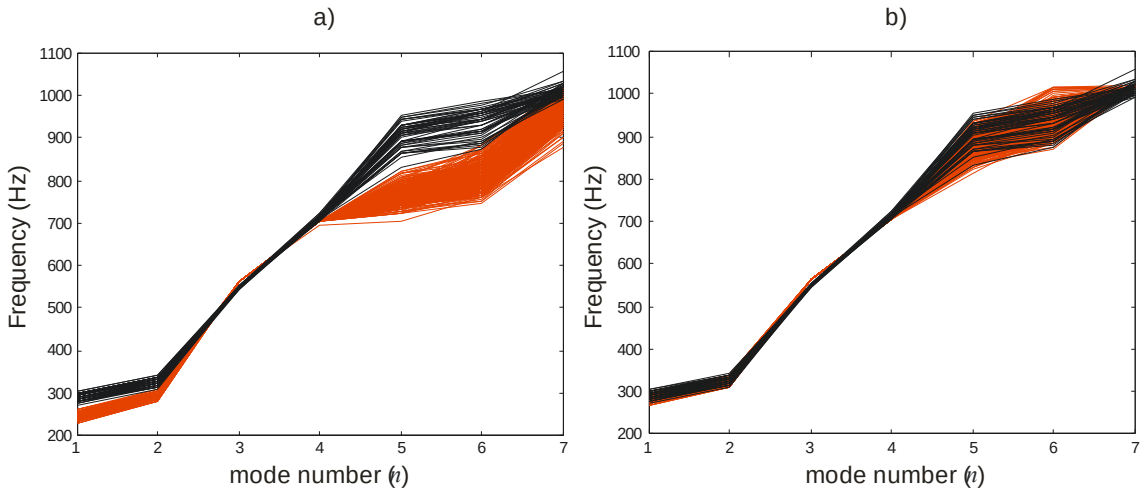

Figure 5.35: Natural frequencies for the first seven flexural modes: a) simple spring model; b) proposed model.: —— FE MCS; —— measured.

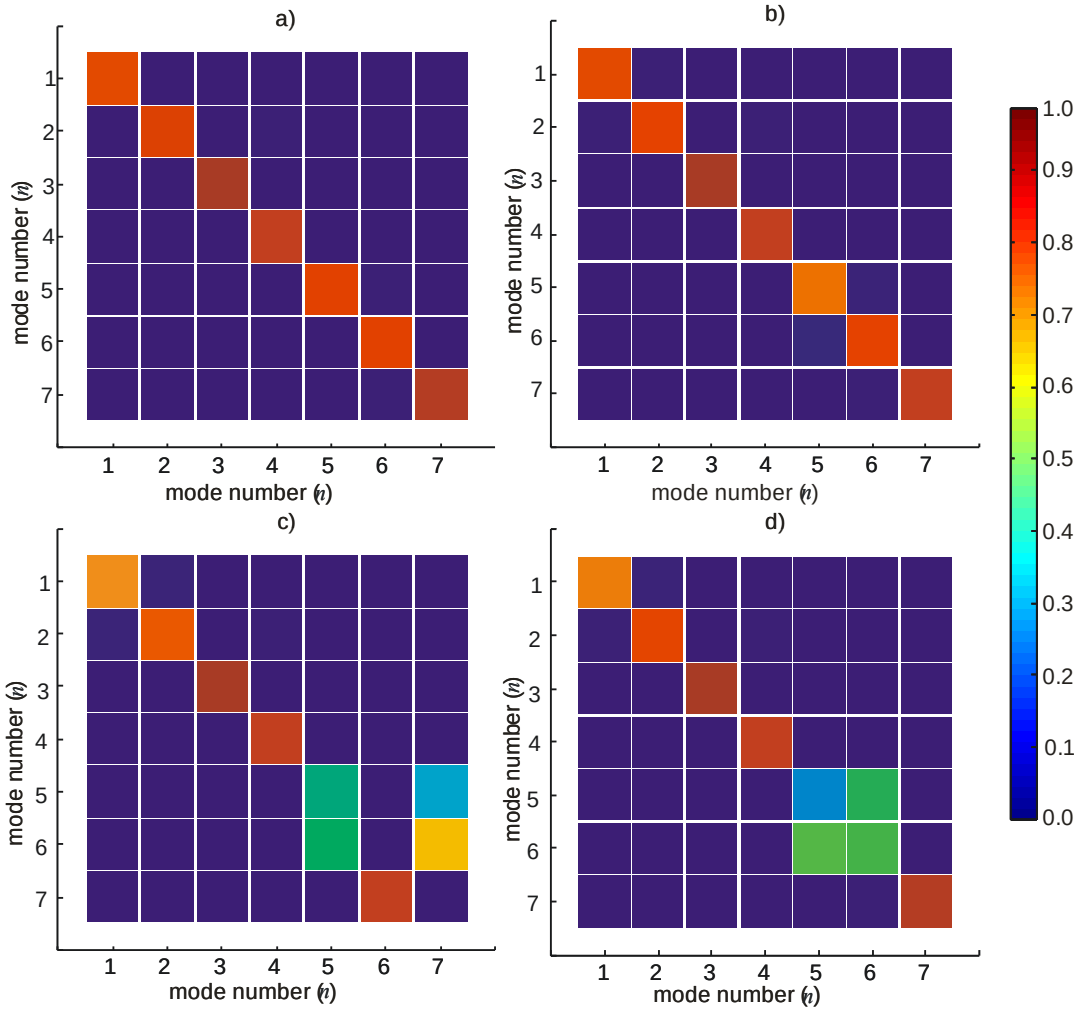

Figure 5.36: Graphical representation of **MAC** matrix: a) baseline configuration; b) ensemble average;c) and d) 2 samples with $\mathbf{MAC}(i,i) < 0.4$.

5.4.1 Statistical analysis

The dispersion of the natural frequencies are analysed in terms of the normalized error as calculated in equation (5.3).

Figure 5.37 shows the histograms of the first seven natural frequencies when compared to normal distribution. Table 5-15 shows the skew, kurtosis and the χ^2 probability results. It can be seen that modes 1,2,5 and 6 are clearly affected by the uncertainty in the spot weld position, while the natural frequencies for modes 3,4 and 7 are almost insensitive to the uncertainties in the spot welds properties.

The skew and kurtosis values in modes 1,2,5 and 6 suggest that they might fit a normal distribution, i.e. the skew values are low and the kurtosis values are close to three. However, based on the results from the χ^2 goodness-of-fit results, the hypothesis that the assembly natural frequencies fit to a normal distribution is rejected, except for mode 5. As said before, modes 3,4 and 7 are not affected by the properties in the connections, therefore it is irrelevant if they fit or not into a normal distribution.

On the other hand, based on the experimental results, modes 1,2,5 and 6 are expected to fit a normal distribution. Mode 5 does, and if the significance level were reduced to $\alpha = 0.05$ the distributions for modes 1 and 2 could also be considered as normal.

When compared to the experimental results in Table 5-10 and Figure 5.27, it can be observed that the modes with larger variation in the MCS results correspond to the modes with larger variation in the experimental results. Furthermore, the modes in which the natural frequencies are insensitive to the spot weld characteristics in the MCS also correspond to the modes with low variation in their measured natural frequencies.

When the standard deviation of the natural frequencies for the FE MCS and experimental results are compared, it can be seen that the simulation results underestimate the experimental results in all modes as seen in Figure 5.38. It can also be seen that the difference between the measured and the estimated σ_n is almost constant in all modes, including the insensitive frequencies. This difference can be attributed to variability in the properties of the substructures which are not considered in the FE MCS.

mode number (n)	1	2	3	4	5	6	7
σ_n	0.0526	0.0466	0.0056	0.0112	0.0613	0.0638	0.0245
Skew	0.797	0.622	0.491	0.120	0.913	0.790	0.524
Kurtosis	2.189	2.061	3.784	2.725	2.468	2.031	4.674
k	29	29	29	29	29	29	29
χ^2	37.481	63.693	38.709	37.861	20.630	54.242	374.906
Υ	35.563	35.563	35.563	35.563	35.563	35.563	35.563

Table 5-15: Skew, Kurtosis and χ^2 probability results for goodness-of-fit test of ε_n.

Hence it can be said that the method presented here is accurate when predicting which modes are sensitive to the uncertainties in the spot welds and which modes are not. It can also predict the standard deviation of the natural frequencies distributions as a result of spot weld variation. This method also predicts the correlation between the normalized natural frequencies accurately, as can be observed in Figure 5.39.

On the other hand, PDF properties such as kurtosis and goodness of fit to a normal distribution were not correctly predicted, perhaps due to the difference in the number of samples between the experiments and the FE MCS. i.e. 50 vs 500.

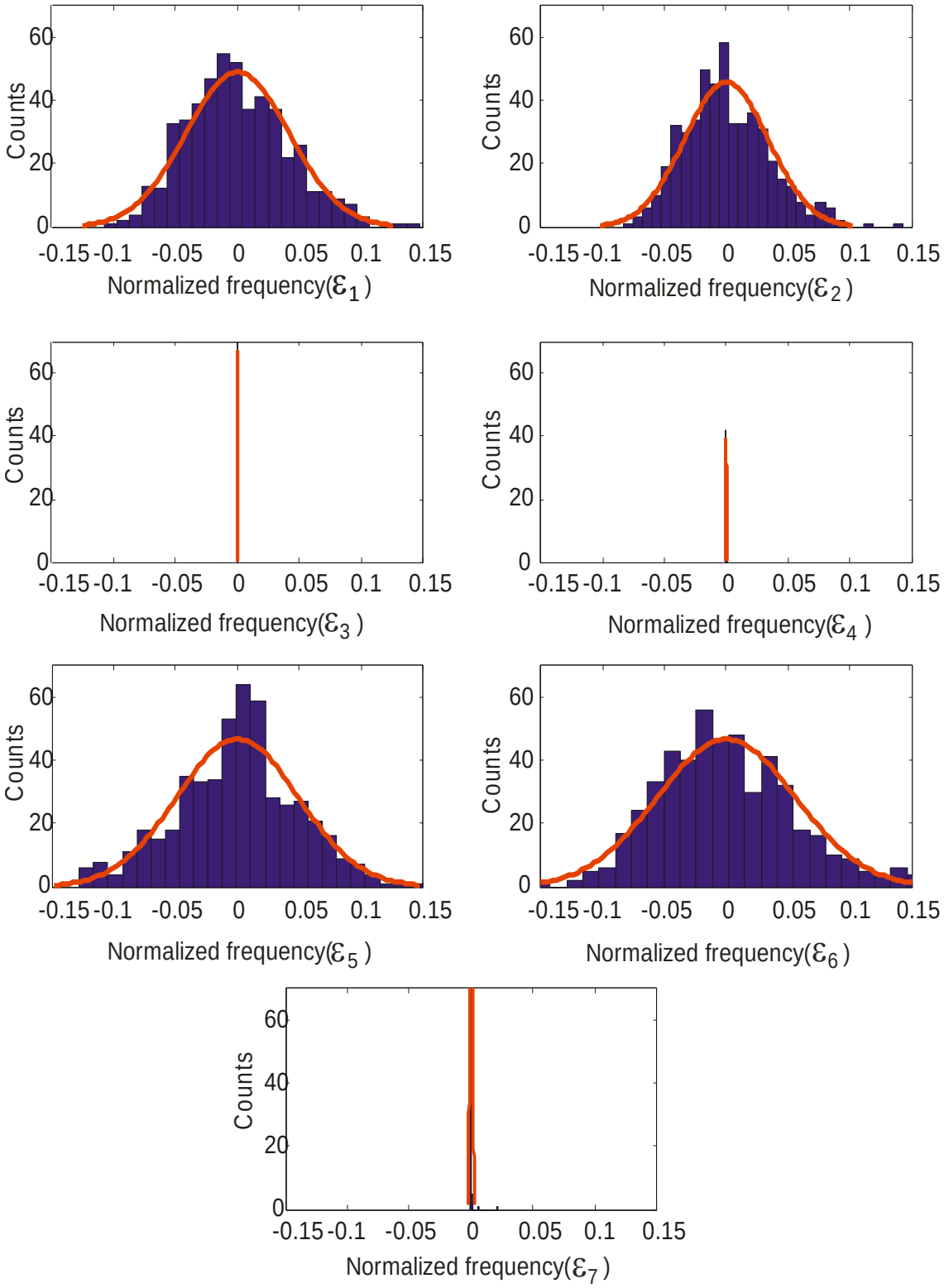

Figure 5.37: Distribution of the first seven natural frequencies:
MCS results ; Gaussian distribution.

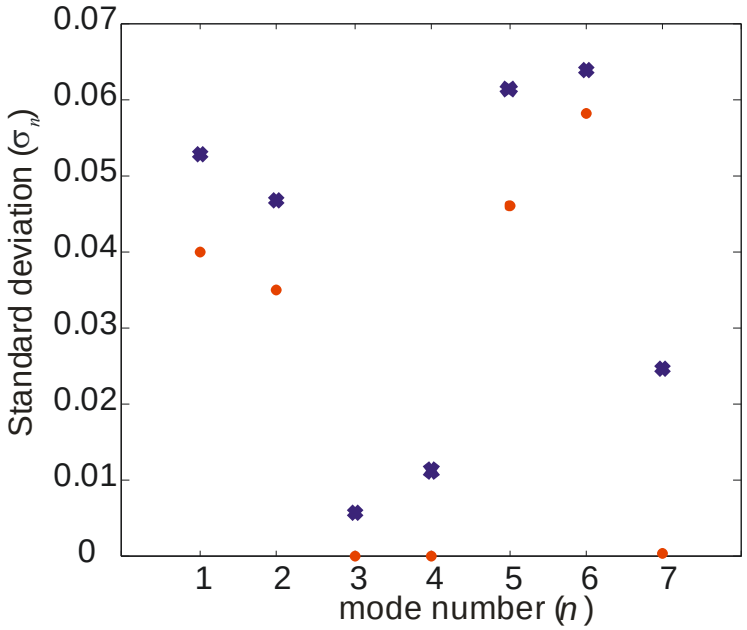

Figure 5.38: Standard deviation of natural frequencies distribution (σ_n):
● experiments; ● FE MCS.

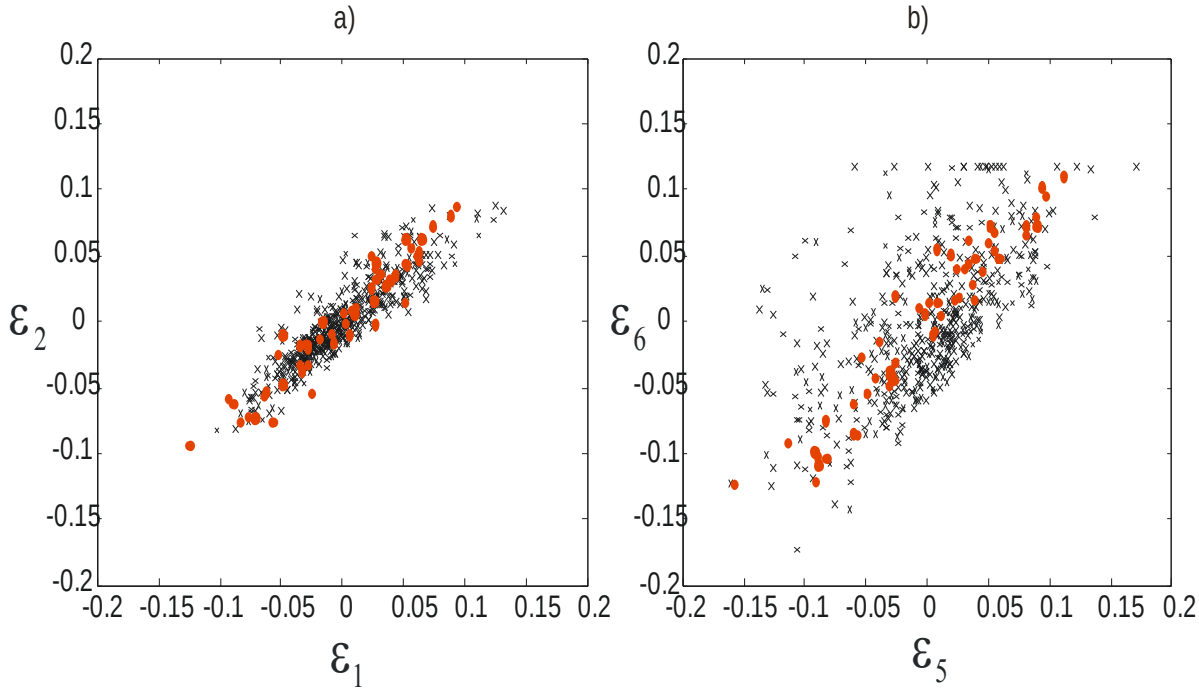

Figure 5.39: Normalized natural frequencies: a) ε_1 vs ε_2; b) ε_5 vs ε_6:
● experiments; **x** FE MCS.

5.5 Conclusions

In this chapter the proposed spot weld model in Chapter 3 and the method to evaluate the variability in the structure properties due to uncertainties in the spot welds was validated using experimental results. A double hat structure was chosen for this purpose.

159 profiles were fabricated and tested before assembly, the natural frequencies were measured and their probability density functions (PDF) were studied. In order to reduce the variability in the substructures the samples with larger errors in the modal frequencies when compared to the mean were discarded; 108 profiles were left.

After being welded, the spot weld size and location were measured. The natural frequencies, loss factor and mode shapes were estimated and analysed. The damping estimates together with the spot weld size and location are used as inputs for the FE model.

A deterministic FE model for the single profiles was built and compared to experimental measurements to evaluate its performance. Finally the assembly was built in a MCS with stochastic spot weld properties and compared to the test results.

It was concluded that the modal frequencies of the single profiles fit into a normal distribution and the modal loss factors are always lower than 3.5×10^{-3}. Measured spot weld position, spot weld size and assembly modal frequencies also fit into a normal distribution.

When the deterministic FE model of a single plate is compared to the ensemble of measurements, the agreement between both of them is good, where the resonances and antiresonances show the same behaviour. The position of the resonances in the experimental results describes the variability of the manufacturing process, while the FE result represents a sample with natural frequencies close to the experimental mean modal frequencies. The prediction of modeshapes was also satisfactory.

When the proposed spot weld model is used, the predicted natural frequencies overlap the experimental results. The modeshapes are correctly predicted and the modeshape analysis show that in general the modes do not swap order. In contrast, when the simple spring spot weld model is used the natural frequencies are clearly underestimated.

Finally, the method presented here is accurate when predicting which modes are sensitive to the uncertainties in the spot welds and which modes are not. It can also predict the standard deviation of the natural frequencies distributions as a result of spot weld variation. This method also predicts the correlation between the normalized natural frequencies accurately.

6 CONCLUSIONS AND FUTURE WORK

6.1 Conclusions

Spot welds are the most important structural joint in the automotive industry. A vehicle body contains several thousands of spot welds. There is an inherent variability in these joints due to the complexity in the manufacturing process.

These variations lead to variations in the joint dynamic properties and the resulting overall dynamic behaviour of the built up structure. At this moment there is not a method in which the uncertainties in the spot welds are considered when predicting the global dynamic properties such as frequency response functions (FRFs), eigenvectors, eigenvalues etc.

In this thesis an efficient method to calculate the variability in the dynamic properties of spot welded structures due to uncertainties in the location and size of the spot weld was proposed and experimentally validated.

The finite element method (FEM) is used in conjunction with Monte Carlo simulations (MCS) to predict the variability in the vibration response of the spot weld structures; this is usually computationally expensive especially for large scale models.

In this thesis the computational time of such analyses is reduced up to 99% using a proposed spot weld model based on multipoint constraints (MPCs) and an analytical update theory in the component mode synthesis (CMS) framework and the results were experimentally validated.

In chapter 2 MPCs were used to apply connections between flat structures. It was shown that an MPC connection can be placed between nodes of an FE model and is able to incorporate any change in the location of the elastic connection in an accurate way.

When beams are connected, results showed that the MPC connection has the same predictive performance compared to the direct node to node connections. Both models giving accurate results for point connections comprising a translational or rotational spring.

Results showed that the MPC connection is not accurate when thin plate elements are used, due to the non-conforming formulation. In contrast, when the Heterosis element was used the results showed that the MPC connection is as accurate as the node-to-node connection. Additional errors appear when rotational springs are used in the connection, due to discrepancies between the element formulation and the analytical solution. Some convergence issues exist in the modal summation when rotational degrees of freedom (DOFs) are involved; however the solution is still acceptable.

When a rotational spring is used, the transfer mobility magnitude is sensitive to the element size. This problem is not related to the MPC, since the MPC and node to node connection results are almost identical. Furthermore, the MPC results are closer to the analytical solution. This sensitivity is related to the addition of rotational stiffness into the FE stiffness matrix.

In chapter 3 MPCs in combination with CMS were used to predict the response where there are uncertainties in the joint locations in a FE model. It was seen that CMS gives a sub-structuring framework and a reduction in the number of DOFs of the model. Combining both approaches, the response of the system can be evaluated for any

connection location using the unchanged modal representation of the substructures in an accurate and numerically efficient manner.

However, when the number of degrees of boundary DOFs is large, then the CMS size reduction is less efficient since the interface DOFs are not reduced. Two techniques are proposed to overcome this problem: (i) characteristic constraint modes [3] and (ii) low rank update theory [4].

The vibration response was calculated using these approaches for different connection positions and compared to a full modal solution. The predictions obtained gave a good agreement and the computational time was reduced by approximately 99% when compared to the full modal solution. When compared to the characteristic constraint mode method, the low rank update approach leads to a reduction in the computational time t at a rate of $t^{2/3}$.

The last approach was used in a MCS with 500 samples to evaluate the variability in the vibration response. The results show that probability density functions (PDFs) of the system natural frequencies are not Gaussian even though the connection locations are Gaussian variables.

A second MCS was used to evaluate the variability in the vibrational response due to missing or broken connections and/or uncertainty in the location of the spot-welds in a model of two plates with five spot welds. Results show that, for the example considered, when any of the inner spot welds is missing and the location and size of the remaining connections is uncertain the vibration responses lie approximately within the bounds of the case in which all the connections are present. On the other hand, when any of the outer connections are absent the variability in the vibration response is greater.

In chapter 4 a new spot weld model was proposed. This model imposes a surface-to-surface connection between two structures using simple spring elements and MPCs, therefore coincident meshes are not required. The application of the new spot-weld model is validated experimentally on a model of two simply supported plates with three spot weld connections. The performance is compared to a simple MPC connection.

It was shown that when plate elements are based on Mindlin-Reissner plate theory, the stiffnesses in the rotational DOFs depend on the element size in a quadratic way. In addition, when the rotational stiffness of the connection is added to the system, it results in a high sensitivity of the static solution and natural frequencies to the element size. This was demonstrated on an assembly of two simply supported plates with a single connection.

The new model does not add stiffness to the rotational DOFs, but instead it is composed of an array of springs that add an equivalent rotational stiffness to the system. The results show that the new spot weld model reduces the sensitivity substantially and improves convergence with different mesh sizes. For the structures considered, convergence is achieved with an 8mm element size compared to a plate thickness of 1.96mm, whilst for the simple MPC model convergence is not achieved. The average sensitivity to element size at 10mm is reduced almost five times from 346.7 Hz/m to 70.49 Hz/m.

In chapter 5 the proposed spot weld model in Chapter 3 and the method to evaluate the variability in the structure properties due to uncertainties in the spot welds was validated using experimental results. A double hat structure was chosen for this purpose.

159 profiles were fabricated and tested before assembly, the natural frequencies were measured and their PDFs were studied. In order to reduce the variability in the substructures the samples with larger errors in the modal frequencies when compared to the mean were discarded; 108 profiles were left.

After being welded, the spot weld size and location were measured. The natural frequencies, loss factor and mode shapes were estimated and analysed. The damping estimates together with the spot weld size and location are used as inputs for the FE model.

A deterministic FE model for the single profiles was built and compared to experimental measurements to evaluate its performance. Finally the assembly was built in a MCS with stochastic spot weld properties and compared to the test results.

It was concluded that the modal frequencies of the single plates fit into a normal distribution and the modal loss factors are always lower than 3.5×10^{-3} .Measured spot weld position, spot weld size and assembly modal frequencies also fit into a normal distribution.

When the deterministic FE model of a single plate is compared to the ensemble of measurements, the agreement between both of them is good, where the resonances and antiresonances show the same behaviour. The position of the resonances in the experimental results describes the variability of the manufacturing process while the FE result represents a sample with natural frequencies close to the experimental mean modal frequencies. The prediction of modeshapes was also satisfactory.

When the proposed spot weld model is used, the predicted natural frequencies overlap the experimental results. In contrast, when the simple spring spot weld model is used, the natural frequencies are clearly underestimated. The modeshapes are correctly predicted and the MAC analysis show that the modes do not swap order in all samples.

Finally, the method presented here is accurate when predicting which modes are sensitive to the uncertainties in the spot welds and which modes are not. It can also predict the standard deviation of the natural frequencies distributions as a result of spot weld variation. This method also predicts the correlation between the normalized natural frequencies accurately.

6.2 Future work

In this thesis the propagation of uncertainties in the spot welds was computed using a standard MCS. The computational time was reduced using characteristic constraint modes/update theory in a CMS framework, here the computational time of the deterministic solution is reduced. The calculation cost for one solution can also be

reduced drastically, if numerically expensive operations, such as solving the eigenvalue problem, are replaced with numerically cheap formulations. First order perturbation methods using response sensitivities [70] are appropriate for low levels of uncertainty. For larger uncertainties, higher order perturbation or interpolation can be used. A systematic approach to select the reference solutions for an interpolation is given by the design of experiments methodology. It can also be used to construct an approximate response surface model (RSM) [71], which replaces the original model to provide a relationship between input parameters and response quantities. Although a replacement of the original model is often associated with errors due to approximations, these can often be neglected with respect to the level of uncertainty in the input data.

Another option that could be explored is to apply techniques designed to reduce the number of necessary evaluations by using advanced sampling techniques [72]. These reduce the variance of the sampling estimator and achieve the same accuracy with a lower number of samples. The most common techniques are importance sampling [54], directional sampling [73], subset simulation and Line-Sampling [74]. The DOE methodology can also be applied to create advanced MC methods to estimate the mean and variance of a distribution using a very low number of samples. Latin Hypercube sampling [75] is a version of stratified sampling, where it is ensured that the samples are taken more evenly from the input parameter distribution. In contrast to sampling approaches, there are various subspace projection schemes, such as polynomial chaos expansion [76] and stochastic reduced basis methods [77].

It could also be possible to apply a possibilistic approach, in this case, the complication comes when defining the bounds of the solution. In this case a small MCS can be run and the 5 and 95 percentiles in the stiffness matrix can be taken as the lower and upper bounds in the possibilistic method.

In order to not only model the variability in the spot welds but also the variability in connected panels, statistical energy analysis (SEA) could be used to model large panels and coupled to small FE sections where the spot welds are located (e.g. the landings or flanges on the hat profiles can be modelled with FEA while the rest of the structure could be modelled using SEA). This would create a hybrid FE-SEA model that

potentially could extend the frequency domain of the analysis, reduce further the computational time and also consider the variability in the rest of the structure.

This approach could be used for reverse problems in which, for a given set of requirements such as standard deviation of natural frequencies, a maximum tolerance in the location and size of the spot weld is determined.

The proposed methodology should be applied in structures with a larger number of spot welds and more than two components in order to study the feasibility of applying it in industrial problems. The final goal would be the implementation of the current approach in large built up models such as a vehicle body-in-white with three to five thousands spot welds.

7 REFERENCES

[1] E. Feulvarch et al., "Resistance spot welding process: experimental and numerical modeling of the weld growth mechanisms with consideration of contact conditions," *Numerical Heat Transfer, Part A (Applications)*, vol. 49, no. 4, pp. 345-367, Aug. 2006.

[2] Z. Feng, J. E. Gould, S. S. Babu, M. L. Santella, and B. W. Riemer, "An Incrementally Coupled Electrical-Thermal-Mechanical Model for Resistance Spot Welding," Trends in Welding pp. 599-604 ASM International (1998).

[3] A. M. Chertov and R. G. Maev, "A one-dimensional numerical model of acoustic wave propagation in a multilayered structure of a resistance spot weld," *IEEE Transactions on Ultrasonics, Ferroelectrics and Frequency Control*, vol. 52, no. 10, pp. 1783-1790, 2005.

[4] P. Lardeur and M. Scionti, "Verification and validation of finite element models for the vibrational behaviour of a windscreen in presence of variability," in *International Conference on Noise and Vibration - ISMA 2006*, 2006.

[5] M. Palmonella, M. I. Friswell, J. E. Mottershead, and A. W. Lees, "Finite element models of spot welds in structural dynamics: review and updating," *Computers & Structures*, vol. 83, no. 8-9, pp. 648-661, 2005.

[6] K. Pal and D. L. Cronin, "Static and dynamic characteristics of spot welded sheet metal beams," *Journal of Engineering for Industry, Transactions of the ASME*, vol. 117, no. 3, pp. 316-322, 1995.

[7] D. Heiserer, J. Sielaft, and M. Charging, "High Performance Process Oriented Weld Spot Approach," in *1st MSC Worldwide Automotive User Conference.*, 1999.

[8] MacNeal-Schwendler Corporation., "MSC/NASTRAN user's manual." MacNeal-Schwendler Corporation, Los Angeles, Calif., 2004.

[9] S. Donders, M. Brughmans, L. Hermans, and N. Tzannetakis, "The effect of spot weld failure on dynamic vehicle performance," *Journal of Sound and Vibration*, vol. 39, no. 4, pp. 16-25, 2005.

[10] J. Fang, C. Hoff, B. Holman, F. Mueller, and D. Wallerstein, "Weld modelling with MSC.Nastran," in *2nd MSC Worldwide Automotive User Conference*, 2000.

[11] W. M. Dong, W. L. Chiang, and F. S. Wong, "Propagation of uncertainties in deterministic systems," *Computers and Structures*, vol. 25, no. 3, pp. 415-423, 1987.

[12] W. Dong and H. Shah, "Vertex method for computing functions of fuzzy variables," *Fuzzy Sets and Systems*, vol. 24, pp. 65-78, 1987.

[13] G. I. Schuëller, "Computational stochastic mechanics - recent advances," *Computers and Structures*, vol. 79, pp. 2225-2234, 2001.

[14] G. I. Schueller et al., "A State-of-the-Art Report on Computational Stochastic Mechanics," *Probabilistic Engineering Mechanics*, vol. 12, no. 4, pp. 197-321, 1997.

[15] G. Upton and I. Cook, *Dictionary of statistics*. Oxford University Press, 2004.

[16] G. S. Fishman, *Monte Carlo: Concepts, algorithms, and applications*. Berlin: Springer-Verlag, 1996.

[17] N. Metropolis and S. Ulam, "The Monte Carlo method," *Journal of the American Statistical Society*, vol. 44, pp. 335-341, 1949.

[18] M. M. Drugan and D. Thierens, "Evolutionary Markov chain Monte Carlo." *Lecture Notes in Computer Science*, 2004, Volume 2936/2004, 63-76.

[19] R. Y. Rubinstein, *Simulation and the Monte Carlo Method*. New York: Wiley, 1981.

[20] J. M. Hammersley and D. C. Handscomb, *Monte Carlo Methods*. Norwich: Fletcher and Son Ltd., 1967.

[21] R. R. Craig Jr. and M. C. C. Bampton, "Coupling of substructures for dynamic analyses," *AIAA Journal*, vol. 6, no. 7, pp. 1313-1319, 1968.

[22] M. P. Castanier, Y. C. Tan, and C. Pierre, "Characteristic constraint modes for component mode synthesis," *AIAA Journal*, vol. 39, no. 6, pp. 1182-1187, 2001.

[23] M. S. Shephard, "Linear multipoint constraints applied via transformation as part of a direct stiffness assembly process," *International Journal for Numerical Methods in Engineering*, vol. 20, no. 11, pp. 2107-2112, Nov. 1984.

[24] J. F. Doyle, *Wave propagation in structures : spectral analysis using fast discrete Fourier transforms*, 2nd ed. New York: Springer, 1997.

[25] M. Petyt, *Introduction to finite element vibration analysis*. Cambridge: Cambridge University Press, 1998, p. xv, 558 p.

[26] F. Fahy, J. Walker, and NetLibrary Inc., *Advanced applications in acoustics, noise, and vibration*. London ; New York: Spon, 2004, p. xiii, 640 p.

[27] W. Soedel, *Vibrations of shells and plates*, 3rd ed., no. 177. New York: Marcel Dekker, 2004, p. xxiv, 553 p.

[28] T. J. R. Hughes and M. Cohen, "The `heterosis' finite element for plate bending," *Computers and Structures*, vol. 9, no. 5, pp. 445-450, 1978.

[29] H. Nguyen-Xuan, T. Rabczuk, S. Bordas, and J. F. Debongnie, "A smoothed finite element method for plate analysis," *Computer Methods in Applied Mechanics and Engineering*, vol. 197, no. 13-16, pp. 1184-1203, 2008.

[30] P. Shorter, "Combining finite elements and statistical energy analysis," Ph.D thesis . University of Auckland, 1998.

[31] L. Hinke, B. R. Mace, and T. P. Waters, "Analysis of structures with uncertain parameters using component mode synthesis," in *ISMA 2006*, Leuven 2006.

[32] C. Lecomte, J. J. Forster, B. R. Mace, and N. S. Ferguson, "Bayesian inference for uncertain dynamic systems," in *Proceedings of the 10th International Conference on Recent Advances in Structural Dynamics*. Southhampton 2010.

[33] L. Hinke, F. Dohnal, B. R. Mace, T. P. Waters, and N. S. Ferguson, "Component mode synthesis as a framework for uncertainty analysis," *Journal of Sound and Vibration*, vol. 324, no. 1-2, pp. 161-178, 2009.

[34] W. C. Hurty, "Dynamic analysis of structural systems using component modes," *AIAA Journal*, vol. 3, pp. 678-685, 1965.

[35] R. B. M. Hintz, "Analytical methods in component modal synthesis," *AIAA Journal*, vol. 13, no. 8, pp. 1007-1016, Aug. 1975.

[36] R. H. MacNeal, "A hybrid method of component mode synthesis," *Computers and Structures*, vol. 1, no. 4, pp. 581-601, Dec. 1971.

[37] S. Rubin, "Improved component-mode representation for structural dynamic analysis," *AIAA Journal*, vol. 13, no. 8, pp. 995-1006, Aug. 1975.

[38] J. Craig R. R., "A review of time-domain and frequency-domain component mode synthesis methods," *Journal of Modal Analysis*, vol. 2, no. 2, pp. 59-72, 1987.

[39] J. Craig R. R., "Methods of component mode synthesis," *Shock and Vib. Digest*, vol. 9, pp. 3-10, 1977.

[40] J. Craig R. R., "Substructure methods in vibration," *J. Vib. Acoust*. June 1995 Volume 117, Issue B, 207.

[41] J. Craig R. R., *Structural Dynamics - An Introduction to Computer Methods*. Wiley, 1981.

[42] R. R. J. Craig and A. J. Kurdila, *Fundamentals of Structural Dynamics*. Wiley, 2006.

[43] Z. Bai, "Krylov subspace techniques for reduced-order modeling of large-scale dynamical systems," *Applied Numerical Mathematics*, vol. 43, no. 1-2, pp. 9-44, Oct. 2002.

[44] J. Craig R. R. and C. J. Chang, "On the use of attachment modes in substructure coupling for dynamic analysis," in *AIAA/ASME 18th Struc., Struc. Dyn. and Materials Conf.*, 1977.

[45] M. Woodbury, "Inverting Modified Matrices: Memorandum Rept. 42," *... Research Group, Princeton University, Princeton, NJ*, 1950.

[46] G. Mergen and L. Tong, "Type based estimation over multiaccess channels," *Signal Processing, IEEE Transactions on*, vol. 54, no. 2, pp. 613–626, 2006.

[47] G. M. Megson, "Systolic rank updating and the solution of non-linear equations," in *Parallel Processing Symposium, 1991. Proceedings., Fifth International*, 1991, pp. 344–351.

[48] O. Cakar and K. Sanliturk, "Elimination of transducer mass loading effects from frequency response functions," *Mechanical systems and signal processing*, vol. 19, no. 1, pp. 87–104, 2005.

[49] M. S. Bartlett, "An inverse matrix adjustment arising in discriminant analysis," *The Annals of Mathematical Statistics*, vol. 22, no. 1, pp. 107–111, 1951.

[50] B.G.Falzon, P.Apruzzese "Numerical analysis of intralaminar failure mechanisms in composite structures. Part II: Applications" *Composite Structures*, Volume 93, Issue 2, January 2011, Pages 1047–1053.

[51] B.G.Falzon,D.Hitchings "Capturing mode-switching in postbuckling composite panels using a modified explicit procedure" *Composite structures*, Volume 60, Issue 4, June 2003, Pages 447–453.

[52] B.G.Falzon,D.Hitchings "Mode-Switching In Postbuckling Composite Aerostructures" *Proceedings of the Second International Conference on Structural Stability and dynamics ...*, Singapore 2003.

[53] S. Köksal, M. D. Cömert, and H. N. Özgüven, "Reanalysis of Dynamic Structures Using Successive Matrix Inversion Method," in *Proceedings of the 24th International Modal Analysis Conference, St. Louis, Missouri*, 2006.

[54] A. Swiercz, P. Kolakowski, and J. Holnicki-Szulc, "Damage identification in skeletal structures using the virtual distortion method in frequency domain," *Mechanical Systems and Signal Processing*, vol. 22, no. 8, pp. 1826–1839, 2008.

[55] J. Sherman and W. J. Morrison, "Adjustment of an inverse matrix corresponding to a change in one element of a given matrix," *The Annals of Mathematical Statistics*, vol. 21, no. 1, pp. 124–127, 1950.

[56] R. O. De Alba, B. R. Mace, and N. S. Ferguson, "Prediction of response variability in uncertain point connected structures using component mode synthesis and characteristic constraint modes.," in *Proceedings of the 10th International Conference on Recent Advances in Structural Dynamics*. Southampton UK 2010.

[57] X. Deng, W. Chen, and G. Shi, "Three-dimensional finite element analysis of the mechanical behavior of spot welds," *Finite Elements in Analysis and Design*, vol. 35, no. 1, pp. 17–39, 2000.

[58] P. Lardeur, E. Lacouture, and E. Blain, "Spot weld modelling techniques and performances of finite element models for the vibrational behaviour of automotive structures," in *ISMA 25*, 2000, pp. 409-416.

[59] F. Kuratani, M. Okuyama, T. Yamauchi, and S. Washior, "Finite Element Modeling of Spot Welds for Vibration Analysis," *5th Asian Conference on Multibody Dynamics ACMD2010*, Kyoto Japan 2010.

[60] H.-C. Huang, *Static and Dynamic Analyses of Plates and Shells*. London ; New York: Springer Verlag, 1989.

[61] M. Ouisse and S. Cogan, "Robust design of spot welds in automotive structures: A decision-making methodology," *Mechanical Systems and Signal Processing*, vol. 24, no. 4, pp. 1172-1190, May 2010.

[62] M. Palmonella, "Improving finite element models of spot welds in structural dynamics," *Ph.D Thesis*, University of Wales Swansea 2003.

[63] D. J. Ewins, *Modal Testing - Theory, Practice and Applications, Second Edition*, 2nd ed. Philadelphia: Research Studies Press Ltd., 2001.

[64] D. N. Joanes and C. A. Gill, "Comparing measures of sample skewness and kurtosis," *Journal of the Royal Statistical Society: Series D (The Statistician)*, vol. 47, no. 1, pp. 183-189, Mar. 1998.

[65] B. W. Lindgren, *Basic Ideas of Statistics*. Collier-Mac., 1975, p. 352.

[66] B. Lindgren, *Statistical Theory, Fourth Edition (Chapman & Hall/CRC Texts in Statistical Science)*. Chapman and Hall/CRC.

[67] E. Kreyszig, *Advanced Engineering Mathematics*. John Wiley & Sons.

[68] J. Lee Rodgers, W. A. Nicewander, and J. L. Rodgers, "Thirteen Ways to Look at the Correlation Coefficient," *The American Statistician*, vol. 42, no. 1, p. 59, Feb. 1988.

[69] R. J. Allemang and D. L. Brown, "A correlation coefficient for modal vector analysis," *Proceedings, 1st International Modal Analysis Conference*, pp. 110-116, NY, USA,1982.

[70] A. Saltelli, K. Chan, and E. M. Scott, *Sensitivity Analysis*. Wiley, 2000.

[71] G. I. Schuëller, C. G. Bucher, and H. J. Pradlwarter, "The response surface method - an efficient tool to determine the failure probability of large structural systems," in *International Conference on Spacecraft Structures and Mechanical Testing*, 1991.

[72] G. I. Schuëller, H. J. Pradlwarter, and P. S. Koutsourelakis, "A critical appraisal of reliability estimation procedures for high dimensions," *Probabilistic Engineering Mechanics*, vol. 19, pp. 463-474, 2004.

[73] J. Nie and R. Ellingwood, "Directional methods for structural reliability," *Journal of Structural Safety*, vol. 22, p. 233, 2000.

[74] P. S. Koutsourelakis, H. J. Pradlwarter, and G. I. Schuëller, "Reliability of structures in high dimensions, part I: algorithms and applications," *Probabilistic Engineering Mechanics*, vol. 19, pp. 409-417, 2004.

[75] M. D. McKay, R. J. Beckman, and W. J. Conover, "A comparision of three methods for selecting values of input variables in the analysis of output from a computer code," *Technometrics*, vol. 42, no. 1, 2000.

[76] R. G. Ghanem and P. D. Spanos, *Stochastic Finite Elements: A Spectral Approach*. Dover Publications, 2003.

[77] P. B. Nair, A. J. Keane, and U. Kingdom, "Stochastic reduced basis methods," *AIAA Journal*, vol. 40, no. 8, p. 102514/21837, 2002.

APPENDIX A

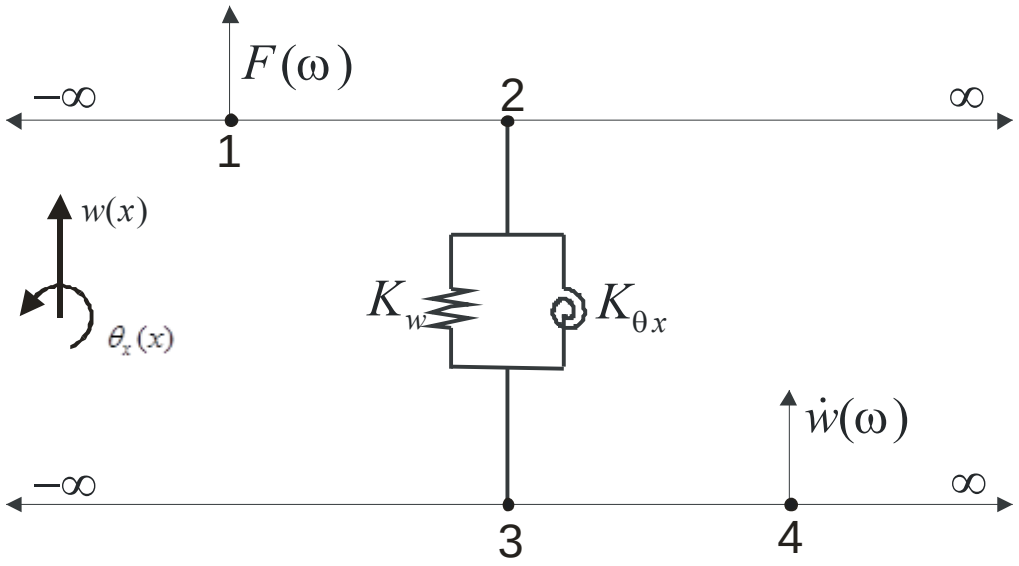

For this system each point has two degrees of freedom, therefore the forces and displacement matrixes at each node are

$$\mathbf{v}_i = \begin{bmatrix} v_i \\ \psi_i \end{bmatrix} \tag{A.1}$$

$$\mathbf{F}_i = \begin{bmatrix} F_i \\ M_i \end{bmatrix} \tag{A.2}$$

Then the mobility matrix $\mathbf{Y}_{ij}$ relates the force matrix in point *i* and the velocity matrix in point *j* as

$$\dot{\mathbf{v}}_j = \mathbf{Y}_{ij}\mathbf{F}_i \tag{A.3}$$

where $\mathbf{Y}_{ij}$ containing the following elements $Y_{\dot{v},F}^{i-j} = {i\omega v_j}/{F_i}$, $Y_{\dot{\psi},F}^{i-j} = {i\omega \psi_j}/{F_i}$, $Y_{\dot{v},M}^{i-j} = {i\omega v_j}/{M_i}$ and $Y_{\dot{\psi},M}^{i-j} = {i\omega \psi_j}/{M_i}$

The equations defining the system in Figure A.1 are; for the upper beam

$$\dot{\mathbf{v}}_2 = \mathbf{Y}_{12}\mathbf{F}_{ext} + \mathbf{Y}_{22}\mathbf{F}_2 \tag{A.4}$$

for the lower beam

$$\dot{\mathbf{v}}_4 = \mathbf{Y}_{34}\mathbf{F}_3 \tag{A.5}$$

Finally the spring can be defined in terms of its mobility

$$\begin{bmatrix} \dot{\mathbf{v}}_2 \\ \dot{\mathbf{v}}_3 \end{bmatrix} = \mathbf{Y}_s \begin{bmatrix} \mathbf{F}_{e2} \\ \mathbf{F}_{e3} \end{bmatrix} \tag{A.5}$$

here the equilibrium forces are

$$\begin{bmatrix} \mathbf{F}_{e2} \\ \mathbf{F}_{e3} \end{bmatrix} = \begin{bmatrix} -\mathbf{F}_2 \\ -\mathbf{F}_3 \end{bmatrix} \tag{A.6}$$

Finally for the system in Figure A-1, the connection is massless. Therefore

$$\mathbf{F}_2 = \mathbf{F}_3 \tag{A.7}$$

APPENDIX B

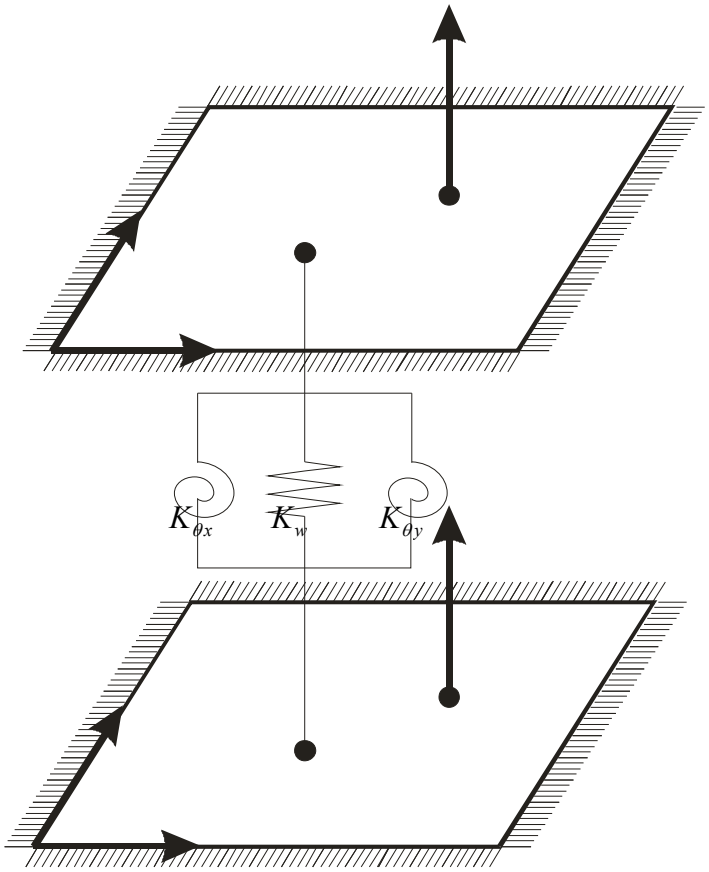

Figure B-1: Two simply supported plates with a single elastic connection

For this system each point has three degrees of freedom, therefore the forces and displacement matrixes at each node are

$$\mathbf{v}_i = \begin{bmatrix} v_i \\ \psi_{xi} \\ \psi_{yi} \end{bmatrix} \tag{B.1}$$

$$\mathbf{F}_i = \begin{bmatrix} F_i \\ M_{xi} \\ M_{yi} \end{bmatrix} \tag{B.2}$$

Then the mobility matrix $\mathbf{Y}_{ij}$ relates the force matrix in point *i* and the velocity matrix in point *j* as

$$\dot{\mathbf{v}}_j = \mathbf{Y}_{ij}\mathbf{F}_i \tag{B.3}$$

where $\mathbf{Y}_{ij}$ containing the following elements $Y_{\dot{v},F}^{i-j} = {i\omega v_j}/{F_i}$, $Y_{\dot{\psi}x,F}^{i-j} = {i\omega\psi_{xj}}/{F_i}$, $Y_{\dot{\psi}y,F}^{i-j} = {i\omega\psi_{yj}}/{F_i}$, $Y_{\dot{v},Mx}^{i-j} = {i\omega v_j}/{M_{xi}}$, $Y_{\dot{\psi}x,Mx}^{i-j} = {i\omega\psi_{xj}}/{M_{xi}}$, $Y_{\dot{\psi}y,Mx}^{i-j} = {i\omega\psi_{yj}}/{M_{xi}}$, $Y_{\dot{v},My}^{i-j} = {i\omega v_j}/{M_{yi}}$, $Y_{\dot{\psi}x,My}^{i-j} = {i\omega\psi_{xj}}/{M_{yi}}$ and $Y_{\dot{\psi}y,My}^{i-j} = {i\omega\psi_{yj}}/{M_{yi}}$.

The equations defining the system in Figure B.1 are; for the upper plate

$$\dot{\mathbf{v}}_2 = \mathbf{Y}_{12}\mathbf{F}_{ext} + \mathbf{Y}_{22}\mathbf{F}_2 \tag{B.4}$$

for the lower plate

$$\dot{\mathbf{v}}_4 = \mathbf{Y}_{34}\mathbf{F}_3 \tag{B.5}$$

Finally the spring can be defined in terms of its mobility

$$\begin{bmatrix} \dot{\mathbf{v}}_2 \\ \dot{\mathbf{v}}_3 \end{bmatrix} = \mathbf{Y}_s \begin{bmatrix} \mathbf{F}_{e2} \\ \mathbf{F}_{e3} \end{bmatrix} \tag{B.5}$$

here the equilibrium forces are

$$\begin{bmatrix} \mathbf{F}_{e2} \\ \mathbf{F}_{e3} \end{bmatrix} = \begin{bmatrix} -\mathbf{F}_2 \\ -\mathbf{F}_3 \end{bmatrix} \tag{B.6}$$

Finally for the system in Figure B-1, the connection is massless. Therefore

$$\mathbf{F}_2 = \mathbf{F}_3 \tag{B.7}$$